The Dissertation Committee for Jun Koda
certifies that this is the approved version of the following dissertation:

Gravitational Dynamics of Halo Formation in a Collisional Versus Collisionless Cold Dark Matter Universe

Committee:

Paul R. Shapiro, Supervisor

Duane A. Dicus

Eiichiro Komatsu

Richard A. Matzner

Steven Weinberg

Gravitational Dynamics of Halo Formation in a Collisional Versus Collisionless Cold Dark Matter Universe

by

Jun Koda, B.S.

DISSERTATION

Presented to the Faculty of the Graduate School of

The University of Texas at Austin

in Partial Fulfillment

of the Requirements

for the Degree of

DOCTOR OF PHILOSOPHY

THE UNIVERSITY OF TEXAS AT AUSTIN

December 2009

Dedicated to the C++ programming language

Acknowledgments

I would like to thank Paul Shapiro for thorough and patient advising. I would also like to thank Eiichiro Komatsu for helpful discussions and organising informative meeting on cosmology and astrophysics, and Milos Milosavljević for giving me chances to work on wide range of topics.

I appreciate Texas Advanced Computing Center for managing Dell-Linux computation cluster "Lonestar," on which I perform most of numerical simulations, and for many helpful lectures. My work was supported in part by Chandra grant SAO TM8-9009X, NSF grant AST 0708176 and NASA grant NNX07AH09G.

Gravitational Dynamics of Halo Formation in a Collisional Versus Collisionless Cold Dark Matter Universe

Publication No. _____

Jun Koda, Ph.D.
The University of Texas at Austin, 2009

Supervisor: Paul R. Shapiro

Flat cosmology with collisionless cold dark matter (CDM) and cosmological constant (ΛCDM cosmology) may have some problems on small scales, even though it has been very successful on large scales. We study the effect of Self-Interacting Dark Matter (SIDM) hypothesis on the density profiles of halos. Collisionless CDM predicts cuspy density profiles toward the center, while observations of low mass galaxies prefer cored profiles. SIDM was proposed by Spergel & Steinhardt [161] as a possible solution to this cuspy profile problem on low-mass scales. On the other hand, observations and collisionless CDM agree on mass scales of galaxy clusters. It is also known that the SIDM hypothesis would contradict with X-ray and gravitational lensing observations of cluster of galaxies, if the cross section were too large. Our final goal is to find the range of SIDM scattering cross section models that are consistent with those astrophysical observations in two different mass scales.

There are two theoretical approaches to compute the effect of self-interacting scattering – Gravitational N-body simulation with Monte Carlo scattering and conducting fluid model; those two approaches, however, had not been confirmed to agree with each other. We first show that two methods are in reasonable agreement with each other for both isolated halos and for halos with realistic mass assembly history in an expanding ΛCDM universe; the value of cross section necessary to have a maximally relaxed low-density core in ΛCDM is in mutual agreement.

We then develop a semianalytic model that predicts the time evolution of SIDM halo. Our semianalytic relaxation model enables us to understand how a SIDM halo would relax to a cored profile, and obtain an ensemble of SIDM halos from collisionless simulations with reasonable computational resources. We apply the semianalytic relaxation model to CDM halos, and compare the resulting statistical distribution of SIDM halos with astrophysical observations. We show that there exists a range of scattering cross sections that simultaneously solve the cuspy core problem on low-mass scales and satisfy the galaxy cluster observations.

We also present that other potential conflicts between ΛCDM and observations could be resolved in Part II and III.

Table of Contents

Acknowledgments v

Abstract vi

List of Tables xii

List of Figures xiii

Part I Self Interacting Dark Matter 1

Chapter 1. Introduction 2

1.1 Self-Interacting Dark Matter (SIDM) 2

1.2 Monte Carlo Scattering Algorithm 7

1.3 Conducting Fluid Model 8

1.3.1 Gravothermal Catastrophe 9

1.3.2 Definitions and Notations 10

1.3.3 Fluid Approximation and Conducting Fluid Model 11

Chapter 2. Comparison of Conducting Fluid Model with Monte Carlo N-body Simulations I: Isolated SIDM Halos 15

2.1 Comparison Setup 17

2.1.1 Definitions 17

2.1.2 Self-Similar Solution of Gravothermal Collapse 18

2.1.3 The Monte Carlo N-body Simulations 19

2.1.4 Analysis of N-body Data 21

2.2 Results 23

2.2.1 Self-Similar Solution 23

2.2.2 Evolution in the Transitional Regime 26

2.2.3 Plummer Model 27
2.2.4 NFW & Hernquist Profile 29
2.3 Discussions 34
2.3.1 Implications on the Cosmological Similarity Solution 34
2.3.2 The Source of Difference 36
2.4 Conclusion 37

Chapter 3. Comparison of Conducting Fluid Model with Monte Carlo N-body Simulations II: Cosmological SIDM halos 42
3.1 Cosmological Conducting Fluid Model 43
3.1.1 Fluid Equations 43
3.1.2 Initial Condition 45
3.2 Summary of N-body simulations 46
3.3 Results 48

Chapter 4. Monte Carlo N-body Simulations 53
4.1 Models of Elastic Scattering Cross Sections 53
4.2 Monte Carlo Scattering Algorithm 55
4.3 Relaxation of an Isolated Halo 59
4.3.1 Relaxation Time 60
4.3.2 Time Evolution of the Central Density 61
4.4 Cosmological SIDM Simulations 63
4.4.1 Simulation Setup 63
4.5 Partially Relaxed Density Profiles 66
4.5.1 Cored NFW Formula 66
4.5.2 Rotation Curves 71

Chapter 5. Semianalytic Relaxation Model 75
5.1 The Model: Flattening in ΛCDM 76
5.2 Numerical Method of Solving the Model 79
5.3 Verification of the Model 81
5.4 Analytical Properties 83
5.4.1 Self-Similar Solution 83

Chapter 6. Statistical Properties of SIDM Halos in ΛCDM **87**
6.0.2 Cosmological Collisionless N-body Simulations 87
6.0.3 Comparison with Observed Galaxy Rotation Curves 89
6.0.4 Comparison with Observed Galaxy Cluster Density Profiles . 91
6.1 Conclusion 96

Part II A Collision of Clusters of Galaxies **103**

Chapter 7. The Cluster-Merger Shock in 1E 0657-56 **104**
7.1 Introduction 105
7.2 Simulation 105
7.3 Results 106
7.4 Discussion and Conclusions 108

Part III Abundance of Disc-Dominated Galaxies in ΛCDM **110**

Chapter 8. On the Survival and Abundance of Disk-dominated Galaxies **111**
8.1 Introduction 112
8.2 Disk Survival in ΛCDM Cosmology 115
8.2.1 Mechanisms for Bulge Formation in Mergers 115
8.2.2 The Critical Virial Velocity for Bulge Formation after Reionization and Jeans-Mass Filtering 118
8.2.3 Merger Histories of Low-Mass Galaxies 119
8.2.4 Results 123
8.3 Conclusions 133

Appendices **136**

Appendix A. Scattering Cross Sections **137**
A.1 The Definition 137
A.2 Classical Mechanics 138
A.2.1 Hard Sphere 139

A.2.2 The Maxwell Molecule or the Inverse Power Law Model . . . 141
A.2.3 The Rutherford Scattering 142
A.3 Quantum Mechanics 143
A.3.1 Yukawa Cross Section 143

Bibliography **146**

Vita **161**

List of Tables

2.1 Parameters used for Monte Carlo N-body simulations 41

4.1 Multi-resolution simulations 66

6.1 Uniform resolution cosmological simulations 88
6.2 Best fit parameters for low mass SIDM halos results 91
6.3 Best fit parameters for r_c-M_{500} fit (hard sphere) 101
6.4 Best fit parameters for r_c-M_{500} fit (Yukawa cross sections) 102

List of Figures

2.1 Resolution test 22
2.2 Density and velocity dispersion profiles 24
2.3 Central quantities plotted as a function of the time 25
2.4 Time evolution in the transitional regime 28
2.5 Collapse of the Plummer model 30
2.6 Profiles of collapsing NFW and Hernquist halos 32
2.7 Time evolution of NFW and Hernquist halos 33
2.8 The effect on the similarity solution 33
2.9 Anisotropy of the collapsing halos 40

3.1 Mass accretion histories 47
3.2 Density profiles of N-body and Fluid 50
3.3 Monte Carlo N-body v.s. Fluid model for a cosmological Milky-Way size halo 51
3.4 Same as Fig. 3.3 but for the cluster sized halo 51

4.1 Relaxation curve: Relaxation of an isolated NFW halo 62
4.2 Density map of Monte Carlo N-body simulations 67
4.3 Cored NFW profile 68
4.4 Rotation curves of partially relaxed isolated SIDM halos 73
4.5 Rotation curves of cosmological SIDM halos 74

5.1 Comparison of our model with Monte Carlo N-body 81
5.2 Same as Fig. 5.1, but for intermediate and cluster scales 82
5.3 Same as Fig. 5.1, but with Maxwell and Yukawa-like cross sections 82
5.4 Self-similar solution of the model 86

6.1 SIDM halo statistics on galaxy scales 92
6.2 Distribution of SIDM halo properties 93

6.3 Density profile of a galaxy cluster A2029 97
6.4 SIDM halo statistics on cluster scales 98
6.5 Distribution of scaled SIDM core radii in cluster scales 99
6.6 Same as Fig. 6.4 but for Yukawa-like velocity dependent cross section 99
6.7 Same as Fig. 6.7 but for Yukawa-like velocity dependent cross section 100

7.1 Time evolution of temperature 106
7.2 Velocity, density, temperature and position of the shock 107
7.3 Surface brightness and Temperature profiles 109
7.4 Thermal bremsstrahlung emission spectrum 109

8.1 Examples of merger trees. Gray circles represent disk-dominated galaxies and black circles represent galaxies with classical bulges, respectively, under a bulge-forming criterion $\mu_{\rm crit} = 0.3$, $V_{\rm vir,crit} = 55$ km s^{-1}. Radii of circles are proportional to $M^{1/3}$. Mergers with $\mu < 0.05$ are not plotted in the figure. Vertical axis label is redshift. 120
8.2 The fraction of disk-dominated galaxies 124
8.3 Disk-dominated fraction as a function of galaxy-hosting halo Mass . 129
8.4 The redshift distribution of first mergers that create classical bulges. 130
8.5 Fraction of halos that have not experienced a merger with mass ratio M_2/M_1 or larger since redshift z. 131

A.1 Hard Sphere Cross Section 140
A.2 Rutherford scattering 143

Part I

Self Interacting Dark Matter

Chapter 1

Introduction

1.1 Self-Interacting Dark Matter (SIDM)

In the currently standard cosmological model (Lambda Cold Dark Matter, ΛCDM), a flat universe with a cosmological constant, contains collisionless cold dark matter as its dominant matter component, perturbed by primordial Gaussian-random-noise density fluctuations. This model has been highly successful at explaining observations of the background universe and large-scale structure. On small scales, however, the distribution of dark matter in coordinate and velocity space is not fully understood. N-body simulations show that the density profiles of the virialized regions ("halos") that form in this collisionless dark matter are cuspy, such as the Navarro-Frenk-White (NFW) profile [142], in which $\rho \rightarrow r^{-1}$ toward the center. Recent high resolution simulations show that the inner profile is not exactly a power law, and varies a little from halo to halo [50, 63, 77, 144, 166]. On the other hand, a cored profile, such as a pseudo-isothermal profile, is observed in dwarf and low surface brightness (LSB) galaxies [48, 49, 64, 65, 110, 111, 184]. Dwarf spiral and LSB galaxies are dark matter-dominated systems which are thought to be less affected by the complexity of the dissipative energy-releasing baryonic component, and, therefore, ideal to understand the dark matter distribution on small scales. Many dwarf and LSB galaxies have flat cores, although some of them are

also consistent with an NFW profile [75, 77, 159, 159, 177]. Non-circular motions may affect the density profile estimate [75], but they are usually not strong enough to make observations consistent with the theoretically-predicted cuspy profile [112, 145, 176].

Many observed galaxies have a lower central density than simulated halos as well [6, 160]. Although baryons can play a significant role in galaxies, there is no established solution to this paradox. Strong bars can reduce the central density [154, 182], but debates continue as to whether that mechanism can solve the cuspy core problem [e.g. see introduction of 155].

Spergel & Steinhardt [161] proposed self-interacting dark matter (SIDM) as a possible solution to this cuspy core problem. Heat transfer within the virialized halos due to these non-gravitational collisions then makes the halo cores expand. This idea was confirmed by several numerical and analytical studies. Burkert [37] introduced a Monte Carlo scattering algorithm between dark matter particles to take the self-interaction into account in a numerical N-body simulation, and this method was refined by Kochanek & White [102]. Cosmological simulations show that a cross section per unit mass $\sigma = 0.5 - 5$ cm^2 g^{-1} makes the profile cored, and the cored profile is stable [46, 183]. Colín et al. [42] emphasized that the profile depends on the accretion history, especially when the last major merger occurred.

Balberg, Shapiro, & Inagaki [13, hereafter BSI] applied a conducting fluid model, originally invented to describe gravitational scattering in star clusters, to isolated SIDM halos; SIDM collisions are represented by a thermal conduction of fluid. BSI derived a self-similar gravothermal collapse solution at large Knudsen

number (Kn, the ratio of mean free path to the system size); the solution shows that an isolated halo collapses within a finite time. They also showed that the collapse is delayed compared to their self-similar solution when the Knudsen number is comparable to or smaller than one, because the length scale of energy exchange is restricted by the mean free path.

A realistic halo is not isolated; it has a cosmological infall and a finite pressure at the virial radius [158]. Ahn & Shapiro [4] derived a fully cosmological similarity solution with such boundary conditions for arbitrary value of the Knudsen number. This solution shows that the gravothermal collapse of the isolated halo in the BSI solution is prevented by the infall, and the core has a constant size in units of the virial radius, for a given SIDM cross section. When there is no self-interaction, this fluid approximation gives a density profile similar to the cuspy profile found in N-body simulations. This shows that the fluid approximation also describes the virialization of collisionless dark matter appropriately, providing, in effect, an analytical derivation of the NFW profile in the collisionless limit. In the presence of SIDM scattering collisions those analytical solutions are in qualitative agreement with the corresponding Monte Carlo N-body simulations as well; SIDM halos have cores and they do not collapse within a Hubble time in a cosmological environment. However, the values of the cross section necessary to explain the observed dark matter density profiles are not in agreement. Ahn & Shapiro [4] claim that $\sigma \sim 200$ cm^2 g^{-1} fits the dwarf and LSB galaxy rotation curves best, while results of N-body simulations claim that $\sigma = 0.5 - 5$ cm^{2}g^{-1} give the observed central density. The difference between these estimates has not yet been

understood. It could be due in part to the difference between hierarchical assembly and smooth accretion, or the difference between self-similar evolution and non-self-similar accretion. But it is possible that either the N-body or the fluid model does not describe the system correctly. We make the direct comparisons, for the first time, to exclude the latter possibility. We will show in Chapters 2 and 3 that the fluid model and Monte Carlo scattering simulations agree reasonably well with each other under the same conditions (halos are either isolated or have cosmological infall with a common mass accretion history); the difference in the mass accretion history between the similarity solution and the N-body simulations caused the large difference.

There are some constraints on the value of the SIDM cross section, mainly when the dark matter velocity is high. Observations of galaxy cluster 1E 0657-56, known as the "bullet cluster," with total matter density mapped by weak and strong gravitational lensing measurements while the density of the intergalactic baryon-electron fluid was mapped by X-ray measurements, show that the dark matter and the baryon-electron plasma are spatially segregated as they would be if the dark matter is not highly collisional [40]. Dark matter and galaxies of the subcluster have passed through the main cluster without distortion while the baryon gas shows a bow shock due to its collisional nature. Analytical estimates and Monte Carlo N-body simulations of the bullet cluster constrain the velocity independent cross section to be $\sigma < 0.7$ cm^2 g^{-1}, using the fact that the mass-to-light ratio of the subcluster is normal [127, 148]. Larger cross section would make the mass-to-light ratio smaller because the SIDM collisions scatter the dark matter out of the subhalo.

(On the other hand, see Mahdavi et al. [123] for a possibility that SIDM with cross section $\sim$ 4 cm^{2}g^{-1} explains a cluster Abell 520 which has substructures with anomalous mass-to-light ratio). This almost excludes the possibility that a velocity-independent cross section solves the cuspy core problem ($\sigma < 0.7$ is probably too small to solve the cuspy core problem). If the cross section is velocity dependent (e.g. $\sigma \propto v^{-1}$), however, it only puts a constraint at very large relative velocity. The relative velocity of the merging halos is estimated to be between $2,500$ and $4,000$km s^{-1} at their observed separation, and even higher at center passage [129, 137, 163].

Additional constraints on SIDM from cluster observations are given by the density profile of relaxed clusters; N-body results find that the core size of relaxed SIDM clusters of galaxies becomes too large if the cross section is $\sim$ 1 cm^{2}g^{-1} [9, 117, 183]. Those constraints do not necessarily exclude SIDM as the solution to the cuspy core problem on the galaxy scale, however, if the cross section is velocity dependent [e.g., inversely proportional to relative speed, 54, 60]. Even for velocity-independent cross section, the self-similar analytical solutions of Ahn & Shapiro [4] suggest that cluster core sizes will be less affected by SIDM relaxation than for dwarf galaxies, if the cross section is large enough such that the heat conduction is suppressed by the small Kn effect at cluster scales; such large cross section, however, is disfavored by the observation of the merging "bullet cluster."

Hennawi & Ostriker [81] constrain the possibility that dark matter is highly collisional near super massive black holes. Scattering feeds the black hole too much if the SIDM collision rate is too high. Gnedin & Ostriker [66] constrain the amount

of heating and evaporation of substructure halos in clusters due to SIDM scatterings.

There was an additional motivation for the SIDM hypothesis when it was first put forth, involving the overabundance of subhalos in CDM N-body simulation compared to observations of the Local Group. The number of substructures in the collisionless CDM model has previously been thought to be about an order of magnitude larger than the observed number of dwarf galaxies in the Local Group. SIDM does not solve this problem [51]; although the number of substructures is reduced by SIDM stripping, as anticipated by the original paper [161], the cross-section that makes the profile cored ($0.6\,\mathrm{cm}^2\mathrm{g}^{-1}$) is not efficient enough to reduce the number of satellites down to the observed level.

In view of the large difference between the numerical and analytical estimates mentioned above for the cross section required for SIDM to solve the cuspy core problem in dwarf and LSB galaxies, it is important to understand this difference in order to assess these other constraints on the SIDM cross section, as well. That is the purpose of our first two chapters. We briefly describe the Monte Carlo numerical algorithm for the SIDM elastic scattering in N-body simulations in §1.2, and summarize the basis for the conducting fluid model in §1.3. We test those two methods against each other for isolated halos in Chapter 2 and for halos in a cosmological environment in Chapter 3.

1.2 Monte Carlo Scattering Algorithm

Monte Carlo scattering algorithm is a particle-based numerical method to simulate collisional matter. We simulate the non-gravitational scattering between SIDM par-

ticles with this Monte Carlo algorithm, in addition to Newtonian self gravity. At each time step, each N-body particle collides with at most one of its neighbors randomly with a collision rate calculated from a given scattering cross section. When two particles collide, a new direction of the relative velocity is selected randomly from an isotropic distribution (for simplicity, we assume an isotropic differential cross section in our research, but the algorithm can be easily generalized to an arbitrary differential cross section).

The Monte Carlo scattering algorithm for particle-particle scattering has been used for more than thirty years to solve physics and engineering problems of collisional molecules, giving reasonable results [known as direct simulation Monte Carlo, 24]. For example, it agrees with an exact solution of the spatially homogeneous Boltzmann equation that describes the relaxation toward a Maxwellian distribution; when applied to a Couette flow at small Kn, it agrees with the Navier-Stokes equation solution and molecular experiments. [e.g., 24, 141].

We implemented this Monte Carlo algorithm in a publicly available N-body simulation code GADGET [164]. We will explain more technical details in § 4.2.

1.3 Conducting Fluid Model

We review the conducting fluid model, which was originally invented to describe the gravothermal collapse of globular star clusters.

1.3.1 Gravothermal Catastrophe

Self-gravitating systems have negative specific heats; when thermal energy is removed from the system, the system gets hotter. Therefore, when the energy conducts from hot center in a spherical system to cooler outer radii, the center get even hotter, which results in larger amount of heat transfer; this unstable process is known as the gravothermal catastrophe [121]. It is also called the gravothermal collapse because the constant density core at center gets smaller and denser during the gravothermal catastrophe. Globular stellar clusters are such "collisional" self-gravitating systems that may already have collapsed during the age of universe; stars are scattered gravitationally with the Rutherford scattering cross section. Gravothermal collapse of stellar system is well understood by numerical Fokker-Planck computations [41, 169] and by N-body simulations [17, 100, 124, 165, 168].

Another approach to understand the collisional self-gravitating system is to use moment equations derived from Boltzmann equation. Boltzmann equation can be written as an infinite series of moment equations; there were several attempts to close the infinite moment hierarchy for star clusters, approximately, and obtain a finite number of partial differential equations, including the fluid equations – continuity, Euler and energy equations [74, 114, 119]. Lynden-Bell & Eggleton [120, *hereafter LBE*] invented a successful thermal conduction formula for collisional star clusters based on a simple dimensional analysis. The system of fluid equations with that LBE thermal conduction is called the conducting fluid model, or the gaseous model. The model has been shown to be successful for star clusters; (a) the

analytical solution of the model, by LBE, that describes the self-similar collapse appear in the late stage of Fokker-Plank and N-body computations; (b) when the time evolution of a Plummer sphere is solved numerically by integrating the partial differential equations of the fluid model, the resulting collapse time agrees with that from other numerical methods [68, 79].

SIDM halos and globular clusters are both "collisional" self-gravitating systems, but the angular distribution and velocity dependence of the collisions are different in the two cases. Stars obey Rutherford scattering, which is dominated by small-angle scattering and small velocity encounters, $\sigma \propto v^{-4}$, while the SIDM cross section we explore in the first two chapters is isotropic and velocity independent. It is possible, however, that the SIDM interaction also obey Rutherford scattering via "dark-photon" [3, 59].

1.3.2 Definitions and Notations

We use scattering cross section per unit mass σ (scattering cross section divided by the particle mass) to characterise the interaction of SIDM; the reason we use a cross section per mass is because we know the mass density of dark matter, but do not know the number density. We assume that all dark matter particles have the same mass and the same cross section, but besides that, our studies of SIDM is independent of the particle mass. In Chapters 2 and 3, we assume a hard sphere cross section, which is a differential cross section independent of both relative velocity and scattering angle (Appendix A.2.1); but the conducting fluid model is applicable to other scattering cross sections.

The conducting fluid model is written with the following macroscopic fluid variables as a function of position $\boldsymbol{x}$ and time t: mass density $\rho(\boldsymbol{x}, t)$, one-dimensional velocity dispersion $v(\boldsymbol{x}, t)$[1] and heat flux $\boldsymbol{q}$; heat flux is the amount of energy that passes a unit area perpendicular to the vector $\boldsymbol{q}$ per unit time. We also use pressure $p \equiv \rho v^2$, and specific energy $e \equiv 3v^2/2$, in which monoatomic particle is assumed, i.e., no internal mode such as rotation or vibration. We sometimes use the word temperature and velocity dispersion interchangeably because they are related by the Boltzmann constant k_B: $k_B T \equiv m v^2$.

Mean free path λ is defined as $\lambda \equiv 1/(\rho\sigma)$. The ratio of the mean free path to the system size is known as the Knudsen number, Kn, which characterize the importance of collisionality in that system. The local relaxation time is defined as $t_r \equiv 1/(a\rho\sigma v)$, where the constant $a \equiv \sqrt{16/\pi} \approx 2.26$ defined in BSI; the relaxation time is defined as the inverse of the collision rate of particles that follow a Maxwellian distribution.

1.3.3 Fluid Approximation and Conducting Fluid Model

The Boltzmann equation, which is a partial differential equation on phase space, can be written as an infinite series of moment equations on position space by integrating over all velocities. When third moments are negligible (skewless) the series of moment equations can be closed by truncating at second order, as described in Ahn & Shapiro [4] (*fluid approximation*). Same equations would result from assuming a

[1] Velocity dispersion is a tensor in general, but we assume an isotropic (diagonal) velocity dispersion: $\langle (v_i - u_i)(v_j - u_j)^2 \rangle = v^2 \delta_{ij}$ for all $i = 1, 2, 3$

Gaussian velocity distribution (not necessarily isotropic, i.e. Maxwellian), which is called Gaussian closure [115]. The fluid approximation can describe the structure formation of collisionless CDM, and accurately reproduce the CDM halo properties resulting from spherical cosmological infall (secondary infall model) [4]. If velocity isotropy is imposed in addition, the fluid approximation gives the familiar Euler equation for an ideal gas with ratio of specific heats, $\gamma = 5/3$.

When collisions are important, (e.g., gravitational scattering between stars or dark matter self-interaction), thermal conduction, which is one of the third order moments, should not be neglected. Accurate evaluation of third moments, however, is only successful in the small Knudsen number regime, $Kn \ll 1$, i.e., first order perturbation with respect to the small mean free path. In this regime, the Navier-Stakes equation is derived from the Boltzmann equation with the Fourier law of heat flux, $\boldsymbol{q}_s$,

$$\boldsymbol{q}_s = -\frac{3}{2} a^{-1} b \rho \frac{\lambda^2}{t_r} \boldsymbol{\nabla} v^2, \tag{1.1}$$

where $b \equiv 25\sqrt{\pi}/32 \approx 1.38$ is a constant[2] derived from Chapman-Enskog theory for hard elastic spheres [39, 118]; the mean free path λ, the local relaxation time t_r, and the constant a were defined in § 1.3.2. Direct simulation Monte Carlo results agree with this thermal conductivity in this regime for the one-dimensional Fourier flow problem: steady state of heat transfer between two thermal bath at the edges [24, 62].

In the other limit, $Kn \gg 1$, Lyndel-Bell & Eggleton [LBE] found that an

[2]BSI used a value $b = 25\pi/(32\sqrt{6}) \approx 1.002$, but it should be $25\pi/32$.

empirical thermal conduction formula with λ replaced by the gravitational scale height (or, Jeans length) $H \equiv \sqrt{v^2/4\pi G\rho}$ explains the gravothermal catastrophe of star clusters very well, i.e.,

$$\boldsymbol{q}_l = -\frac{3}{2} C\rho \frac{H^2}{t_r} \boldsymbol{\nabla} v^2, \tag{1.2}$$

where C is an unknown constant of order unity. The scale height H characterizes the length scale over which particles (or stars) orbit under the gravitational force. Balberg et al. [13] combined the two limiting forms of the thermal conduction in a single form,

$$\boldsymbol{q} = -\frac{3}{2}\rho \left[\left(C\frac{H^2}{t_r} \right)^{-1} + \left(a^{-1} b \frac{\lambda^2}{t_r} \right)^{-1} \right]^{-1} \boldsymbol{\nabla} v^2 \tag{1.3}$$

The first term in the bracket is the LBE formula (Eq. 1.2), which dominates in the large Knudsen number limit, $\lambda \gg H$. In the other limit ($\lambda \ll H$), second term in the bracket dominates and the conduction converges to Equation (1.1), instead. BSI's formula is an empirical interpolation between those two limits. BSI assumed $C = b$, but the exact value is not known analytically. We determine the value of C by fitting the Monte Carlo N-body data in §2.2.1.

The conducting fluid model is a set of moment equations closed empirically by this thermal conduction $\boldsymbol{q}$, as follows. Hereafter, we assume spherical symmetry and velocity isotropy; the velocity distribution inside a dark matter halo is known to be nearly isotropic. We introduce a commonly used symbol $L(r) = 4\pi r^2 q_r$ which is the energy flux across a sphere of radius r per unit time. The system of partial

equations for the conducting fluid model is,

$$\frac{\partial \rho}{\partial t} + \frac{1}{r^2}\frac{\partial}{\partial r}(r^2 \rho u) = 0, \tag{1.4}$$

$$\rho \frac{Du}{\partial t} = -\frac{\partial p}{\partial r} - \rho \frac{GM}{r^2}, \tag{1.5}$$

$$-\frac{1}{4\pi r^2}\frac{\partial L}{\partial r} = \rho v^2 \frac{D}{Dt} \ln\left(\frac{v^3}{\rho}\right) \left(= \frac{3}{2}\rho \frac{D}{Dt} v^2 + \rho p \frac{D}{Dt}\frac{1}{\rho}\right) \tag{1.6}$$

$$\frac{L}{4\pi r^2} = -\frac{3}{2}\rho \left[\left(C\frac{H^2}{t_r}\right)^{-1} + \left(a^{-1} b \frac{\lambda^2}{t_r}\right)^{-1}\right]^{-1} \frac{\partial v^2}{\partial r}, \tag{1.7}$$

where $M = M(r)$ is the mass enclosed by radius r, u is the radial component of the macroscopic velocity $\boldsymbol{u}$ and $D/Dt = \partial/\partial t + u\partial/\partial r$ is the Lagrangian derivative. The first equation states the continuity of matter, second is the Euler equation, and the third is the first law of thermodynamics, in the form relating energy transfer and entropy: "$dQ = TdS (= dE + pdV)$." When the time evolution is much slower compared to the dynamical time of the system, the second equation can be replaced by the hydrostatic equilibrium equation,

$$\frac{\partial p}{\partial r} + \rho \frac{GM}{r^2} = 0. \tag{1.8}$$

In the problem of gravothermal collapse, this is a good approximation, because the collapse time scale is more than a hundred times larger than the dynamical time.

Chapter 2

Comparison of Conducting Fluid Model with Monte Carlo N-body Simulations I: Isolated SIDM Halos

Our focus here will be on the question of whether the conducting fluid model and numerical Monte Carlo scattering N-body results agree on the problem of gravothermal catastrophe, in the novel situation in which gravitational scattering in star clusters has been replaced by non-gravitational elastic scattering in an otherwise collisionless-dark matter halo. We make direct comparisons between Monte Carlo N-body simulations and analytic and numerical solutions of a conduction fluid (gaseous) model, for various isolated self-interacting dark matter (SIDM) haloes. There was a disagreement between two methods on the sufficient strength of collisionality to solve the cuspy profile problem, but we will show that the two methods agree to within 20% for isolated haloes.

The Monte Carlo N-body agrees very well with the analytical self-similar solution of gravothermal collapse in the fluid model by Balberg, Shapiro, & Inagaki [13, (BSI)] when one free parameter, the coefficient of thermal conduction, is calibrated against the Monte Carlo N-body simulation. The density profile evolves self-similarly and the central density and velocity dispersion as follows analytical solution.We also initialize the simulation and the one-dimensional numerical cal-

culation of the conducting fluid model with the Plummer's model, the Hernquist profile and the Navarro-Frenk-White (NFW) profile to show that the fluid model is applicable to more realistic density profiles. The central density at maximum core expansion and the collapse time agree to within 20% in the long mean free path regime.

As the mean free path becomes comparable to the system size, we see the delay in collapse rate as predicted by BSI. In this transitional regime, the collapse time as a function of cross section agrees between the Monte Carlo N-body and the conducting fluid model, if another prefactor of thermal conduction, for the short mean free path effect, is set to $b = 0.25$. The functional form of thermal conduction by BSI agrees with Monte Carlo simulations in the long and intermediate mean-free-path regime.

Monte Carlo N-body simulation and conducting fluid model agree with each other if two prefactors of thermal conduction C and b are calibrated by the N-body simulation. We demonstrate that the two methods agrees with each other reasonably well, and their methods themselves are not the source of inconsistency in the magnitude of cross sections necessary to have a cored profile. In this and next chapter, the collision is assumed to be isotropic and velocity independent. The methodology details of the Monte Carlo N-body simulations are described in Chapter 4.

2.1 Comparison Setup

2.1.1 Definitions

We use the following characteristic scales in the rest of this chapter. For the self-similar solution and the Plummer model, we describe densities and velocities in units of central quantities, $\rho_c(t) \equiv \rho(0,t)$ and $v_c^2(t) \equiv v^2(0,t)$; $\rho(r,t)$ and $v(r,t)$ denote the density and the one dimensional velocity dispersion, respectively, in spherical symmetry. We use core radius $r_c(t) \equiv v_c/\sqrt{4\pi G\rho_c}$ as a standard length scale.

For Hernquist and NFW profiles, which have singularities at the center, we use the scale radius r_s and density ρ_0 that appear in the density profiles (Eqs. 2.9 & 2.10) as units, instead. We use $v_0 \equiv r_s\sqrt{4\pi G\rho_0}$ as the velocity scale, which is similar to the definition of the core radius above.

The local relaxation time is defined as $t_r(r,t) \equiv 1/(a\rho\sigma v)$ where the constant $a \equiv \sqrt{16/\pi} \approx 2.26$ describes the collision rate of particles that follow a Maxwellian distribution, defined in BSI. The relaxation time at the center $t_{r,c}(t) \equiv t_r(0,t)$ or $t_{r,0} \equiv 1/(a\rho_0\sigma v_0)$ are used as unit time-scales.

We express cross sections in a dimensionless way $\hat{\sigma}_c \equiv \rho_c\sigma r_c$ and $\hat{\sigma}_0 \equiv \rho_0\sigma r_s$, where σ is the scattering cross section per unit mass. The inverses are the Knudsen numbers (Kn), the mean free path in the unit of system size (r_c or r_s). From simple dimensional analysis, one can see that the evolution of the system is characterized by Kn only, independent of the scale.

2.1.2 Self-Similar Solution of Gravothermal Collapse

We first compare a result of Monte Carlo N-body simulation with the self-similar solution of the conducting fluid model derived by BSI; we review the BSI self-similar solution in this section.

In the large Knudsen number limit $\lambda \gg H$, the quasi-static conducting fluid model (Eqs. 1.4, 1.6, 1.7, and 1.8) has a self-similar solution. When a self-similar solution exists with a reasonable condition that (a) the density is static as $r \to \infty$ and (b) the evolution time-scale $\rho_c/\dot{\rho_c}$ is proportional to the relaxation time at the center, $t_{r,c}(t) \equiv t_r(r=0,t)$, the central quantities evolve as,

$$\rho_c(t)/\rho_c(0) = (1 - t/t_{coll})^{-2\alpha/(3\alpha-2)}, \tag{2.1}$$

$$v_c^2(t)/v_c^2(0) = (1 - t/t_{coll})^{-(2\alpha-2)/(3\alpha-2)}, \tag{2.2}$$

$$t_{rc}(t)/t_{rc}(0) = 1 - t/t_{coll}, \tag{2.3}$$

for some constants α and t_{coll}, by dimensional analysis [LBE]. The exponents of $t - t_{coll}$ depend on the form of the relaxation time; therefore the exponents above, for the hard sphere cross section, are different from those in [LBE] for stellar Rutherford scattering. By solving an eigenvalue problem of a system of ordinary differential equations, BSI obtained the value of the constants,

$$\alpha = 2.190, \tag{2.4}$$

$$t_{coll} = 290\, C^{-1} t_{r,c}(0). \tag{2.5}$$

We show in § 2.2.1 that this self-similar solution agrees very well with the self-similar time evolution in the Monte Carlo N-body simulation, if we fit the free parameter C with the simulation.

For non-self-similar profiles, we must integrate the time evolution of fluid variables ρ and v^2 numerically by alternative steps of the heat conduction and adiabatic relaxation to hydrostatic equilibrium, as described in BSI. We compare numerical results of the conducting fluid equations with those of Monte Carlo N-body simulations in §§ 2.2.2-2.2.4.

2.1.3 The Monte Carlo N-body Simulations

We generate the particle initial conditions randomly from the distribution functions $f(E)$ using the rejection method [1, 87]. The distribution function of the BSI's self-similar solution and the NFW profile are calculated numerically by Eddington's formula [23]. The distribution functions of the Plummer model and the Hernquist Model [82] have known analytical form. We set the initial center-of-mass velocity to zero by over-all boost.

We truncate the initial profile at some radius r_f, and put a simple reflection boundary, which flips the direction of the radial velocity if particles are moving outward outside the reflection boundary. We use $r_f = 600\, r_c$ for BSI self-similar profile, $r_f = 58.5\, r_c$ for Plummer model, and $r_f = 100\, r_s$ for Hernquist and NFW profiles. Density at r_f is smaller than $2 \times 10^{-7} \rho_c$, and the heat flux (Eq. (1.7)) at r_f, calculated from the equation for conducting fluid model, is smaller than 0.02% of its maximum value. Collapse time is sometimes sensitive to the position of the

reflection boundary. The collapse was slower by a factor of two when we first used truncation radius $r_f = 58.5\,r_c$ for the BSI profile. The truncation radius is large enough for the nearly isothermal profile to have gravothermal catastrophe (Antonov's criterion, [57]), but not large enough to avoid artificial effects of the boundary condition. We test $r_f = 300\,r_c$ for the self-similar solution, and the collapse time only change by 3% compared to $r_f = 600\,r_c$.

We use two time step criteria such that the time step must satisfy $\Delta t \leq \eta_v v_c(0)/a$, and $\Delta t \leq \eta_G/\sqrt{G\tilde{\rho}}$, where $v_c(0)$ is the initial one-dimensional velocity dispersion, a is the local gravitational acceleration, and $\tilde{\rho}$ is the local density calculated form $n = 32$ nearest neighbors (see below Eq. 4.6). We choose the dimensionless parameters to be $\eta_v = 0.02$ and $\eta_G = 0.005$. With this choice the initial conditions are static for several dynamical time when scattering is turned off. The energy conservation is better than 1% in all runs.

Number of particles, gravitational softening length and other parameters are summarized in Table 2.1. For simulation cases BSI and PLM, we reset the gravitational softening length ϵ to $0.1r_c$ every time the central density increases by a factor of 10, to avoid the numerical effect of softening on the density profile.

We tested that the scattering rate is correct, by counting the number of scatterings in the simulation of a non-singular isothermal sphere[1] and comparing it to the analytical rate. The scattering rates agree to within 3% when 64^3 particles are used and the isothermal sphere is truncated at $58.5\,r_c$. The difference is due to the

[1]The solution of hydrostatic equilibrium (eq. 1.8) with constant $v(r) \equiv v_c$ and finite central density.

fluctuation in the randomly generated initial conditions, not to the Poisson noise in the number of scatterings.

To test convergence, we simulated the self-similar solution (§2.2.1) with three different numbers of particles, 2×32^3, 4×32^3, and 16×32^3, which gives the number of particles inside the core $N_c = 227,376$ and $1,527$, respectively. At the time of our resolution test, we used reflection radius $r_f = 58.5\, r_c$. Numerical errors due to finite number of particles should only depend on the N-body particle density, independent of the choice of boundary condition. As a result, it was not necessary to run additional convergence test for the case with $r_f = 600 r_c$, used in our final runs. Other parameters are the same as run BSI. In Fig. 2.1, we plot the evolution of density and number of particles inside the core as a function of time. For visual clarity, the density plots are shifted left by 50 and shifted up by a factor of two. Three smooth curves in the left panel are the same analytic self-similar solution (Eq. (2.1)) with $t_{coll} = 705 t_{r,c}(0)$. The $N = 4 \times 32^3$ run and the $N = 16 \times 32^3$ run agree very well, $N = 2 \times 32^3$ run deviates from other two runs systematically when $N_c \lesssim 100$.

2.1.4 Analysis of N-body Data

We calculate the central quantities for each snapshot from N-body particles within radius r_c, around the density weighted center of mass [38], assuming an isothermal sphere inside r_c. Namely, we find a consistent r_c iteratively that satisfies,

$$r_c = \sqrt{v_c^2 / 4\pi G \rho_c}, \tag{2.6}$$

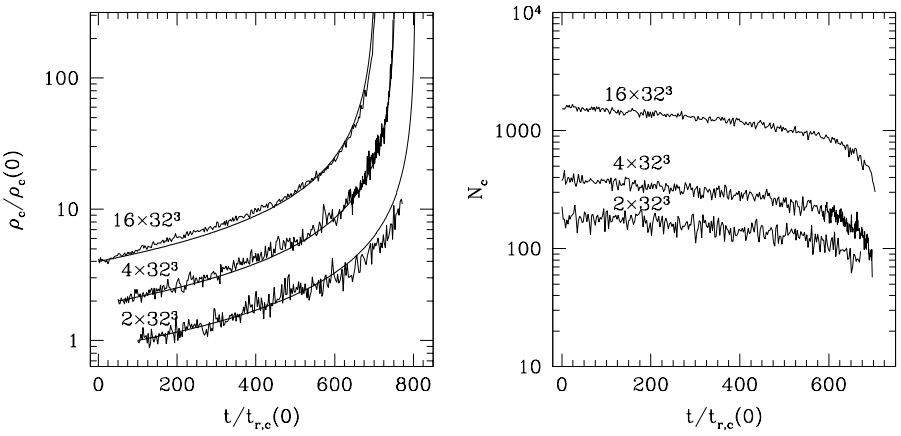

Figure 2.1: Simulation with different number of particles. Density and Mass deviates systematically when $N_c \lesssim 100$. Collapse time is different from run BSI because the reflection boundary is set at $58.5\,r_c$.

where ρ_c is the central density estimated from $M(r_c)$, the mass inside r_c,

$$\rho_c \equiv 1.10 \times M(r_c) / \frac{4}{3}\pi r_c^3, \tag{2.7}$$

and v_c is the velocity dispersion inside r_c. The value 1.10 in Eq. (2.7) is the ratio of the central density to the average density inside r_c for the isothermal sphere. In this way we can use as many particles as possible without systematic error for the calculation of the central quantities. The velocity dispersion inside the core quickly become isothermal due to collisions.

We calculated the density and velocity dispersion profiles by adaptive smoothing approach with each N-body particle assigned a spherically averaged Gaussian kernel [e.g, 149], with the kernel size equal to r_{32}, the distance to its 32nd nearest-neighbor particle.

2.2 Results

2.2.1 Self-Similar Solution

In this section, Monte Carlo N-body simulation for large Kn is compared with the BSI self-similar solution The time evolution for this quasi-static system is independent of the actual value of σ for the large Kn regime, if the time for solutions with different σ is expressed in units of the relaxation time. We used a small enough cross section, $\hat{\sigma}_c(0) = Kn^{-1} = 0.067$ for the N-body, here. (We discuss the Kn dependence in § 2.2.2.)

Fig. 2.2 shows the time evolution of the density and velocity dispersion profiles in the Monte Carlo N-body simulations. The right panels, plotted in self-similar variables, show that the self-similar solution indeed evolves self-similarly in the N-body simulation.

Our Monte Carlo N-body simulation is in excellent agreement with the self-similar solution, Eqs. (2.1)-(2.5), by choosing one parameter C (Fig. 2.3). We determine the collapse time $t_{coll} = 385\, t_{r,c}(0)$ by fitting the time evolution of the relaxation time data (Fig. 2.3, left-bottom panel) by the linear function, Eq. (2.3). The prefactor of the thermal flux $C = 0.75$ follows from Eq. (2.5). The best-fitting power law index of $v_c^2 \propto \rho_c^{(\alpha-2)/\alpha}$ (Eqs. 2.1, 2.2) gives a value $\alpha = 2.22$ (Fig. 2.3, right-bottom), which agrees reasonably well with the value of self-similar solution 2.19 (Eq. 2.4). Overall, the Monte Carlo N-body and the conducting fluid model agree very well in the self-similar collapse mode.

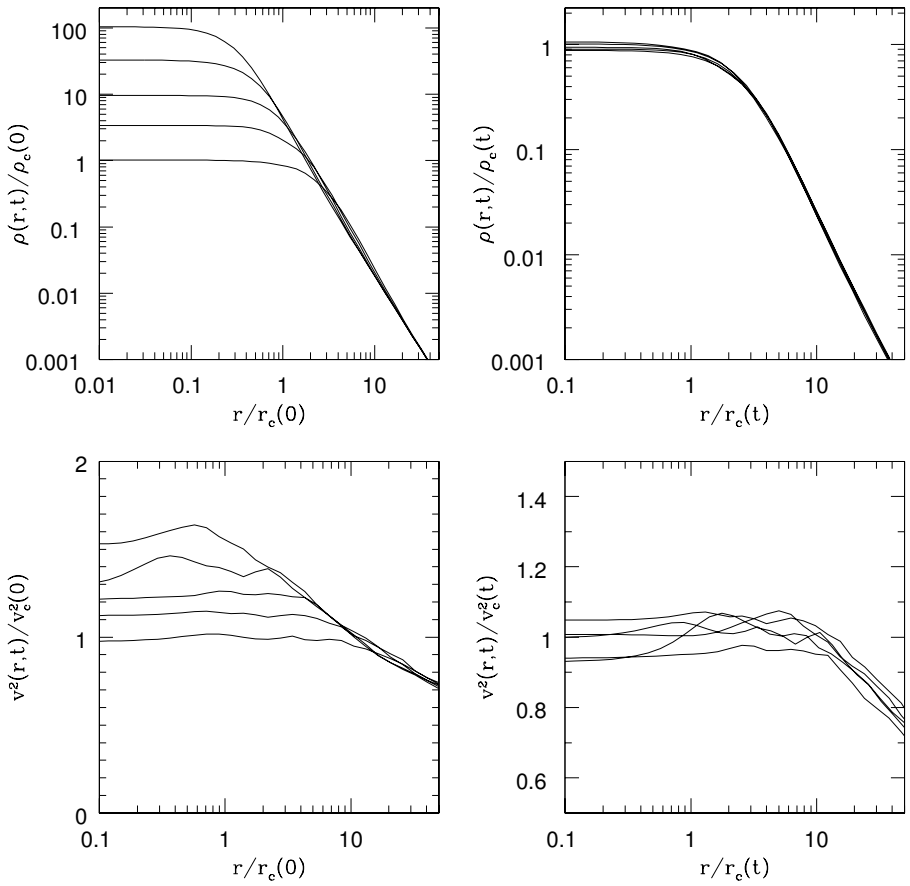

Figure 2.2: Density and velocity dispersion profiles of the N-body simulation for $\hat{\sigma}_c = 0.067$ plotted with fixed scales (*left*) and self-similar scales (*right*) at $t/t_{r,c} = 0, 275, 356, 376$ and 383. Initial condition is the self-similar solution. (*Right:*) The evolution is indeed self-similar.

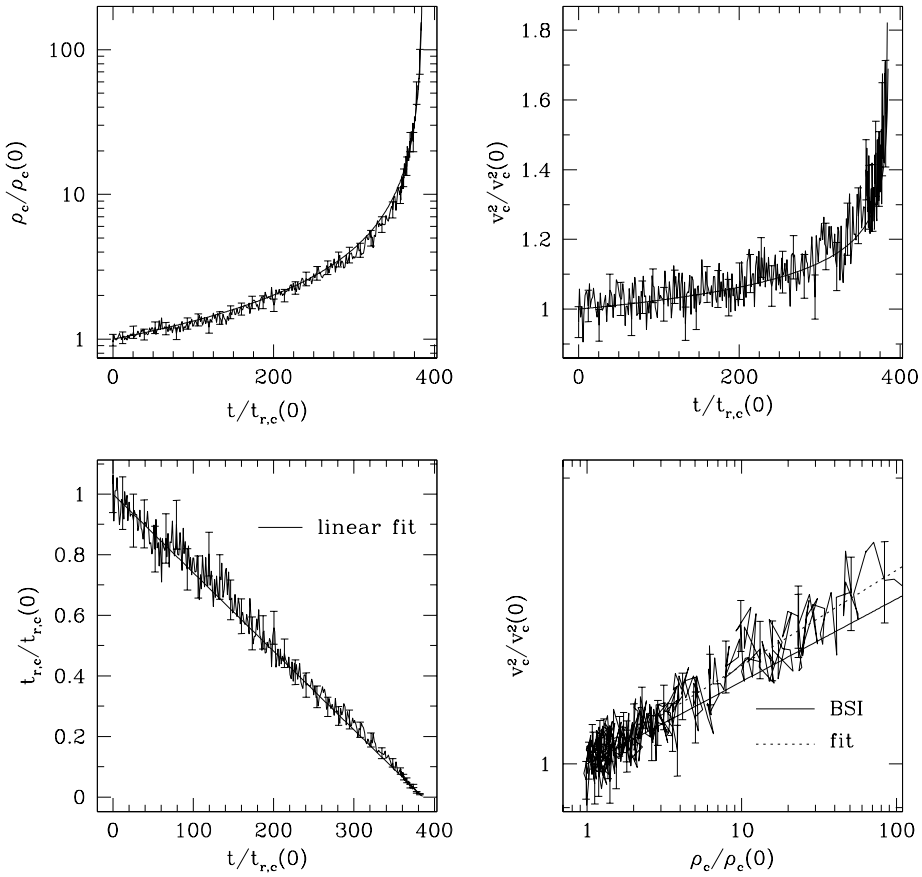

Figure 2.3: Central quantities plotted as a function of the time for $\hat{\sigma}_c = 0.067$. N-body results are in good agreement with the self-similar solution (smooth curves, Eqs. (2.1) - (2.4)), with $t_{coll} = 385 t_{r,c}(0)$ or $C = 0.75$. Fluctuations are of order Poisson noise. Error bars represent $\Delta\rho/\rho = \Delta t_{r,c}/t_{r,c} = 2/\sqrt{N_c}$, and $\Delta v^2/v^2 = 1/\sqrt{N_c}$ where N_c is the number of particles inside r_c.

2.2.2 Evolution in the Transitional Regime

When Kn becomes comparable to or smaller than one, the solution is no longer consistent with the self-similar behavior derived in the long mean free path limit, because of the short mean free path effect – second term in the heat conduction equation (1.3). We run Monte Carlo N-body simulations with initial Knudsen number $Kn^{-1}(0) = \hat{\sigma}_c(0) = 0.25, 0.5, 0.75$ and 1.0 initialized by the BSI self-similar solution, and compare with the conducting fluid model computed numerically by a 1D quasi-static code. Number of particles are 4×64^3 for $\hat{\sigma}_c = 0.25, 0.50$ and 2×128^3 for $\hat{\sigma}_c = 0.75, 1.0$. Other parameters are the same as run BSI. N-body simulation with larger $\hat{\sigma}_c$ become seriously difficult because of the mean free path must be longer than the particle separation length scale (we will discuss at Eq. (4.8) in § 4.2). Our $\hat{\sigma}_c(0) = 1.0$ run violates $\lambda > r_{32}$ at $\rho_c(t) \sim 7$. Required number of particles scales as $\hat{\sigma}_c^3$ beyond this density or cross section.

For the fluid model, the prefactor C is chosen to be 0.75 to make an agreement at small $\hat{\sigma}_c$ (§2.2.1). We run the fluid code with initial dimensionless cross section $\hat{\sigma}(0)/\sqrt{b} = 0, 0.25, 0.5, 0.75, 1.0, 1.5$ and 2.0. The time evolution of fluid model in the unit of initial relaxation time depends only on the combination $\hat{\sigma}/\sqrt{b}$, which can be seen from the heat conduction Eq. (1.3).

We plot the evolution of the central density for both N-body and fluid model in the left panel of Fig. 2.4. In the unit of relaxation time, the collapse is slower for larger cross section. Fluid model with $\hat{\sigma}/\sqrt{b} = 0.5, 1.0, 1.5$ and 2.0 evolve similar to N-body simulation with $\hat{\sigma} = 0.25, 0.5, 0.75$ and 1.0, respectively. This suggest that the effective value of the coefficient is $b = 0.25$ in the transitional regime

$Kn \gtrsim 1$.

To show the agreement between our N-body and the fluid model with $b = 0.25$, we plotted the normalized collapse rate as a function of cross section in the right panel of Fig. 2.4, where t_{10} is the time that the density increase by a factor of ten, and the fiducial time scale t_{10}^* is the time that the self-similar solution with $\hat{\sigma}_c(0) = 1$ has a density increase by a factor of ten. The collapse rate is proportional to the cross section in the large Kn regime (small $\hat{\sigma}$)), but deviates from the linear relation in the transitional regime $\hat{\sigma} \gtrsim 0.5$, as predicted by BSI. The collapse rate should reach some maximum at some cross section and then decreases as $t_{10}^{-1} \propto \hat{\sigma}_c^{-1}$ as $\hat{\sigma}_c \to \infty$. Furthermore, since the value of b can be calculated from first principal in small Kn regime, b should converge to the Chapman-Enskog value (b=1.38 in § 1.3.3) as $Kn \to 0$. However, due to the numerical limit in Eq. (4.8), we cannot go into the small Kn regime to see the convergence to the Chapman-Enskog theory or the turn over of the collapse rate. Our N-body results are consistent with a constant $b \equiv 0.25$ in the range we are able to simulate.

2.2.3 Plummer Model

We also compare the Monte Carlo N-body simulation with the conducting fluid model when the initial condition is the Plummer model in the large Kn regime. Plummer model is a standard initial condition to study gravothermal instabilities.

$$\rho(r) = \frac{M_T}{4\pi a_{pl}^3/3} \frac{1}{(1 + r/a_{pl})^{5/2}} \tag{2.8}$$

The characteristic scales defined in § 2.2.1 can be calculated as, $a_{pl} = 3\sqrt{2}r_c$ and $v_c = (2GM_T/a_{pl})^{1/2}/12$. Conducting fluid model is calculated in the large Kn

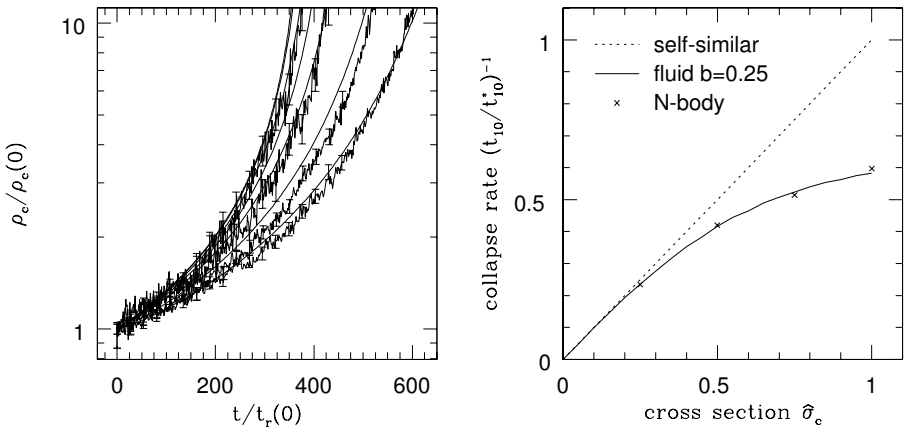

Figure 2.4: (*Left:*) Central density against time from N-body simulation and the conducting fluid model in the transitional regime. Cross sections of N-body are $\hat{\sigma} = 0.25, 0.50, 0.75$ and 1.0, from left to right. The cross sections of the fluid model are $\hat{\sigma}/\sqrt{b} = 0, 0.25, 0.5, 1.0, 1.5$ and 2.0, from left to right. First two curves, $\hat{\sigma}/\sqrt{b} = 0, 0.25$, are indistinguishable, and $\hat{\sigma}/\sqrt{b} = 0.5, 1.0, 0.15$ and 2.0 overlap with the N-body with $\hat{\sigma} = 0.25, 0.5, 0.75$ and 1.0 respectively. (*Right:*) Collapse rate plotted as a function of cross section for self-similar solution (dotted line), fluid model with $C = 0.75, b = 0.25$ (solid line) and N-body (crosses). See text for the definition of the collapse rate. Due to the short mean free path effect, the evolution deviates from the self-similar solution. $b = 0.25$ gives the transitional effect that agree with N-body simulations.

limit, $\hat{\sigma}_c \to 0$, and the N-body simulation is performed in the large Kn regime, $\hat{\sigma}_c(0) = 0.013$. Time evolution is independent of the actual value of σ for the large Kn regime, if the time is expressed in units of the relaxation time.

We plot the time evolution in Fig. 2.5. The fluid model agrees with the N-body reasonably well if the coefficient $C = 0.80$ is used. Considering the statistical fluctuation in the randomly generated initial condition, this is in reasonably good agreement with the value of $C = 0.75$ found in the self-similar solution. The logarithmic slope (right-top panel) has a plateau at about $-\alpha$, which is the asymptotic slope of the self-similar profile. This implies that the inner part is converging to the self-similar solution, with an asymptotic logarithmic slope $-\alpha$, which was well known in the gravothermal collapse of star clusters.

2.2.4 NFW & Hernquist Profile

We run a simulation with NFW profile [142] to see the consistency of the Monte Carlo N-body simulation and the conducting fluid model for the typical profile seen in cosmological N-body simulations. NFW profile is,

$$\rho(r) = \rho_0 \frac{1}{r/r_s(1+r/r_s)^2}. \tag{2.9}$$

We also simulate with Hernquist profile [82],

$$\rho(r) = \rho_0 \frac{1}{r/r_s} \frac{1}{(1+r/r_s)^3}, \tag{2.10}$$

which has the same inner profile $\rho \propto r^{-1}$ and sometimes used to approximate NFW profile. As for the Plummer model, our large Kn limit simulations adopt $\sigma \to 0$ for the fluid model and a small finite σ for the N-body simulations (cf. Table 2.1).

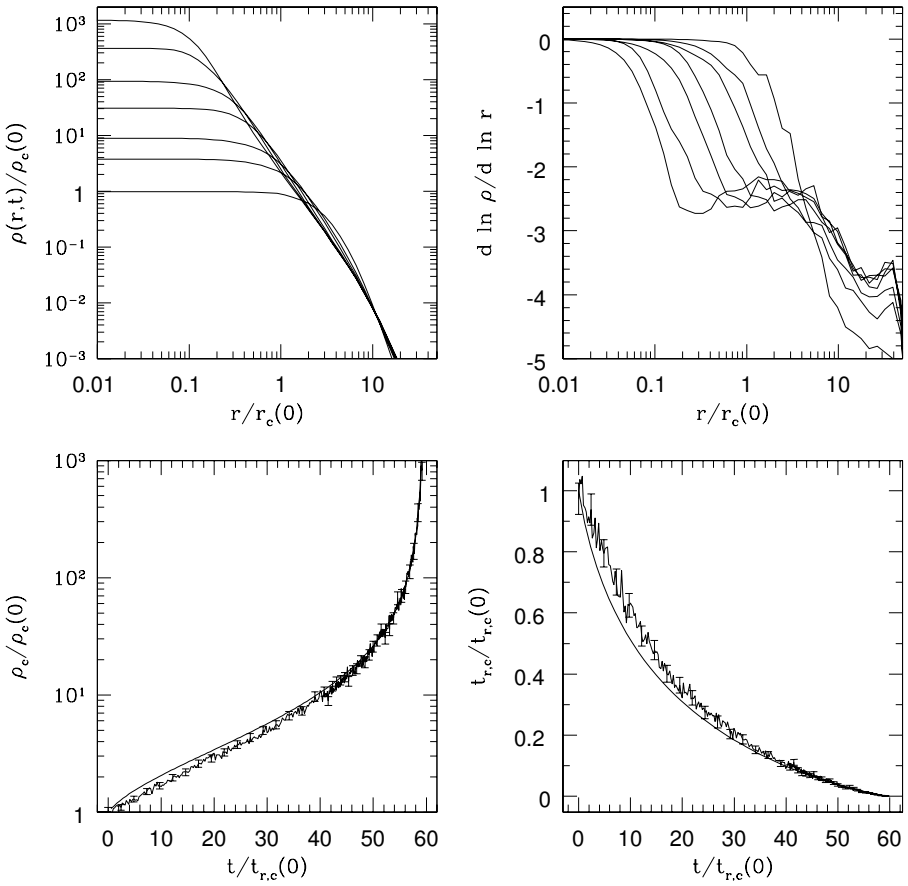

Figure 2.5: Collapse of the Plummer model for $\hat{\sigma}_c(0) = 0.013$. *Top:* Snapshots of the Monte Carlo N-body simulation, taken at $t/t_{r,c}(0) = 0.0, 24.338.552.0, 56.7, 58.6,$ and 59.3. *Bottom:* Central density and relaxation time evolution as a function of time for N-body and 1D calculation of the fluid model with $C = 0.8$ (smooth curve).

The evolution of density profile and center quantities result from both N-body and conducting fluid model is plotted in Figs. 2.6 and 2.7. Density profiles agree very well when the central densities are equal, but the value of the central density differ about 20% at the maximum core expansion. The agreement is reasonably well in the gravothermal collapse phase after the maximum core expansion. The differences in the collapse times are also about 20%, inherited from the difference at the maximum core expansion. The $100\,t_{r,0}$ shift in the left panels of Fig. 2.7 is about 20% of the collapse time, and the value of $C = 0.9$ used in the run HQS differ 20% compared to 0.75 in the run BSI.

We note that the initial NFW profile evolves very differently from the initial Hernquist profile, for the same parameters ρ_0 and r_s. The run NFW has about three times smaller central density at maximum core expansion, and about four times longer collapse time than the run HQS. This is because the NFW profile has larger heat flux at $r \gtrsim r_s$ due to its larger density, which heats and expands the center more than the Hernquist profile.

Our simulation results are qualitatively similar to those of Kochanek & White [102] , but the time evolution differs by a factor of two. Their unit corresponds to $\rho_0^{\rm KW} = 2\pi\rho_0$, $t_{r,c}^{\rm KW} = 1.7 \times 2\sqrt{2}at_{r,0} = 11\,t_{r,0}$ and $\hat{\sigma}_{DM}^{\rm KW} = 2\pi\hat{\sigma}_0$. Their $\hat{\sigma}_{DM}^{\rm KW} = 1$ simulation, which has the same cross section as ours, reach minimum density at $t \approx t_{r,c}^{\rm KW} = 11t_{r,0}$ and collapse gravothermally to $\rho_C = 2\rho_0^{\rm KW} = 13\,\rho_0$ at $t \approx 3.2t_{r,c}^{\rm KW} = 35\,t_{r,0}$ while our simulation reach those densities at $20\,t_{r,0}$ and $70\,t_{r,0}$, respectively (Fig. 2.7). Their evolution is about twice as fast as our simulation. For other cross sections, their collapse time did not simply scale as $\hat{\sigma}^{-1}$ for $\hat{\sigma}_{DM}^{\rm KW} = 3$

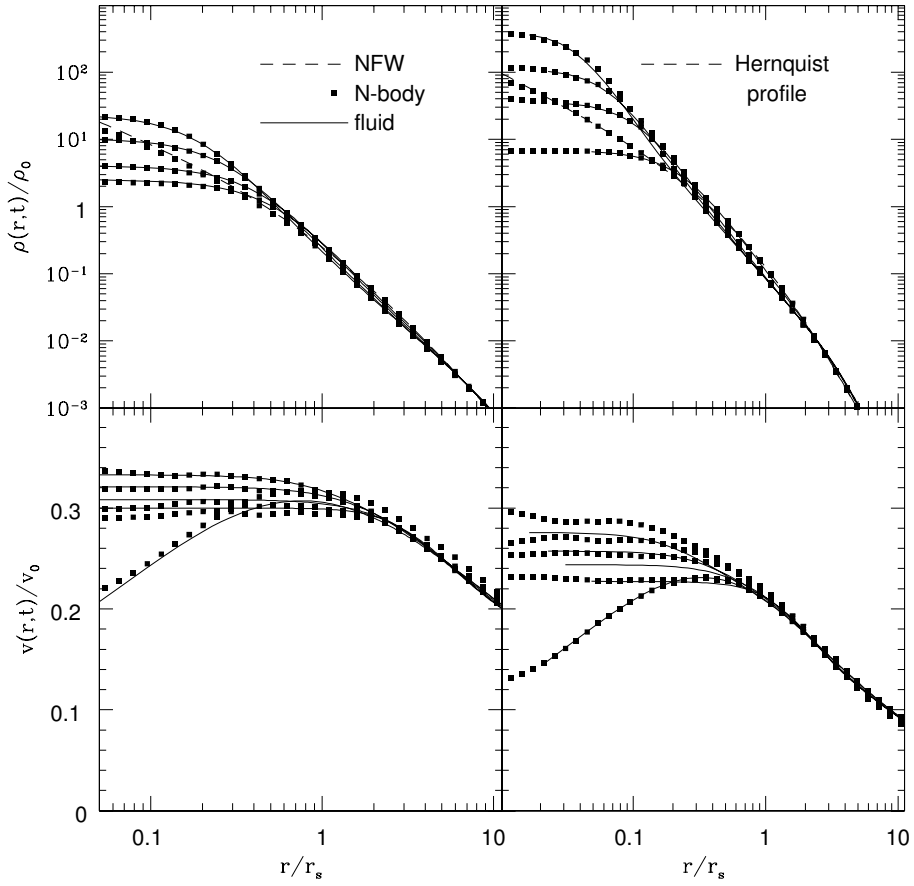

Figure 2.6: The density and velocity dispersion profiles. (*Left:*) N-body snapshot with NFW initial condition at $t/t_{r,0} = 0, 197, 336, 462$ and 515, and profiles of the fluid model when they have the same central density. (*Right:*) Same with Hernquist profile initial condition at $t/t_{r,0} = 0, 16, 111, 129$ and 139.

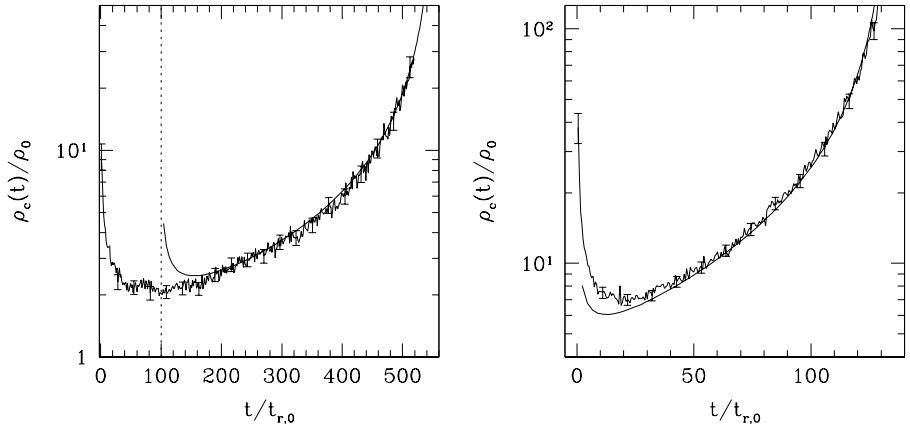

Figure 2.7: Central density against time, started from NFW (*left*) and Hernquist profile (*right*). We use $C = 0.75$ for NFW and $C = 0.9$ for Hernquist profile. The origin for the fluid curve is shifted by $100t_{r,c}$ in the left panel to show the agreement in the gravothermal collapse phase. Minimum density of the fluid is $\pm 20\%$ different from N-body. This is the source of difference in the collapse time.

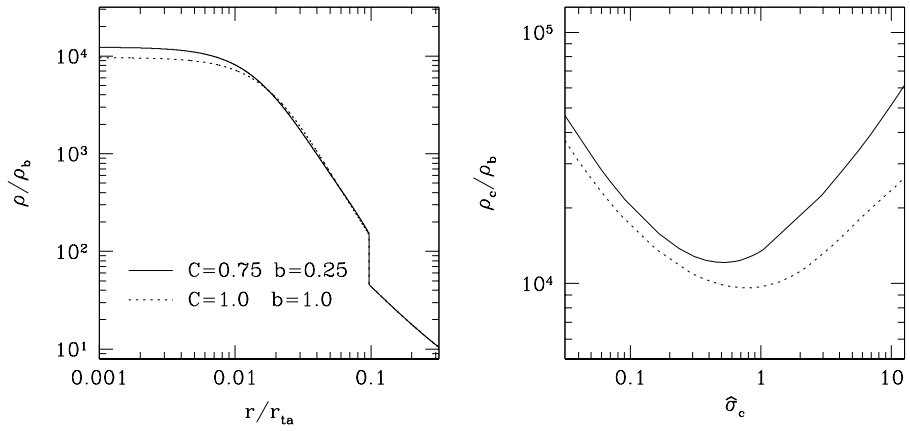

Figure 2.8: The cosmological similarity solution by Ahn & Shapiro [4] with our calibrated prefactors (C=0.75, b=0.25; solid lines) and the original prefactors (C=b=1.0; dotted lines). (*Left:*) The maximally relaxed density profile in the unit of background critical density ρ_b and turn around radius $r_{\rm ta}$. The maximum relaxed solution for new prefactors has a 25% larger central density. (*Right:*) The central density for different cross section.

and 10, but this is consistent qualitatively with the conductivity suppression in the transitional regime (§2.2.2); at maximum core expansion ($\rho_c \approx 7\rho_0$, $v_c \sim 0.5v_0$ and $r_c \sim 0.2r_0$) cross sections $\hat{\sigma}_{DM}^{\rm KW} = 3$ and 10 correspond to Knudsen numbers $Kn \sim 1.7$ and 0.2, respectively, which are in transitional regime ($Kn \lesssim 1$).

2.3 Discussions

2.3.1 Implications on the Cosmological Similarity Solution

In this section, we discuss the consequence of prefactors $C = 0.75$ and $b = 0.25$, calibrated by our Monte Carlo N-body simulations, on the cosmological similarity solution derived by Ahn & Shapiro [4, hereafter, A&S].

The BSI heat conduction, Eq. (1.3), has a $\hat{\sigma} = H/\lambda$ dependence,

$$L \propto \hat{\sigma} \left(a^{-1}C^{-1} + b^{-1}\hat{\sigma}^2 \right)^{-1}. \tag{2.11}$$

This function on the right hand side takes its maximum value $\sqrt{abC}/2$ at $\hat{\sigma} = \sqrt{a^{-1}b\,C^{-1}}$. Compared to previously assumed values, $C = b = 1.0$, our calibrated heat conduction has a factor $\sqrt{bC} \approx 0.4$ smaller maximum at a factor $\sqrt{bC^{-1}} = 0.58$ smaller $\hat{\sigma}$.

A&S applied the BSI heat conduction (Eq. 1.3) to a secondary infall model with a spherically symmetric power law over density, $\delta M/\bar{M} \propto \bar{M}^{-1/6}$, that models a cosmological accretion; $\bar{M}(r)$ is the cosmological average mass inside radius r, and $\delta M(r) = M(r) - \bar{M}(r)$ is the mass perturbation inside the radius. The solution is self-similar, that is, the solution is time independent if the radius and the density are measured in units of turn-around radius $r_{\rm ta}$ and critical background

density ρ_b, respectively, in the flat matter-dominated (Einstein-de Sitter) universe. The family of similarity solutions are parametrized by the dimensionless cross section $Q \equiv \rho_b \sigma r_{\rm vir}$, where $r_{\rm vir}$ is the halo virial radius, where the accretion shock occurs. The density profile has a minimum central density and largest core size approximately when the dimensionless cross section at the center $\hat{\sigma}_c$ maximizes the heat flux with the value, $\hat{\sigma}_c = \sqrt{a^{-1} b\, C^{-1}}$ (Eq. 2.11). The solution with that $\hat{\sigma}_c$ is defined as the maximally relaxed solution, and the corresponding cross section Q is denoted by $Q_{\rm th}$. The maximally relaxed halo has a density profile almost identical to the empirical Burkert profile [36], which fits observed rotation curves of dwarf and LSB galaxies well. It is also almost identical to that of the equilibrium, nonsingular, truncated isothermal sphere (TIS) model derived analytically by [158]

We used the same numerical code as A&S to solve the similarity solutions with our calibrated prefactors. In Fig. 2.8, we plot the maximally relaxed density profile on the left panel, and plot the cross section dependence of the central density. The solution is maximally relaxed at $Q = Q_{\rm th} = 4.60 \times 10^{-4}$, with a central density $\rho_c = 1.23 \times 10^4 \rho_b$ (similar to the central density of the TIS solution $1.8 \times 10^4 \rho_b$). This central density is about 25% larger than the original maximally relaxed solution with prefactors ($C = b = 1.0$). For $\hat{\sigma} \ll 1$, a factor 0.75^{-1} times larger cross section is required to achieve the same central density, due to the change of coefficient C from 1.0 to 0.75.

Using the same argument as A&S, the $Q_{\rm th}$ value corresponds to a cross section 137 cm^2 g^{-1}, if dwarf galaxies have maximally relaxed profiles. This is slightly smaller than the original value 218 cm^2 g^{-1}, but still much larger than the

values, $0.5 - 5\,\mathrm{cm}^2\,\mathrm{g}^{-1}$, used in Monte Carlo N-body simulations that produce cored profiles [42, 46].

As we shall show elsewhere, the essential difference between the self similar solution and the cosmological N-body simulations is that the self-similar halo is continuously heated by the accretion shock associated with the supersonic infall of additional mass onto the virialized region of the halo, while the inner parts of more realistic haloes on the galaxy scale are unaffected by infall once the mass supply tapers off [34, 84]. We will discuss why self-similar solution requires significantly larger cross section to have maximal relaxation in our following chapter, using Monte Carlo N-body simulations with cosmological initial conditions.

2.3.2 The Source of Difference

Our Monte Carlo N-body simulations agree with the solutions of conducting fluid model in the self-similar gravothermal collapse phase, but in general have about 20% difference in the central density and the collapse rate. This disagreement is not surprising because the conducting fluid model is not an exact theory derived from first principal. Heggie & Stevenson [80] compared the thermal conductivity of the conducting fluid model for gravitational scattering with that calculated from orbit-averaged Fokker-Plank equation for star clusters with several profiles, polytrops and lowered Maxwellian, at the center, and find that coefficient of conductivity, C, differs by a factor of 2 or 3. Overall collapse rate is not that different, probably because the profiles quickly converge to the self-similar solution around the center. Indeed, for star clusters, the value of $C = 0.88$ (with Spitzer's definition

of relaxation time) which is adjusted to give the asymptotic collapse rate in isotropic Fokker Plank calculation [41] also gives the correct collapse time of the Plummer model [68, 79], which means that C needs not to be different between self-similar solution and the collapse of Plummer model. The conducting fluid model has been shown to describe the gravothermal collapse relatively accurately, but we cannot expect high precision, in general. 20% match in the core expansion phase of run NFW or HQS is a reasonable agreement.

Anisotropy in velocity dispersion affects the collapse time as well [21, 119]. Fokker-Plank calculation with anisotropy shows that the collapse time of the star clusters initialized by Plummer model is 20% larger compared to an isotropic one [169], and agrees with N-body simulation [100]. In Fig. 2.9, we plot the radial (v_r^2), and tangential ($v_\perp^2 = (v_\theta^2 + v_\phi^2)/2$) velocity dispersion of our simulation when the central density increase by a factor of ten. We do not see anisotropies near the center, but we do at $r \gtrsim 5r_c$ for run PLM, NFW and HQS. Anisotropy is larger if the logarithmic slope of the density profile is steeper. This is simply because the number of scattered anisotropic particles is larger relative to that of native isotropic particles at large radii for steeper density profiles. Anisotropy may play some role in the collapse rate of run PLM and HQS.

2.4 Conclusion

We compare the Monte Carlo N-body simulations with the conducting fluid model for isolated, spherically symmetric self-gravitating SIDM haloes. The collisions were assumed to be velocity independent, elastic and isotropic.

- The evolution of the N-body simulation is in very good agreement with the self-similar solution, using a coefficient of thermal conduction $C = 0.75$. The time to collapse is always proportional to the central relaxation time at that time t, $t_{coll} - t = 390\, t_{r,c}(t)$.

- The conducting fluid model agrees with the Monte Carlo N-body simulations reasonably well for different initial conditions, including Plummer Model, Hernquist profile and NFW profile. The collapse time and the central density at the maximum core expansion agree to within 20%. The shape of the density profile and the central density evolution as a function of time during gravothermal collapse agree very well.

- We also showed that the collapse time becomes longer in units of relaxation time as the system transits from large to small *Kn* regime. The N-body results agree with the conducting fluid model for $\mathrm{Kn} \gtrsim 1$, or $\hat{\sigma} \leq 1$, with the prefactor $b = 0.25$. However, this prefactor is more than five times smaller than the Chapman-Enskog value, valid in the small *Kn* limit. Conducting fluid model must be calibrated against N-body simulations if it is used in the transitional regime beyond $\hat{\sigma} = 1$.

- Our calibration of the prefactors C and b does not change the cosmological similarity solutions of Ahn & Shapiro [4] significantly. The cross section that gives the maximally relaxed SIDM profile in the dwarf galaxy scale is altered from 220 $\mathrm{cm^2 g^{-1}}$ to 140 $\mathrm{cm^2 g^{-1}}$, but this is still much larger than the values that cosmological Monte Carlo N-body simulations use to make cored

SIDM haloes ($\sigma \sim 0.5 - 5$ cm^{2}g^{-1}). We will investigate this problem in our subsequent chapter. Our results here suggest that this apparent discrepancy is not the result of either a break-down of the conducting fluid model or the Monte Carlo scattering algorithm in the N-body simulations. As we shall show in the next Chapter, the discrepancy results, instead, from the departure of halo evolution from self-similarity.

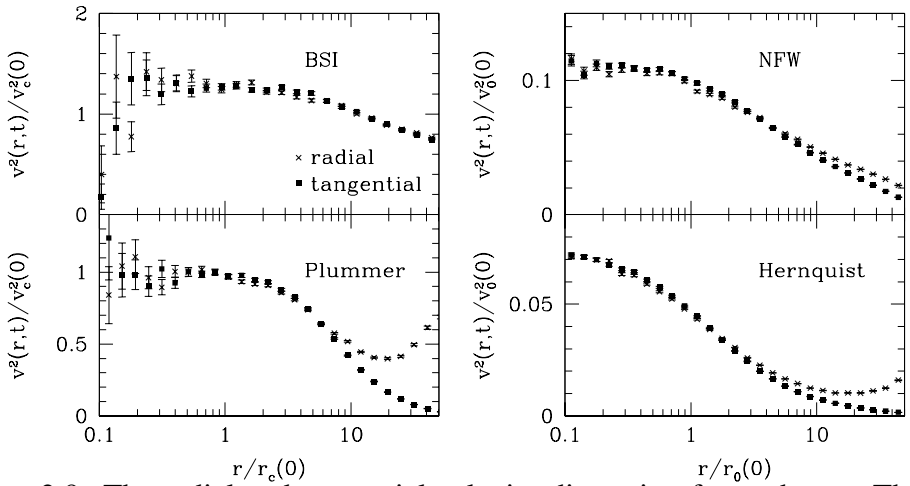

Figure 2.9: The radial and tangential velocity dispersion for each run. The snapshots are taken when the densities at the center are $10\rho_c(0)$ for run BSI and PLM, $25\rho_0$ for run NFW and $125\rho_0$ for run HQS. The velocity dispersion is calculated in 40 logarithmically equally spaced bins. The error bars show the Poisson error: $\Delta v^2 = v^2/\sqrt{N}$, where N is the number of particles in each bin.

name	initial condition	σ	N	$\max N_c$	r_f	ϵ	C
BSI	BSI self-similar	$\hat{\sigma}_c = 0.067$	4×64^3	473	$600\, r_c$	$0.1 r_c$	0.75
PLM	Plummer	$\hat{\sigma}_c = 0.067$	4×32^3	1455	$58.5\, r_c$	$0.1 r_c$	0.8
HQS	Hernquist profile	$\hat{\sigma}_0 = 0.16$	2×64^3	1493	$100\, r_s$	$0.03 r_s$	0.9
NFW	NFW profile	$\hat{\sigma}_0 = 0.088$	2×64^3	794	$100\, r_s$	$0.03 r_s$	0.75

Table 2.1: Parameters used for each run. N is the number of N-body particles, $\max N_c$ is the maximum number of particles inside the core, r_f is the radius of the reflection boundary, ϵ is the Plummer equivalent gravitational softening length, and C is the LBE prefactor used for the conducting fluid model.

Chapter 3

Comparison of Conducting Fluid Model with Monte Carlo N-body Simulations II: Cosmological SIDM halos

We clarify the origin of disagreement between N-body simulations with Monte Carlo scattering [42, 46] and the similarity solution of the conducting fluid model [4], on the value necessary for the SIDM scattering cross section to produce cored density profiles observed in dwarf spiral and Low surface brightness galaxies (c.f. § 1). We compare the results of cosmological Monte Carlo N-body simulations initialized by the standard random Gaussian field with those of one-dimensional numerical computation of the conducting fluid model with cosmological secondary infall, both in a Lambda Cold Dark Matter (ΛCDM) universe. The initial condition of the secondary infall is chosen such that the mass accretion history of a fluid halo agree with the N-body halo in comparison. With the common mass accretion history, the N-body and the fluid model agree with each other on the value of cross section that gives maximally relaxed cored profile.

The central density of SIDM halos decreases with time due to collisional relaxation. A reasonably good agreement is found for the degree of relaxation (the ratio of central density to that of maximum relaxation) as a function of time between the N-body and the fluid model for their computations with cosmological infall. On

the other hand, a factor of two difference is found for the values of the central densities at the maximum relaxation between the two; this could be due to a cumulative error in the fluid approximation (neglecting the third order moments, § 1.3.3), the departure from the isotropic velocity dispersion, and the inaccuracy of the LBE-BSI thermal conduction formula (Balberg, Shapiro, & Inagaki [13], Lynden-Bell & Eggleton [120]).

Our first objective of the thesis is to confirm the consistency of two approaches, Monte Carlo N-body and the conducting fluid model; we have achieved this with satisfaction: The value of the cross section necessary to have a sufficiently relaxed halo, and more generally, the degree of relaxational central profile flattening as a function of cross section are in agreement. The effect of the departure from self-similar halo formation, which was larger than previously thought, explains the previous disagreement between the two methods.

3.1 Cosmological Conducting Fluid Model

We numerically solve the one-dimensional partial differential equations of conducting fluid model, assuming spherical symmetry and the isotropic velocity dispersion in a ΛCDM cosmology.

3.1.1 Fluid Equations

Spherically symmetric cosmology in General Relativity can be formulated as a Newtonian dynamics [10, 28, 173]. A particle at radius r with radial velocity $u = \dot{r}$ and zero angular momentum satisfies energy conservation, if there is no force other

than gravity:

$$\frac{1}{2}u^2 - G\frac{M(r)}{r} - \frac{1}{6}G\Lambda r^2 = \text{const}, \tag{3.1}$$

where $M(r)$ is a mass enclosed within a sphere of radius r, and Λ is the cosmological constant. The equivalent equation of motion is

$$\dot{u} = -G\frac{M(r)}{r^2} + \frac{1}{3}G\Lambda r. \tag{3.2}$$

We combine this equation of motion with the conducting fluid equations (§ 1.3.3); we solve the motion of Lagrangian shells at radius r with radial velocity u, one-dimensional velocity dispersion v, mass density ρ, pressure $p = \rho v^2$ and internal specific energy $e = 3v^2/2$,

$$\dot{r} = u, \tag{3.3}$$

$$\dot{u} = -\frac{GM}{r^2} - \frac{\partial p}{\partial r} + \frac{1}{3}G\Lambda r \tag{3.4}$$

$$\frac{D}{Dt}e = -\rho p\frac{D}{Dt}\frac{1}{\rho} - \frac{1}{4\pi r^2}\rho\frac{\partial L}{\partial r} \tag{3.5}$$

where D/Dt is a Lagrangian derivative, and L is the BSI heat flux (Eq. (1.7)). We solve those equations with a simple one-dimensional Lagrangian hydrodynamics code by Ahn & Shapiro [5] with initial conditions set as in Alvarez, Ahn, & Shapiro [8][see e.g., 31, 171, for the numerical methods in detail].[1], chosen so that the mass infall onto the central object grows in non-self-similar way reported from N-body simulations of CDM.

[1] Although we use explicit method for solving the system of partial differential equations, the computation may be faster with an implicit method [e.g., 78], which allows a larger time step without numerical instabilities.

3.1.2 Initial Condition

As described in Alvarez, Ahn, & Shapiro [8], we setup initial conditions such that the virial mass $M_{\rm vir}$ of halos follows the Wechsler et al. [181] formula, defined below. The virial mass $M_{\rm vir}$ is defined as the mass enclosed by a sphere of radius $r_{\rm vir}$ in which the mean density is a factor $\Delta_{\rm vir}$ times the critical density $\rho_{\rm crit}$;

$$M_{\rm vir} = \frac{4}{3}\pi\Delta_{\rm vir}\rho_{\rm crit}r_{\rm vir}^3, \tag{3.6}$$

where $\Delta_{\rm vir} = \Delta_{\rm vir}(z)$ is a widely used fitting formula for the overdensity of virialized halo at redshift z in a spherical tophat model in a flat ΛCDM cosmology (Bryan & Norman [33]):

$$\Delta_{\rm vir}(z) = 18\pi^2 + 82x - 39x^2, \qquad x \equiv \Omega(z) - 1, \tag{3.7}$$

where $\Omega(z)$ is the ratio of cosmic mean matter density to critical density at redshift z. Because the mean density within a radius usually decrease monotonically with the radius, such $M_{\rm vir}$ is unique. The Wechsler et al. mass accretion history is a two parameter formula, derived as an empirical fit to N-body simulations of CDM:

$$M(a) = M_0\,\exp\left[-2a_c(a_0/a - 1)\right], \tag{3.8}$$

where $a = (1+z)^{-1}$ is the cosmological scale factor, M_0 is the halo mass at some scale factor a_0, and a_c is a parameter called formation time. The factor 2 is an arbitrary factor that defines the formation time a_c.

At a sufficiently high redshift z_i, at which the Hubble parameter is H_i, we locate each equal-mass Lagrangian shell at $r = r_i$ with Hubble velocity $u = H_i r_i$

and zero temperature $v^2 = 0$, so that the time integral of the equation of motion (3.2) gives the Wechsler et al. mass accretion history. The value of r_i is chosen by integrating the equation of motion numerically with two trial initial radii, followed by more trial initial radii using the bisection method. The initial redshift is checked to be large enough, by confirming that the innermost shell has not turned around (has outward velocity) by the initial redshift, which is a sufficient condition that the shell is not virialized, and therefore the cold initial condition ($v^2 = 0$) is appropriate.

3.2 Summary of N-body simulations

The results of our three-dimensional N-body Monte Carlo scattering simulation, which will be compared with the fluid model, are briefly summarized in this section. See Chapter 4 for the details of the simulations.

We first performed a low resolution collisionless CDM simulation with 256^3 particles in a periodic box with $70h^{-1}$Mpc in a side. The background cosmology is a standard flat ΛCDM cosmology with mean present matter density ratio $\Omega_m = 0.25$, $\Omega_\Lambda = 1 - \Omega_m = 0.75$, with a random Gaussian initial condition with the power spectrum $n_s = 1$, $\sigma_8 = 0.8$, and the BBKS transfer function. Then, we select two halos in the simulation data, one is a Milky-way sized halo with the mass $M_{\rm vir} = 1.4 \times 10^{12} h^{-1} M_\odot$ and the other is a galaxy-cluster sized halo $M_{\rm vir} = 2 \times 10^{14} h^{-1} M_\odot$. We re-simulate the halos with higher resolution around each halo using the multi-resolution initial condition generator `grafic2` [20].

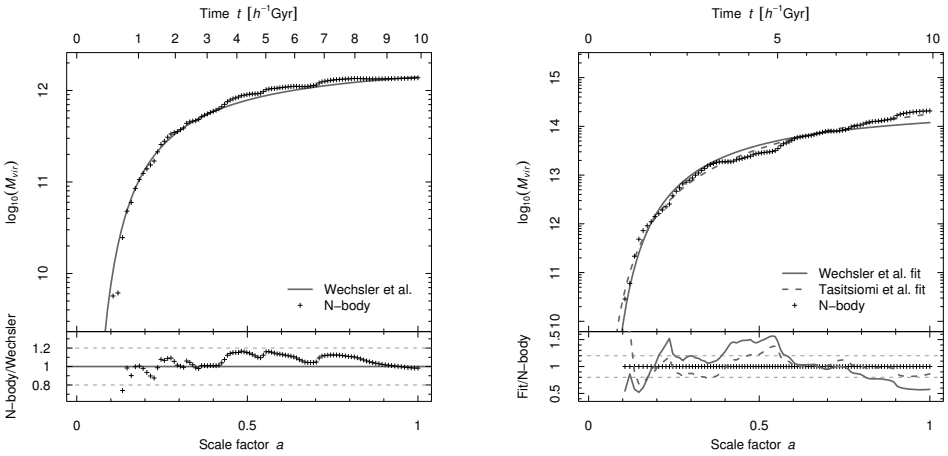

Figure 3.1: Mass accretion histories of the Milky-Way size halo (G1, *left*) and the galaxy-cluster sized halo (C1, *right*) in collisionless N-body simulations, fitted with the Wechsler et. al formula (Eq. 3.8).

We fit each mass accretion history with the Wechsler et al. mass accretion history (Fig. 3.1). We use the best-fitting parameters that have the least squares for the 101 data points, $\{a_i, \ln M_{\mathrm{vir},i}\}_{i=0}^{100}$, equally spaced in time between redshift $z = 10$ and 0: $(M_0, a_c) = (1.4 \times 10^{12} h^{-1} M_\odot, 0.29)$ for the Milky-Way sized halo (run G1), and $(1.2 \times 10^{14} h^{-1} M_\odot, 0.53)$ for the cluster sized halo (run C1), respectively. Because the Wechsler et al. formula is not a good fit for the cluster, the Tasitsiomi et al. [170] mass accretion formula

$$M(a) = M_0\, a^p\, \exp\left[-2a_c(a_0/a - 1)\right], \tag{3.9}$$

with parameters $M_0 = 1.2 \times 10^{14} M_\odot$, $a_c = 0.29$, $p = 1.54$ is also plotted in Fig. 3.1.

N-body simulations with Monte Carlo scatterings are performed with the multi-resolution initial conditions and with hard sphere cross sections $\sigma = 0.3, 1, 5$

and $15\,\mathrm{cm}^2\mathrm{g}^{-1}$ for the Milky-Way size halo, and $\sigma = 0.3$ and $1\,\mathrm{cm}^2\mathrm{g}^{-1}$ for the Cluster sized halo.

3.3 Results

We computed the time evolution of a conducting fluid model with various cross sections including zero (i.e., the fluid approximation for the purely collisionless limit). Left panel of Fig. 3.2 is the spherically averaged density profile for the collisionless N-body and the fluid approximation ($\sigma = 0$). The infalling fluid forms an accretion shock with discontinuities in fluid variables; numerically, this is handled by the artificial viscosity. The density profiles of two methods agree with other to within 20% down to a radius of 1% of the present shock radius, although there is a small but systematic trend that the fluid model gives steeper density profiles. For SIDM halos in the right panel of Fig. 3.2 (cross section $\sigma = 5\,\mathrm{cm}^2\mathrm{g}^{-1}$), however, the central density of the fluid model is about a factor of two larger than that of Monte Carlo N-body simulations at all redshifts. This is probably due to the slightly steeper density profile of the fluid model. Nevertheless, disagreement between the two method is found only for this overall constant, as we see in the following.

The time evolutions of the cosmological conducting fluid equations are plotted on the left panels of Figs. 3.3 and 3.4. The central density declines with time due to the SIDM heat conduction. For the Milky-Way sized halo (Fig 3.3), the central density at present decreases with cross section until it reaches minimum at some cross section between 10 and $15\,\mathrm{cm}^2\mathrm{g}^{-1}$; then, as cross section increases still further, the central density gets larger due to gravothermal collapse. The minimum

density of the fluid solution at present is $\rho_{\rm min}^{\rm fluid} \approx 8.6 \times 10^4 \rho_{\rm crit,0}$, where $\rho_{\rm crit,0}$ is the critical density at present. In the right panel of Fig 3.3, the same central densities of the fluid model divided by the minimum density $\rho_{\rm min}^{\rm fluid}$ are plotted together with the central densities in the N-body Monte Carlo simulations, divided by a different constant $\rho_{\rm min}^{\rm Nbody} \equiv 4.3 \times 10^4 \rho_{\rm crit,0}$; the graph illustrates that the N-body and the fluid model agree if the central densities are in units of their $\rho_{\rm min}$. The value of $\rho_{\rm min}^{\rm Nbody}$ is chosen for illustration purpose, but we think it is close to the minimum value in the N-body Monte Carlo simulations independent of the value of σ; in § 2.2.4, we showed that a SIDM halo initialized with a Navarro-Frenk-White (NFW) density profile relaxes to a cored profile with a central density $\rho_c \approx 2.0\rho_0$, where ρ_0 is a parameter appearing in the NFW profile (Eq. (2.9)); we fit the halo in the collisionless N-body simulations with the NFW profiles and plotted the values of ρ_0 as gray bars in the figures. Although the values of ρ_0 fluctuate due to halo mergers, the value $\rho_{\rm min}^{\rm Nbody}$ chosen above remains comparable to $2\rho_0$, despite these ρ_0 fluctuations, which suggests that this $\rho_{\rm min}^{\rm Nbody}$ value is indeed close to the minimum central density that the simulated SIDM halos can reach by the present.

In Fig. 3.4, we plot the same quantities for the galaxy-cluster sized halo. For the cluster scale, too, we see that the Monte Carlo N-body simulations agree with the conducting fluid model with constants $\rho_{\rm min}^{\rm Nbody} \equiv 1.1 \times 10^4 \rho_{\rm crit,0}$ and $\rho_{\rm min}^{\rm fluid} = 1.9 \times 10^4 \rho_{\rm crit,0}$ which has similar ratio to those for the Milky-Way size case. The difference between the Milky-Way scale and the cluster scale is that larger-mass haloes tend to form later due to the hierarchical nature of structure formation, which results in a longer "formation period" during which the NFW density ρ_0 decreases

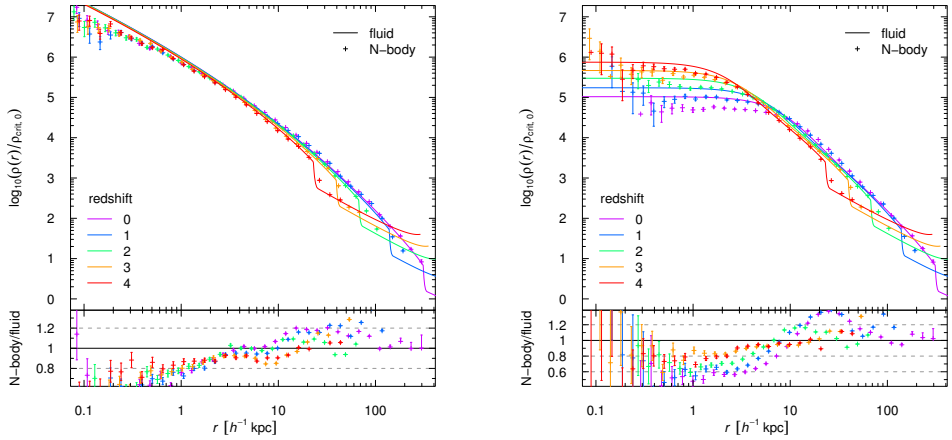

Figure 3.2: Spherically averaged density profiles of the Milky-Way sized (G1) collisionless (*left*) and self-interacting (*right*, $\sigma = 5\,\mathrm{cm}^2\mathrm{g}^{-1}$) CDM halos are compared between N-body simulations (points) and fluid computations (lines) at redshifts $z = 0, 1, 2, 3$ and 4. The vertical axis is the physical density in units of the current critical density, and the horizontal axis is the physical length (non-comoving). The density is calculated in uniform bins in $\log r$. The error bars are Poisson noise $\Delta\rho/\rho = 1/\sqrt{N_i}$, where N_i is the number of particles in ith bin. For the collisionless CDM (left) two methods agree within 20% down to 1% of the shock radius at $z = 0$. Gray bars are the ρ_0 parameter of the NFW profiles that fit the collisionless CDM profiles.

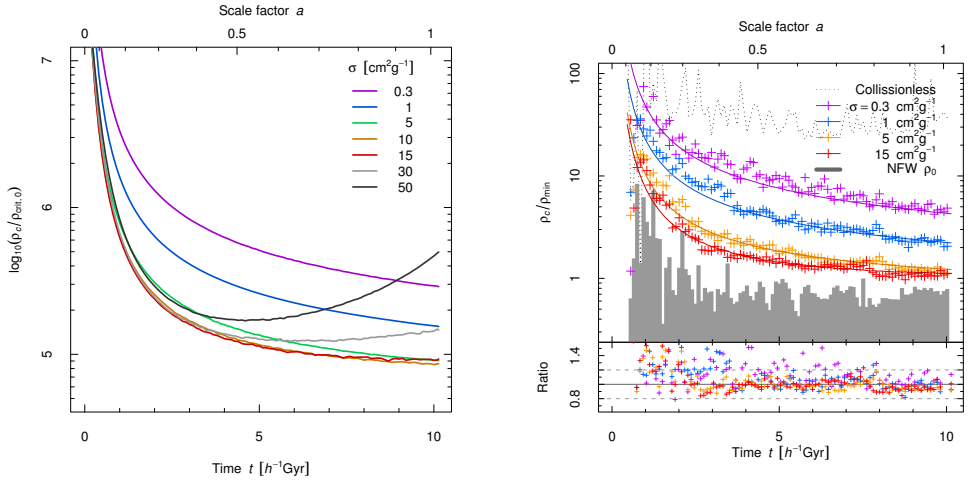

Figure 3.3: (*Left:*) Central density of a galaxy-mass SIDM halo as a function of time. (*Right:*) Comparison of conducting fluid model (solid lines) with Monte Carlo scattering simulation (points) for a galaxy-mass halo (G1) with cosmological mass assembly.

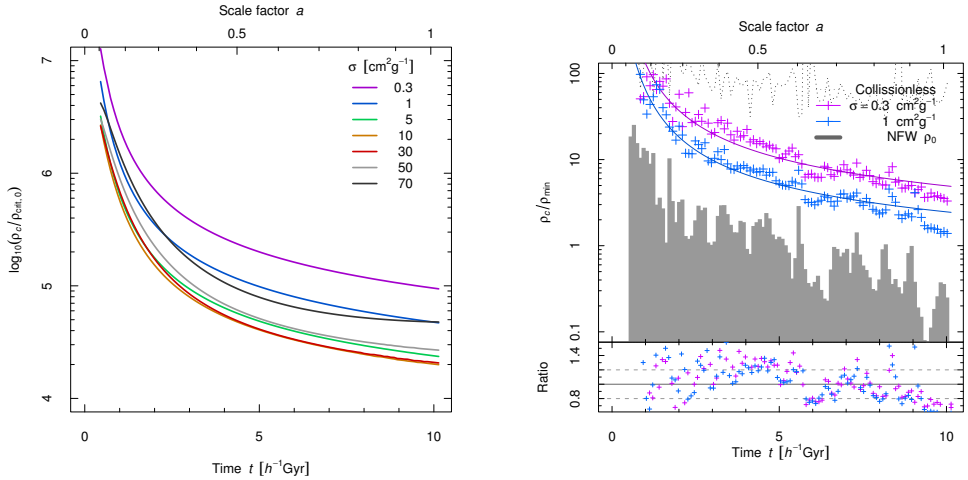

Figure 3.4: Same as Fig. 3.3 but for the cluster sized halo (run C1). Frequent mergers continues until present, which makes the NFW density ρ_0 decreasing.

with time; mass assembly history in the Milky-Way scale has a mixture of early formation period and an isolated period ($\rho_0 \approx const$), while that in the cluster scale is mainly still in the formation regime. The N-body and the fluid computations agree in both mass accretion regimes.

We showed that the fluid model and Monte Carlo basically agree with each other when there is a cosmological infall. For the galaxy sized halo $G1$, both methods give maximally flattened core for hard sphere cross section $\sigma = 5\,\mathrm{cm}^2\mathrm{g}^{-1}$. Previous disagreement on the value of the collision cross section required by N-body simulations and the fluid model to produce the maximally flattened profile was due to the departure from self-similarity of the mass accretion history in the simulations. The similarity solutions assume that mass infall continues at all epochs, which pumps energy into the core continuously by conduction, causing to grow in proportion to the total virial mass and radius. When the cosmological infall tapers off, however, this self-similar growth ends, and the thermal relaxation can proceed without the offsetting effect of further heating. As a result, a smaller cross section value σ serves to relax the non-self-similar halos after they become "isolated" than it would have for the self-similar halos.

Chapter 4

Monte Carlo N-body Simulations

In this chapter, we describe the algorithm and the numerical results of Monte Carlo N-body simulation for the self-gravitating SIDM with elastic collisions. The results were used in Chapter 3 to compare the N-body simulation with the conducting fluid model, and the results will be used in Chapter 5 to justify our semi-analytic relaxation model.

4.1 Models of Elastic Scattering Cross Sections

In the next few chapters, we consider cross sections with three types of velocity dependence: hard sphere cross section (velocity independent), Maxwell's model (cross section inversely proportional to the relative velocity) and that similar to Yukawa cross section. Here, we assume that the scattering angle is isotropic in the center-of-mass frame, for simplicity. See appendix A for the physical origins of those cross sections. In the following, we list the equations of velocity dependence used in our Monte Carlo scattering algorithm.

1. The *hard sphere cross section* (§A.2.1) is velocity independent and isotropic.
2. The next simplest form of cross section is a power law

$$\sigma = \sigma_0 (v/100 \text{ km s}^{-1})^{-\eta} \qquad (\eta \leq 1), \tag{4.1}$$

with an isotropic scattering angle. This is known as a Variable Hard Sphere (VHS) model in literature of molecular gas dynamics [24]. The name means that the angular distribution of the scattering is the same as the hard sphere (isotropic) but the radius of the sphere is "variable" or velocity dependent. The $\eta = 1$ cross section is called the *Maxwell model* (§ A.2.2). The power η must be less than 1, otherwise the collision rate diverge as $v \to 0$; large collision rate for small relative velocity is undesirable, as least in the simulation, because it would cause a large number of collisions at high redshifts between N-body particles separated at cosmological distances, and disturb the random Gaussian initial field. We do not want to disturb the successful large scale structure formation. we adopt the parameter $\eta = 1$, which makes the cross section decline steepest as the collision velocity increases, because observations of cluster of galaxies, which have large virial velocities (~ 1000 km s^{-1}), suggest that collisions are weak, if any, at those scales.

3. We call the cross section with the following velocity dependence as the *Yukawa-like cross section*

$$\sigma(v) = \frac{\sigma_0}{(1 + (v/v_c)^2)^2}. \tag{4.2}$$

Cross section of Yukawa interaction has a similar velocity dependence, but also has an angular dependence on the scattering angle (§ A.3.1), but we assume isotropic collision for simplicity. The free parameter v_c is related to the ratio of the intermediating boson mass m_ϕ to the dark matter particle mass $m_{\rm DM}$: $v_c = cm_\phi/m_{\rm DM}$, where c is the speed of light in vacuum.

4.2 Monte Carlo Scattering Algorithm

The Monte Carlo scattering algorithm that we have implemented in the N-body code GADGET 1.1 [164] is described in detail in this section. Our algorithm is similar to that in Kochanek & White [102]. Each particle can collide with one of its k nearest neighbors with a probability consistent with a given scattering cross section. For simplicity, we assume collisions are elastic and isotropic in the center of mass frame, but the Monte Carlo method can handle any differential cross section. We first outline the algorithm and then describe it step by step in more detail.

Consider N-body particles at positions $\mathbf{x}_j$ and velocities $\mathbf{v}_j$ with equal mass m. We discretize the distribution function f with,

$$f(\mathbf{x},\mathbf{v}) = \sum_j mW(\mathbf{x}-\mathbf{x}_j; r_j^{k\text{th}})\delta^3(\mathbf{v}-\mathbf{v}_j), \tag{4.3}$$

where $W(\mathbf{x},h)$ is a spline kernel function of size h, $r_j^{k\text{th}}$ is the distance from particle j to its $k \approx 32$nd nearest neighbor, and δ is the Dirac delta function. Our choice of kernel is often used in smoothed particle hydrodynamics, including GADGET. Our algorithm is identical to that of Kochanek & White if a top hat kernel is used for W instead of a spline. The result does not depend on the details of the kernel, however. We tested with $n = 128$ but did not see any difference.

The collision rate Γ that a particle at $\mathbf{x}$ with velocity $\mathbf{v}$ collide with this distribution f is,

$$\Gamma = \sum_j mW(\mathbf{x}-\mathbf{x}_j; r_j^{k\text{th}})\sigma|\mathbf{v}-\mathbf{v}_j|, \tag{4.4}$$

where σ is the scattering cross section per unit mass. Therefore the probability that an N-body particle 0 scatter with particle j during a small timestep Δt is,

$$P_{0j} = mW(\mathbf{x}_0 - \mathbf{x}_j; r_j^{k\text{th}})\sigma|\mathbf{v}_0 - \mathbf{v}_j|\Delta t \tag{4.5}$$

One can generate a random number and decide whether this collision happens and reorient velocities when they collide. This method is similar to a variant of direct simulation Monte Carlo called Nanbu's method [140]. His Monte Carlo algorithm, with the pairwise collision probability (Eq. 4.5), can be derived from Boltzmann equation as described in his paper. Conversely, results of Nanbu's numerical method converge, mathematically, to the solution of Boltzmann equation as the number of particles goes to infinity (Babovsky & Illner 12). In Nanbu's method only one particle is scattered per collision (only particle 0 but not j). The philosophy is that the N-body particles are samples chosen from real sets of microscopic particles, and those samples should scatter with the smooth underlining distribution function, not necessarily with another sampled N-body particle. However, then the energy and momentum is not conserved per collision. Even more, the expectation value of the energy decreases systematically [71]. In our case, the error in the energy rises by 10% quickly, so we decided to scatter N-body particles in pairs, not using Nanbu's method. Scattering in pairs is common in direct simulation Monte Carlo [24, e.g. Bird's method].

When particles are scattered in pairs, other particles j can scatter particle 0 during their timestep as well, but the scattering probability P_{0j}, in Equation 4.5, is similar to, but not exactly equal to P_{j0}, due to the difference in kernel size. Therefore

we symmetrize the scattering probability by taking the average scattering rate. Note that it is not trivial to generalize pairwise scattering algorithm to unequal mass simulations, because P_{0j} and P_{j0} would differ by a factor of their mass ratio, and there is no physical reason to symmetrize when two probabilities are intrinsically different.

In the following we describe our algorithm in detail. Each particle, say particle 0, go through the following steps, i to iii, during its time step Δt_0. Let particles $1 \ldots k$ be the k nearest neighbors of particle 0 ($k = 32 \pm 2$). The particle 0 collide with its neighbors with probabilities $P_{j0}/2$ (Eq. 4.5) during its timestep. The factor of two is the symmetrization factor that corrects the double counting of pairs. A particle j would scatter particle 0 during its timestep, which result in a symmetrized scattering rate. Imagine a probability space $[0,1]$, with disjoint subsets $I_j \equiv [\sum_{l=1}^{j-1} P_{l0}/2, \sum_{l=1}^{j} P_{l0}/2)$ that represent scattering events between particles 0 and j. We generate a uniform random number x in $[0,1]$, and scatter particles 0 and j if x falls in a segment I_j, as described below.

i) In the large Kn regime, most of the particles do not collide with other particle. Therefore we can reduce the computation by estimating the rough scattering probability first, and compute the accurate probability P_{0j} only if necessary. First we calculated an upper bound of the scattering probability,

$$\bar{P} = \tilde{\rho}\sigma v_{max}\Delta t_0, \tag{4.6}$$

where $\tilde{\rho}$ is the approximate density calculated from $r_0^{k\text{th}}$ via $\tilde{\rho} = km/\frac{4}{3}\pi(r_0^{k\text{th}})^3$, where v_{max} is the maximum speed of all the particles. If the generated random

number x is larger than $\bar{P}$, this means that x is not in any segment I_j, therefore the particle 0 do not collide during this timestep.

ii) If the possibility of collision was not rejected in step 1, we calculate the pairwise scattering probability P_{j0} and determine which neighbor the particle 0 collide with. The index j of collision partner is the smallest integer that satisfies $x \leq \sum_{l=1}^{j} P_{0j}$, i.e. $x \in I_j$, if such j exists (otherwise, the particle does not collide with any neighbors).

iii) For particle pairs that scatter, we reorient their velocities randomly, assuming an isotropic elastic scattering in the center of mass. Isotropic random directions can be generated by one square root operation, without using trigonometric functions, which is computationally more expensive [e.g., 179]. The velocities are updated in the 'kick' phase of the leap-frog time integration. At that time, we also update the center-of-mass velocities of the nodes around the scattered particles in the oct-tree, used for the gravity calculation. This is because the center-of-mass velocities can be changed drastically by scattering. We go up the Oct-tree from the scattered particle, recalculating the center-of-mass velocity of the node, until the node contains more then 1000 particles; the error is of order 0.1% and within machine precision if the node contains the pair of scattered particles.

We used the random number generator "Mersenne Twister" `MT19937` in the GNU scientific library [70], which has a period $2^{19937} - 1$, and equidistributes in 623 dimensions.

We allowed at most one scattering per time step per particle. In order to

suppress the error due to possible multiple scattering, we restrict the time step so that,

$$\bar{P} < 0.1. \tag{4.7}$$

This restriction make the Monte Carlo method computationally hard in small Kn regime because the timestep become much smaller than the dynamical time – the order of timestep in collisionless N-body simulations. This timestep problem may seem to be avoided by performing multiple scatterings per dynamical timestep, but there is another limit when the Knudsen number is small. The distance to kth neighbors must be smaller than the mean free path $\lambda = 1/(\rho\sigma)$,

$$r_k \lesssim \lambda. \tag{4.8}$$

Otherwise particles beyond mean free path are scattered and make the heat transfer larger than it should be in the diffusion limit. If one tries to avoid it by choosing a kernel size smaller than mean separation length, then the particles simply freely stream beyond the mean free path, which is again incorrect. The only way to overcome this problem is to increase the number of the particles in inverse proportion to the volume within the mean free path, $\propto \lambda^{-3} \propto \sigma^3$. Conditions (4.7) and (4.8) prevent us from running simulations with small mean free path.

4.3 Relaxation of an Isolated Halo

In order to understand the relaxational flattening of SIDM halos, we begin with the simplest case, an isolated halo. We simulate the evolution of an isolated NFW halo

with our Monte Carlo N-body simulation. This forms the basis of our semi-analytic model described later in Chapter 5.

We set the initial condition to be the NFW profile [142],

$$\rho(r) = \frac{\rho_0}{r/r_s(1+r/r_s)^2}, \tag{4.9}$$

with isotropic velocity distribution, as described in § 2.1.3. The particle velocity distribution function is calculated by the Eddington's formula [23, 99], and the random particle velocities are generated by the rejection method [1] with the distribution function. We truncate the profile at radius $r_{tr} = 10\,r_c$ and place a reflection boundary. The result in the core expansion phase is consistent with the $r_{tr} = 100\,r_s$ simulation in Chapter 2, but the central cusp is better resolved with smaller particle mass as a result of smaller truncation radius.

We run Monte Carlo N-body simulations with elastic scattering between N-body particles.

4.3.1 Relaxation Time

The results of the simulations with different velocity dependence on the cross section can be plotted independent of the cross section model with the relaxation time defined below.

We define a relaxation time t_r of an NFW SIDM halo (ρ_0, r_s), by the inverse of the mean collision rate, Γ, of particles that obey Maxwellian distribution with density ρ_0 and maximum one-dimensional velocity dispersion in the NFW profile,

$$v_{\rm max} = 0.30707 r_s \sqrt{4\pi G \rho_0}. \tag{4.10}$$

The velocity dispersion is derived by solved the hydrostatic equilibrium for the NFW profile with isotropic velocity dispersion. The relaxation time is

$$\Gamma = \iint d^3v_1 d^3v_2 \, f_0(\boldsymbol{v}_1) f_0(\boldsymbol{v}_2) \rho_0 \sigma |\boldsymbol{v}_1 - \boldsymbol{v}_2| \tag{4.11}$$

$$= a_* \rho_0 \sigma v_{\max} \quad (\text{evaluated at } v_{\max}), \tag{4.12}$$

$$t_r \equiv \Gamma^{-1} = (a_* \rho_0 \sigma v_{\max})^{-1}, \tag{4.13}$$

where $f_0(v)$ is the Maxwellian distribution,

$$f_0(v) = \frac{\rho_0}{(2\pi v_{\max}^2)^{3/2}} \exp\left[-\frac{v^2}{2v_{\max}^2}\right], \tag{4.14}$$

and the integration gives a cross-section dependent factor a_*,

$$a_* = a_h \equiv 4/\sqrt{\pi} \approx 2.2567 \quad (\text{hard sphere}), \tag{4.15}$$

$$a_* = a_M \equiv 1 \quad (\text{Maxwell model}), \tag{4.16}$$

$$a_* = a_Y(v_{\max}) \equiv \frac{2}{\sqrt{\pi}} \int_0^\infty \frac{\xi^3 e^{-\xi^3/2}}{1 + (\xi/\xi_c)} d\xi, \qquad \xi_c \equiv v_c/(\sqrt{2} v_{\max}) \tag{4.17}$$

(Yukawa-like cross section).

4.3.2 Time Evolution of the Central Density

Fig. 4.1 is the evolution of the central density ρ_c as a function of time in units of relaxation time $\tau = t/t_r$. The time evolution can be fitted by a universal fitting formula,

$$\rho_c(t)/\rho_0 = \mathcal{R}(\tau) \equiv \frac{A}{\sqrt{\tau + B\tau^2}} + C, \tag{4.18}$$

with $A = 7.57$, $B = 1.57$, and $C = 2.0$. The time dependence is independent of size of the halo or value of cross section, as long as the collision is in the large

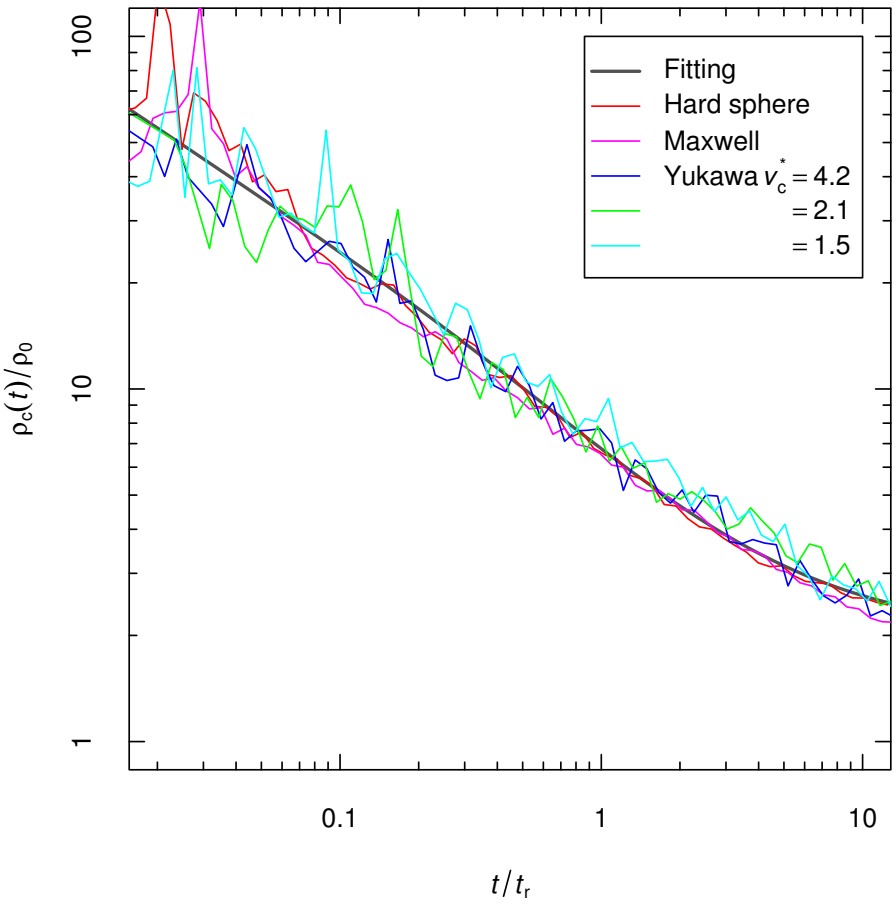

Figure 4.1: The central density of an isolated NFW profile against time in units of relaxation time (Eq. (4.11)), with the universal fitting formula – the *relaxation curve* $\mathcal{R}(\tau)$

Knudsen number regime; it is also independent on the velocity dependence in the range of cutoff velocity v_c we simulated. We use this fitting formula to model the evolution of cosmological SIDM halo in Chapter 5. The density profiles of this simulation will be discussed in § 4.5 together with those in cosmological SIDM simulations.

4.4 Cosmological SIDM Simulations

4.4.1 Simulation Setup

We run multi-resolution N-body simulations that zoom in to a single halo per simulation, with and without Monte Carlo scattering. We simulate three halos with different mass and merger histories.

We first run a cosmological simulation in a periodic box, $70h^{-1}$Mpc on a side with 256^3 particles. The cosmological parameters for this box is $\Omega_m = 0.25$, $\Omega_\Lambda = 0.75$, Hubble constant $h = 0.7$, with a random Gaussian fluctuation with index $n_s = 1$, amplitude $\sigma = 0.8$ and BBKS transfer function [15]. We use publicly available `grafic1`[1] package by E. Bertschinger to generate the initial condition at redshift $z = 70$. This redshift is chosen by the initial condition generator so that the initial density fluctuation (standard deviation of density contrast, $\delta \equiv (\rho - \bar{\rho})/\bar{\rho}$, where $\rho(\boldsymbol{x})$ is matter density and $\bar{\rho}$ is its cosmic mean) is smaller than 0.1 within the resolution of the simulation.

Then we find halos with friends-of-friends (FOF) algorithm [47] with a link-

[1] `http://web.mit.edu/edbert/`

ing length $\ell = 0.2$; Friend-of-friends algorithm defines that two particles i and j are friends ($i \sim j$) if their distance is smaller than ℓ times the mean separation distance$L/\sqrt[3]{N}$, and where L is the length of the simulation box and N is the number of particles, and extend the relation by a rule that a friend of a friend is also a friend ($i \sim j$ and $j \sim k \Rightarrow i \sim k$). This defines a equivalence relation between particles. A halo is defined by the equivalence class, or a group of friends. We then find the gravitational potential minimum for each FOF members and define it as the center of the halo. Then we find a radius r_{200c} that have mean density 200 times the critical density; the symbol "c" stress that the overdensity is measured with respect to the critical density, not the mean matter density).

We pick arbitrary three halos, which we describe below, at redshift $z = 0$ and find a cubic region in the initial condition such that it contains all the particles within $3r_{200}$ [77]. We add high frequency modes in this region and generate initial condition with smaller-mass particles using the `grafic2` package ([20]). `grafic2` has a known bug that it uses the power spectrum of baryon for cold dark matter if it reads the power spectrum data from file [166], but our simulation uses the analytical fitting formula by BBKS. Since we use this simulation to compare with conducting fluid model, or semi-analytic relaxation model, our conclusions are not sensitive to the power spectrum we use. Outside this high resolution region, there are additional two or three layers with less resolution, keeping roughly the same angular resolution from the halo location [174].

We re-simulate this multi-resolution initial condition with our N-body code with Monte Carlo scattering. Particles with different masses do not collide with

each other in our code, because our pairwise scattering algorithm cannot be consistent with a single value cross section per unit mass. Because there is only one particle mass in the halo we analyze, scattering between different resolution particles is unimportant in our simulations. (Multi-mass collisional system may have significantly different properties, for example, mass segregation [e.g., 100].)

First simulation, which we call $G1$, focus on a Milky-Way sized halo with viral mass $M_{\rm vir} = 1.38h^{-1}M_{\odot}$ at $z = 0$, which have no major mergers. (Virial mass and radius are defined in § 3.1.2.) There are two 1:8 major merger before $z = 2$, but there are no other mergers with ratio 1:10 or higher in the simulation. The halo is almost isolated with no evolution in the NFW parameters $\{\rho_0, r_s\}$ since $z \sim 2$. The high resolution region is $6.56h^{-1}$kpc on a side and have 144^3 particles. The particle mass is $6.57 \times 10^6 h^{-1}M_{\odot}$, which means there are 2.11×10^5 particles within the virial radius $r_{\rm vir}$. The softening length for the gravitational calculation is set to $\epsilon = 0.7h^{-1}$kpc.

Second galaxy-sized halo, "$G2$," has a major merger; virial mass doubles from $2 \times 10^{11}h^{-1}M_{\odot}$ to $4 \times 10^{11}h^{-1}M_{\odot}$. during redshifts $z = 0.75 - 0.53$. We see what happens to a SIDM halo with a major merger. Third halo, "$C1$," has a scale of galaxy cluster with mass $2.1 \times 10^{14}h^{-1}M_{\odot}$. This is the second largest halo in the simulation box. This halo continues to grow during the entire age of the universe, which is a typical behaviour for cluster scales in standard ΛCDM universe. The choice of multi-resolution initial condition is summarized in Table 4.1.

We showed the projected 2D density map of simulations $G1$ and $G2$ in Fig. 4.2 in cases of collisionless (top panels), hard sphere cross section $\sigma = 1$

name	Layer 1		Layer 2		Layer 3		Layer 4	
	L	factor	L	factor	L	factor	L	factor
G1	24	6	48	3	128	1	256	1/2
G2	12	12	24	6	64	1	256	1/2
C0	88	2	256	1	-	-	-	-

Table 4.1: Our setup of multi-resolution initial condition. We zoom in to two galaxy scale halo $G1$ and $G2$ and one cluster scale halo $C1$. L is the length of the refined region in the coarse mesh unit; $L = 256$ corresponds to the length of the full periodic box. "factor" is the refinement factor per dimension. Mass of N-body particles are factor^3 times smaller than those in the coarse 256^3-particle simulation.

(middle) and $\sigma = 5\,\mathrm{cm}^2\mathrm{g}$ (bottom). Left three panels are the Milky-Way sized halo $G1$ and right three panels are intermediate mass galaxy $G2$. All figures are at redshift $z = 0$.

4.5 Partially Relaxed Density Profiles

4.5.1 Cored NFW Formula

In Fig. 4.3, we plot the spherically averaged density profiles for the halos in isolated and cosmological Monte Carlo N-body profiles. We introduce an empirical density profile formula, "cored NFW profile" with three parameters,

$$\rho(r) = \frac{\rho_0}{\sqrt{(r_c/r_s)^2 + (r/r_s)^2}\,(1 + r/r_s)^2}. \tag{4.19}$$

The profile reduces to the NFW profile for $r_c = 0$; the additional parameter r_c represents the amount of collisional relaxation. Fig. 4.3 shows that the cored NFW profile fits well for $\rho_c/\rho_0 \gtrsim 5$. For profiles with smaller central density, the non-singular isothermal sphere represents the profile better.

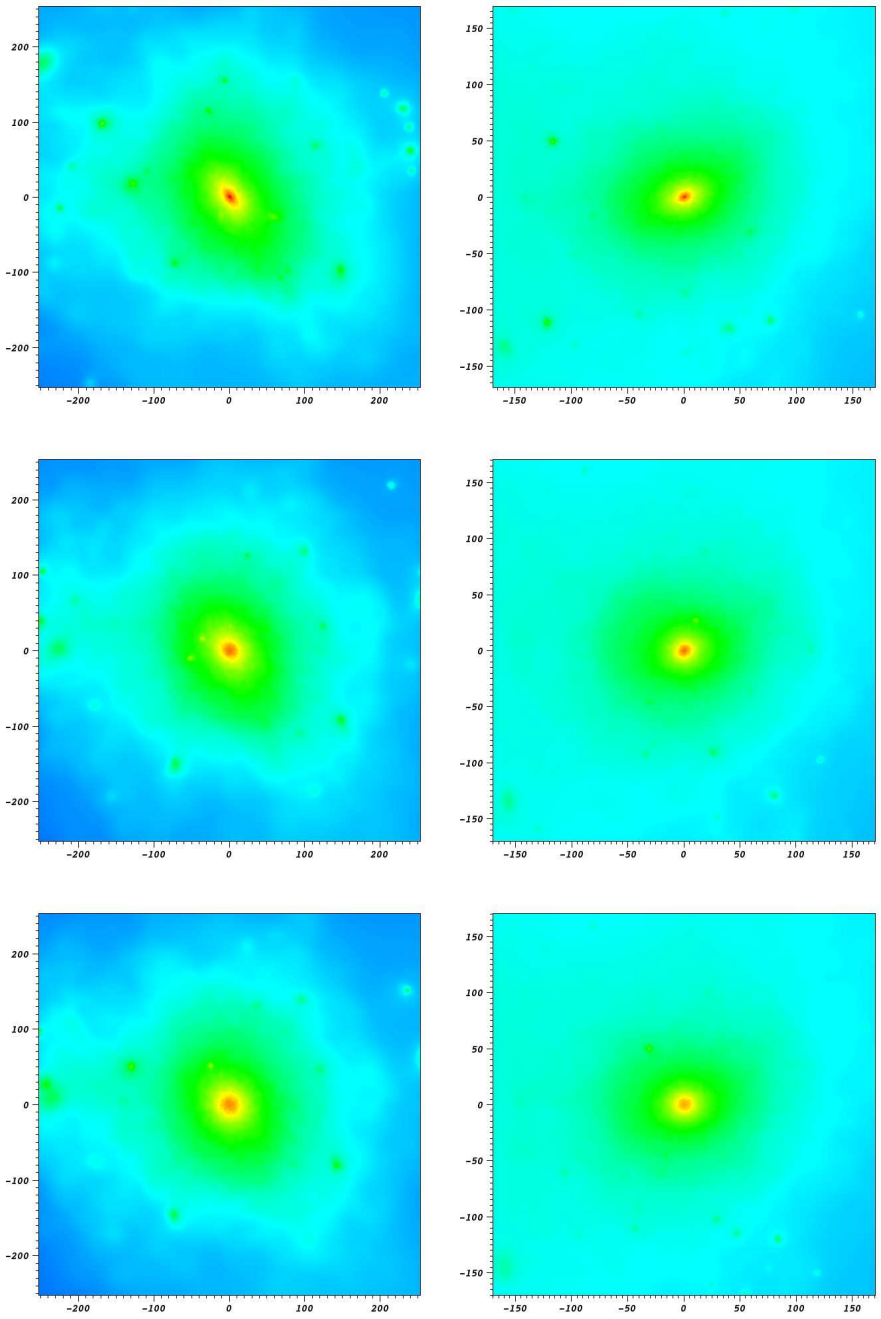

Figure 4.2: Projected density map of Monte Carlo N-body simulation at $z = 0$ for cross section values $\sigma = 0, 1$ and $5\,\mathrm{cm}^2\mathrm{g}^{-1}$ from top to bottom, for our simulated halos G1 (*left*) and G2 (*right*).

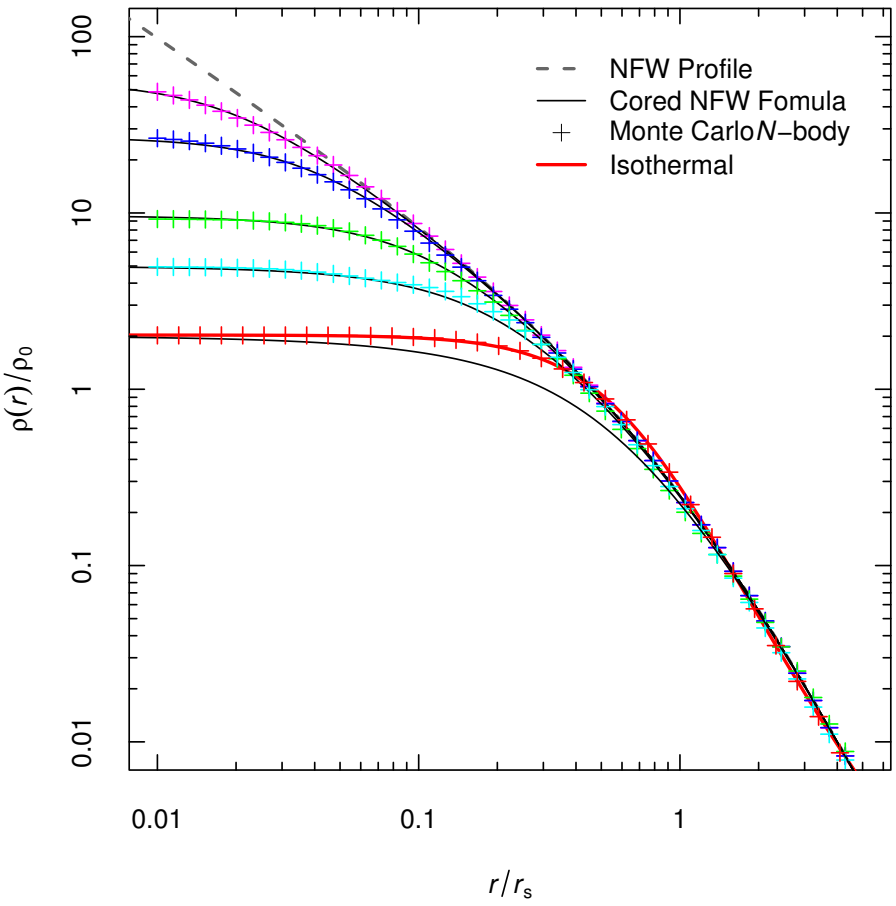

Figure 4.3: The density profiles of partially and fully relaxed SIDM halos (isolated) in our Monte Carlo N-body simulations initialized by the NFW profile. The partially relaxed profiles ($\rho_c/\rho_0 \gtrsim 5$) can be fitted by our empirical formula "cored NFW profile."

SIDM halo when it has minimum central density has an non-singular isothermal profile around the core, which is the solution of hydrostatic equilibrium with constant temperature and finite central density ρ_c. Non-singular isothermal profile plotted in Fig. 4.3 has parameters

$$\rho_c = 2.05\rho_0, \qquad r_c = 0.205 r_s, \tag{4.20}$$

where the core radius is $r_c \equiv \sqrt{v_c^2/(4\pi G\rho_c)}$ related to the (constant) one-dimensional velocity dispersion v_c.

This maximally flattened profile is similar to the Truncated Isothermal Sphere (TIS), which is the minimum energy solution of virial and hydrostatic equilibrium with a finite boundary pressure [8]. The TIS model is an analytical approximation for CDM halos which shares some of the important features of the halos found in N-body simulations of CDM. This TIS, resulting from spherical collapse, is a non-singular isothermal sphere (i.e. solution of the isothermal Lane-Emden equation) with parameters,

$$\rho_c^{\rm TIS} = 1.80 \times 10^4 \rho_{\rm crit}, \qquad r_c^{\rm TIS} = r_{\rm vir}/26.5. \tag{4.21}$$

in a flat matter dominated universe[2] at the time of collapse, where $r_{\rm vir}$ here refers to the radius of the sphere enclosing a mean density of $18\pi^2\rho_{\rm crit}$. The truncation radius of TIS is at radius $29.4 r_c$. This central density is equal to that of the maximally flattened NFW profile after SIDM relaxation if and only if the initial NFW profile

[2]See [90] for open or ΛCDM cosmology. Our main interest is in dwarf galaxy scales which collapse in matter dominated era.

has a concentration parameter,

$$c_{\rm vir} \equiv r_{\rm vir}/r_s = 5.31. \tag{4.22}$$

The core radius of the flattened NFW profile with this concentration,

$$r_c = 0.205 r_s = r_{\rm vir}/25.9, \tag{4.23}$$

is consistent with the core radius for the TIS, $r_c^{\rm TIS}$, which means that the maximally flattened NFW profile is close to the TIS out to $r_{\rm vir}$. We compare this concentration parameter with the Bullock et al. [34] model of halo NFW profile concentration parameter, $c_{\rm vir}$, which successfully explains the mean concentration of NFW halos in galaxy scales, observed in N-body results. In the model, the concentration parameter for mass $M_{\rm vir}$ is

$$c_{\rm vir} = K(FM_{\rm vir}/M_*)^{-\alpha}, \tag{4.24}$$

where $K \approx 4.0$ and $F \approx 0.01$ are the two free parameters of the model; M_* is the mass scale for which the filtered linearly extrapolated density contrast δ has a rms fluctuation σ_M equal to the critical value δ_c (the time at which $\delta = \delta_{\rm crit}$ in the linear perturbation solution is the time when the nonlinear solution for a spherical top-hat perturbation collapses to infinite density; $\delta_c = 1.68$ for Einstein-de-Sitter), and α is the logarithmic slope of the linear density fluctuation $\alpha = -d\ln\sigma_M/d\ln M$. The factor α depends on mass and cosmological parameters weakly; $\alpha \approx 0.13$ in [34]. Later simulation results revise the values $K = 3.4$, $\alpha \approx 0.094$ for WMAP5 cosmological parameters [122]. With the latter set of parameters, halos that just collapsed, i.e. $M = M_*$ by definition, have concentration parameter $c_{\rm vir} = 5.24$.

This is surprisingly close to our TIS value matched above (Eq. 4.22); Maximally flattened SIDM halos can be, therefore, thought of as TIS halos.

4.5.2 Rotation Curves

Observations of rotation curves of galaxies often assumes a pseudo-isothermal profile for dark matter density:

$$\rho(r) = \frac{\rho_c^{\rm iso}}{1 + (r/r_{\rm iso})^2}, \tag{4.25}$$

which has two parameters, central density $\rho_c^{\rm iso}$ and core radius $r_{\rm iso}$. The circular velocity of the pseudo-isothermal profile can be calculated analytically

$$V_c(r) \equiv \sqrt{GM(r)/r} = r_{\rm iso}\sqrt{4\pi G\rho_c^{\rm iso}}\,[1 - \arctan(x)/x] \tag{4.26}$$

where $M(r)$ is a mass enclosed within a sphere with radius r. The circular velocity increases monotonically with radius, and asymptotes to a value $V_{\rm max}^{\rm iso} \equiv r_c^{\rm iso}\sqrt{4\pi G\rho_c^{\rm iso}}$

In order to relate the SIDM halos to the rotation curve of pseudo-isothermal profile, we assume that the central density ρ_c of an SIDM halo is the same as the central density parameter $\rho_c^{\rm iso}$, and the maximum circular velocity of the NFW profile,

$$V_{\rm max}^{\rm NFW} = 0.46759 r_s\sqrt{4\pi G r_s} \tag{4.27}$$

is equal to $V_{\rm max}^{\rm iso}$. Then there is a simple relation between the central density of partially relaxed SIDM halo and NFW parameters

$$r_{\rm iso} = 0.46759\sqrt{\rho_s/\rho_c} \tag{4.28}$$

Rotation curves computed from the isolated halos in Monte Carlo N-body simulation with hard sphere scattering (§ 4.3.2) is plotted in Fig 4.4. The figure also shows that the pseudo-isothermal rotation curves with $r_{\rm iso}$ calculated from the formula above, which fits rotation curves of partially relaxed N-body halos well for sufficiently flattened profiles, $\rho_c/\rho_0 \lesssim 7$. The figure also shows the best-fit pseudo-isothermal rotation curve that fits the N-body data. For less relaxed halos $\rho_c/\rho_0 \gtrsim 10$, the equation for $r_{\rm iso}$ (4.28) do not give the best fit, which indicates that the central density estimate based on a pseudo-isothermal fit against a rotation curve does not exactly gives the actual central density of the SIDM halo; therefore needed to be interpreted carefully. We use pseudo-isothermal rotation curves with Eq. (4.28) to compare central densities of SIDM halos with observed rotation curves.

In Fig 4.5 we plot the rotation curve of our simulated Milky-Way sized halo $G1$ at redshift 0 in our cosmological Monte Carlo simulations, for different values of cross sections. The rotation curves are fitted by the pseudo-isothermal sphere and the Burkert profile [36],

$$\rho(r) = \frac{\rho_0}{(1+(r/r_b)^2)(1+r/r_b)} \tag{4.29}$$

For highly flattened profile ($\rho_c \lesssim 3\rho_0$), Burkert profile fits the rotation curve better; this is consistent with the fact that SIDM collisions drive halo toward Truncated Isothermal Sphere (TIS), and TIS is fitted by the Burkert profile very well [89]. For less relaxed halos ($\rho_c \gtrsim 5\rho_0$) pseudo-isothermal profile fits better than Burkert profile.

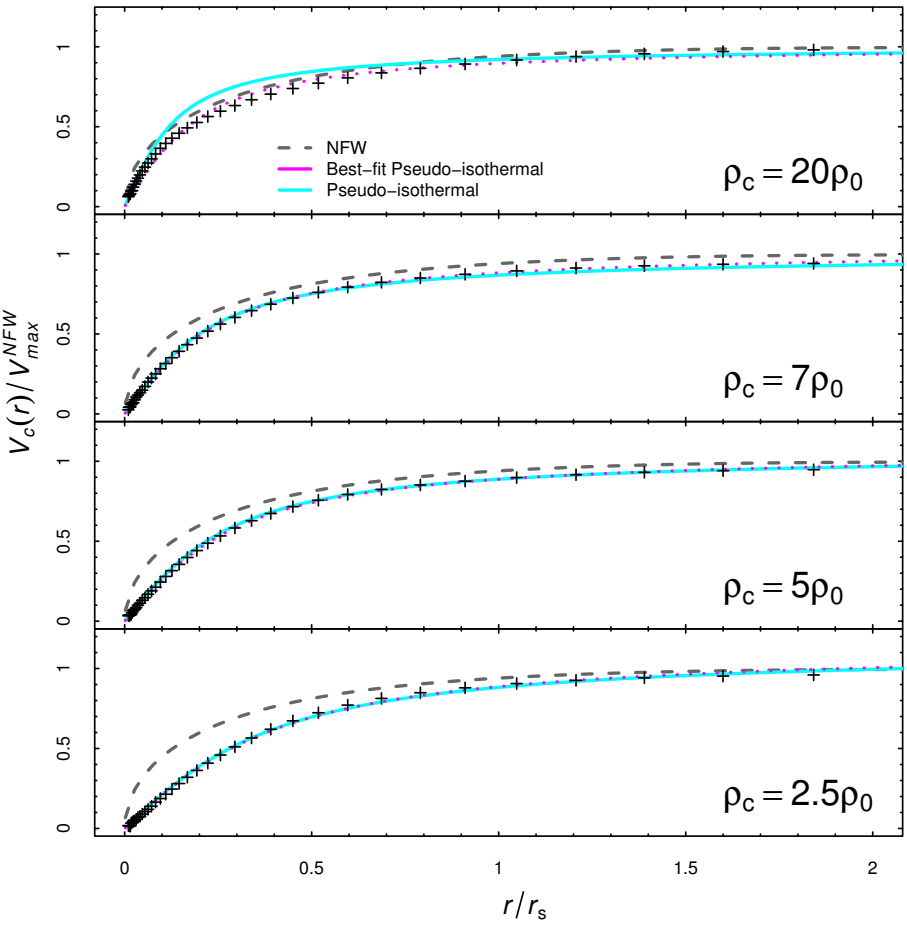

Figure 4.4: Rotation curves of the isolated SIDM halo in Monte Carlo N-body simulations. Crosses are the data from the simulation, and the solid line shows a pseudo-isothermal rotation curve with the core radii given by Eq. (4.28) and the central density of SIDM halos. When the SIDM halo is sufficiently relaxed ($\rho_c/\rho_0 \lesssim 7$), the rotation curve can be fitted with the Pseudo-isothermal profile with Eq. (4.28). Dotted lines are the best-fit pseudo-isothermal rotation curves against simulation results.

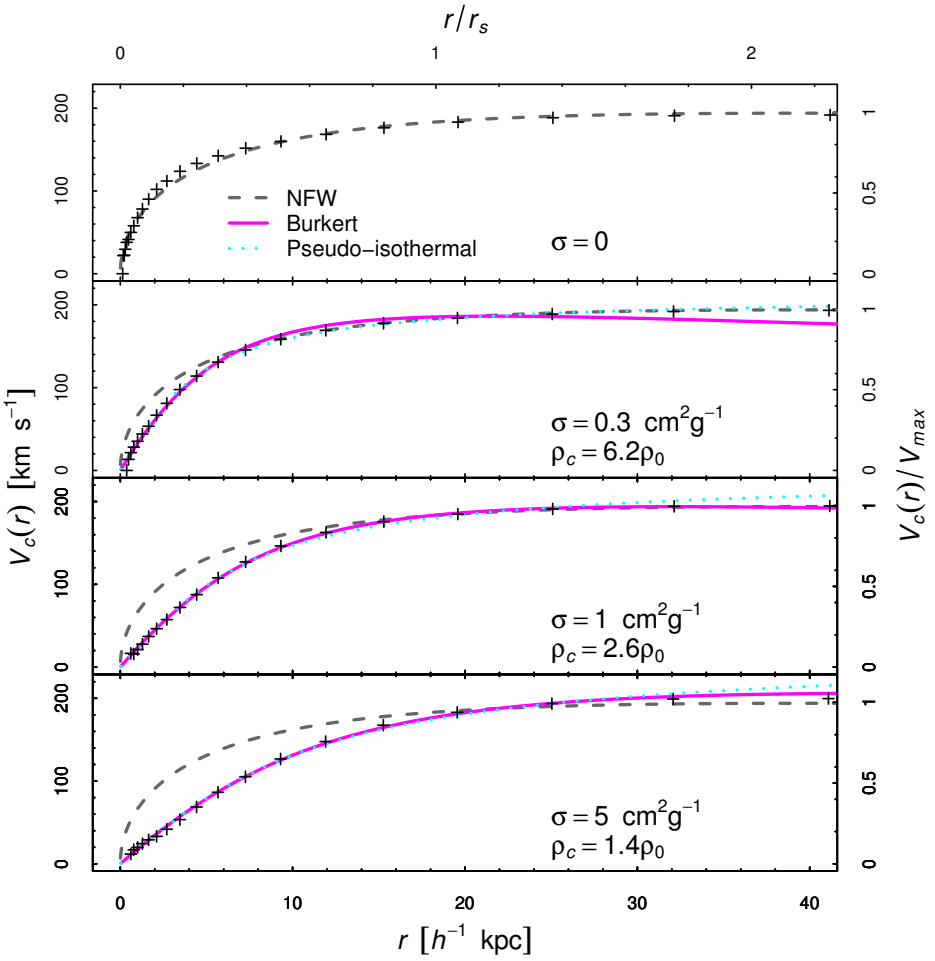

Figure 4.5: Rotation Curves of a cosmological SIDM halo (§ 4.4, *G*1) at present for different values of cross sections, and fits to the rotation curves by pseudo-isothermal profile (dotted) and Burkert profile(solid). Dashed lines are the rotation curve of NFW fit to the collisionless simulation. For highly flattened profile ($\rho_c \lesssim 3\rho_0$), Burkert profile gives a better fit. For less relaxed halos ($\rho_c \gtrsim 5\rho_0$) pseudo-isothermal profile fits better than Burkert profile.

Chapter 5

Semianalytic Relaxation Model

The collisions between SIDM particles convert a SIDM halo toward a relaxed halo with a non-singular cored density profile, which is known to be singular for collisionless CDM. The aim of this chapter is to understand, quantitatively, how the density profile of a SIDM halo evolve in ΛCDM cosmology. We have developed a semi-analytic SIDM relaxation model that describes the relaxational flattening, under the condition that its evolution without the self interaction (i.e., the evolution in the conventional Λ-collisionless-CDM cosmology) is known. We will show that the additional collisional effect of SIDM on any CDM halos are solely characterized by a single function, the *relaxation curve*, $\mathcal{R}(\tau)$ (Eq. 5.2).

The practical benefit of this model is that we can predict the ensemble of density profiles of SIDM halos without running computationally expensive Monte Carlo N-body simulations. For example, in Chapter 6, we will show a statistical distribution of SIDM halos in galaxy-cluster scale in a periodic box of $420h^{-1}$Mpc on a side, using our semi-analytic model. If we only used the Monte Carlo N-body simulations to find the range of cross sections consistent with galaxy-cluster observations, we would need to resolve down to the scale observationally resolved ($\sim\ 10h^{-1}$kpc) with the numerical simulation only, which would require more than

4200^3 particles (assuming that the profile is resolved down to 1% of the initial mean particle separation, which is probably too optimistic); this is about a number of current state-of-art simulations. It is very difficult to simulate such large simulations for each combination of parameters in the scattering cross section. With our semi-analytic model, we only need to run one lower-resolution N-body simulation per mass scale we are interested in, followed by computationally trivial post processing for various models and values of cross sections.

We describe our model in § 5.1, show how we solve the model numerically in § 5.2, justify the model by comparing with Monte Carlo N-body simulations with cosmological initial conditions in § 5.3, and discuss analytical properties of the model in § 5.4. This model will be applied to a statistical ensemble of cosmological CDM halos in the next chapter (Chapter 6), and compared with observations of dwarf/LSB-galaxy rotation curves and a density profiles of a cluster of galaxies.

5.1 The Model: Flattening in ΛCDM

Unlike the isolated halo in § 4.3, for which the relaxation of NFW profiles with any size, mass and cross section, is characterized by a single curve,[1] cosmological halos evolve differently from halo to halo as a result of different merger and accretion histories. We present a semi-analytic model that reproduces the evolution of cosmological SIDM haloes; we assume that cosmological CDM halos without

[1] In the large Knudsen number regime, which is of our interest for astrophysical applications

collision have NFW profiles (Navarro, Frenk, & White [142]),

$$\rho(r) = \frac{\rho_0}{(r/r_s)(1+r/r_s)^2}, \tag{5.1}$$

which is known to fit the spherical averaged density profiles well in collisionless CDM simulations, on length scales of our interest — few percent of the virial radius or larger (Chapter 6). For a given history of NFW profile parameters $\{\rho_0(t), r_s(t)\}$, we are able to calculate the time dependence of the central density $\rho_c(t)$ by solving an ordinary differential equation of the model. The question of how collisionless CDM halos, $\{\rho_0(t), r_s(t)\}$, grow in a ΛCDM cosmology, theoretically, is beyond our scope; we extract those parameters from cosmological collisionless N-body simulations, as numerical data. Our focus in this chapter is the collisional relaxation effect toward a cored density profile on top of a given CDM halo in the conventional ΛCDM.

The key information in our model is the relaxation curve $\mathcal{R}(\tau)$

$$\rho_c(t)/\rho_0 = \mathcal{R}(\tau) \equiv \frac{\mathcal{A}}{\sqrt{\tau + \mathcal{B}\tau^2}} + \mathcal{C}, \qquad (t > 0). \tag{5.2}$$

As shown in § 4.3, it is an empirical fitting formula for the central density ρ_c, as a function of dimensionless time in the unit of halo relaxation time $\tau = t/t_r$, for numerically simulated SIDM halos in isolation, which is initially an NFW profile; the fit gives constants $\mathcal{A} = 7.57$, $\mathcal{B} = 1.57$, and $\mathcal{C} = 2.0$. The relaxation time is defined to be completely determined by the two NFW parameters $\{\rho_0, r_s\}$ for a given cross section model. The density ρ_0 and the relaxation time t_r are both constants in the isolated halo simulations. The ratio of the central density to the NFW

density ρ_0 start with infinity at $\tau = 0$ and converges to $\mathcal{C}$ as $\tau \to \infty$. To generalized this formula to cosmological halos, whose ρ_0 and t_r evolve with time, we first note that the relaxation curve is, trivially, a solution of an ordinary differential equation (ODE)

$$\frac{1}{\rho_0}\frac{d\rho_c(t)}{dt} = -\frac{1}{t_r}\mathcal{F}(\rho_c(t)/\rho_0) \tag{5.3}$$

where $\mathcal{F} \equiv -\mathcal{R}' \circ \mathcal{R}^{-1}$; $\mathcal{R}' = d\mathcal{R}/d\tau$ is a derivative, $\mathcal{R}^{-1}$ is the inverse function of $\mathcal{R}$, and $\mathcal{R}' \circ \mathcal{R}^{-1}(x) \equiv \mathcal{R}'(\mathcal{R}^{-1}(x))$ is the composite function of aforementioned two functions. The inverse function can be calculated easily by solving a quadratic equation,

$$\tau = \mathcal{R}^{-1}(\Delta) = \frac{1}{2B}\left\{\sqrt{1 + 4B\left[\mathcal{A}/(\Delta - \mathcal{C})\right]^2 - 1}\right\}, \quad \Delta = \rho_c/\rho_0 > \mathcal{C}. \tag{5.4}$$

The function $\mathcal{F}$ is, therefore, also an elementary function. Then, it is mathematically natural to generalize this ODE to that with explicit dependence on time, through given time evolutions of halo parameters $\{\rho_0(t), r_s(t)\}$

$$\frac{1}{\rho_0(t)}\frac{d\rho_c(t)}{dt} = -\frac{1}{t_r(t)}\mathcal{F}(\rho_c(t)/\rho_0(t)). \tag{5.5}$$

This is our *semi-analytic relaxation model*. The assumption is that a cosmological halo relaxes as if it is an isolated halo, except for the indirect dependence on time through the halo parameters $\{\rho_0(t), r_s(t)\}$, which determine the outer shape of the SIDM halo. The physical picture here is that a halo relaxes primarily by virialized SIDM particles inside the halo, which are similar to those in isolated NFW halo, and particles or substructures that just fall into the halo are not significantly different from virialized particles. We show that this model agrees reasonably well with Monte Carlo scattering N-body simulations in § 5.3.

5.2 Numerical Method of Solving the Model

We present how we obtain NFW halo parameters, $\{\rho_0, r_s\}$, from a snapshot of collisionless N-body simulations, and how we solve the model with those discrete sets of halo parameters, numerically.

From a set of N-body particle positions, we find halos using friends-of-friends algorithm with a linking parameter $\ell = 0.2$, and find the center of each halo, which we define as the point of minimum gravitational potential (see Chapter 4 for details of those steps). We then use a rather simple method to find the halo parameters, assuming a following facts of the NFW profile apply to CDM halos: The circular velocity of an NFW profile, $V_c(r) = \sqrt{GM(r)/r}$ at scale radius r_s is related to the maximum circular velocity $V_c^{\max}$ by,

$$V_c(r_s) = 0.9451 V_c^{\max}; \tag{5.6}$$

The mass enclosed by a sphere of radius r is,

$$M(r) = 4\pi\rho_0 r_s^3 \left[\frac{r/r_s}{1 + r/r_s} + \ln(1 + r/r_s) \right]. \tag{5.7}$$

We first find the maximum circular velocity $V_c^{\max}$ among the halo particles (particles in friends-of-friends equivalent class), and set the scale radius r_s to be the smallest particle radius that satisfies $V_c(r) \geq 0.9451 V_c^{\max}$. With that r_s, the density ρ_0 is set by the relation (5.7) at $r = r_s$: $M(r_s) = 4\pi\rho_0 r_s^3 (\ln 2 + 1/2)$. The maximum likelihood method for fitting may give a better result [122], but the results of our method are consistent with known results on the relation between the scale radius and the halo mass.

We solve our semi-analytic model numerically, with a discrete set of NFW parameters, $\{\rho_c^i, r_s^i\}$, at discrete times, $\{t^i\}$ ($i = 0, 1, 2 \ldots$), which we calculate with a collisionless N-body simulation, as shown below.

1. The initial central density is set to infinity, $\rho_c^0 = \infty$.

2. Assuming that the ODE was solved up to time step i, the NFW parameters during the next time step are averages of this and the next time step: $\rho_0^{i+1/2} \equiv (\rho_0^i + \rho_0^{i+1})/2$, $r_s^{1+1/2} \equiv (r_s^i + r_s^{i+1})/2$. The relaxation during the time is calculated with those parameters $t_r^{i+1/2} \equiv t_r(\rho_0^{i+1/2}, r_s^{i+1/2})$.

3. A dimensionless time parameter τ is set to $\tau = \mathcal{R}^{-1}(\rho_c^i/\rho_0^{i+1/2})$ if $\rho_c/\rho_0^{i+1/2} > \mathcal{C}$, for which the inverse function $\mathcal{R}^{-1}$ is defined. Because ρ_0 is usually a nonincresing function of time, the condition on the ratio is usually satisfied, but sometimes during mergers when NFW fit is not good, or due to other numerical fluctuations, $\rho_c/\rho_0^{1+1/2}$ may be smaller than $\mathcal{C}$. In such case, we simply set $\rho_c^{i+1} = \rho_c^i$, because the halo cannot relax any further.

4. In the case of $\rho_c/\rho_0^{i+1/2} > \mathcal{C}$, the central density at the next time step is evolved to, $\rho_c^{i+1} = \rho_0^{i+1/2}\mathcal{R}(\tau + (t^{i+1} - t^i)/t_r^{i+1/2})$, which is a relaxation along the relaxation curve for the isolated NFW profile.

This is our method of solving the time evolution of a given NFW halo history at discrete times.

5.3 Verification of the Model

We show that our semi-analytic model for relaxation of SIDM halos (Eq. 5.5) agree with cosmological SIDM simulations with Monte Carlo scattering, presented in § 4.4. Figures 5.1-5.3 show that the model agree with Monte Carlo scattering simulations from galaxy scale to cluster scale for all cross section models presented in § 4.1.

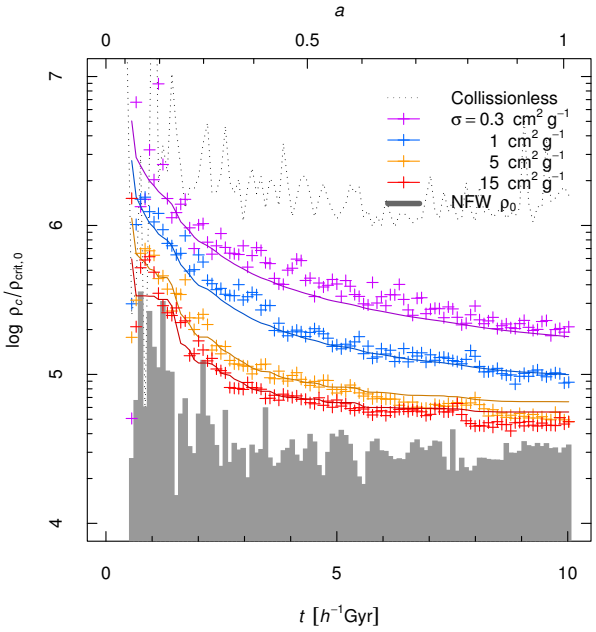

Figure 5.1: Comparison of our semi-analytic relaxation model with Monte Carlo N-body simulations with hard sphere scattering cross section for $\sigma = 0.3, 1, 5$ and $15\,\mathrm{cm}^2\mathrm{g}^{-1}$ from top to bottom. The dotted line is the "central density" for the collisionless simulation, which indicates the resolution limit for the central density; the central density of collisionless CDM halos continue to increases toward the center, without any know limit. Gray bars are the density parameter ρ_0 in the NFW formula.

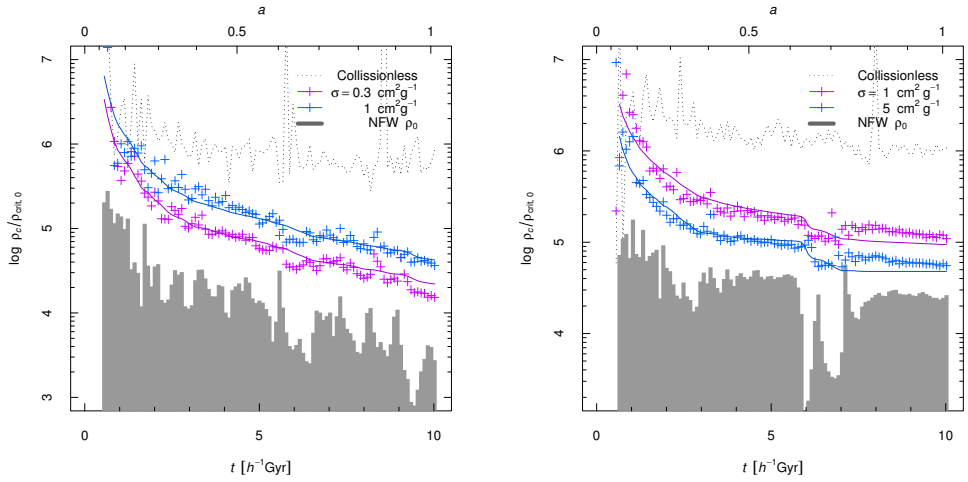

Figure 5.2: Same as Fig. 5.1 but for halo masses of intermediate galaxy with major merger (*left*, G2) and clusters of galaxies (*right*, C1). Semi-analytic model agree with Monte Carlo N-body simulations for both cases. The model works reasonably well for cases with a major merger and continuous mass growth.

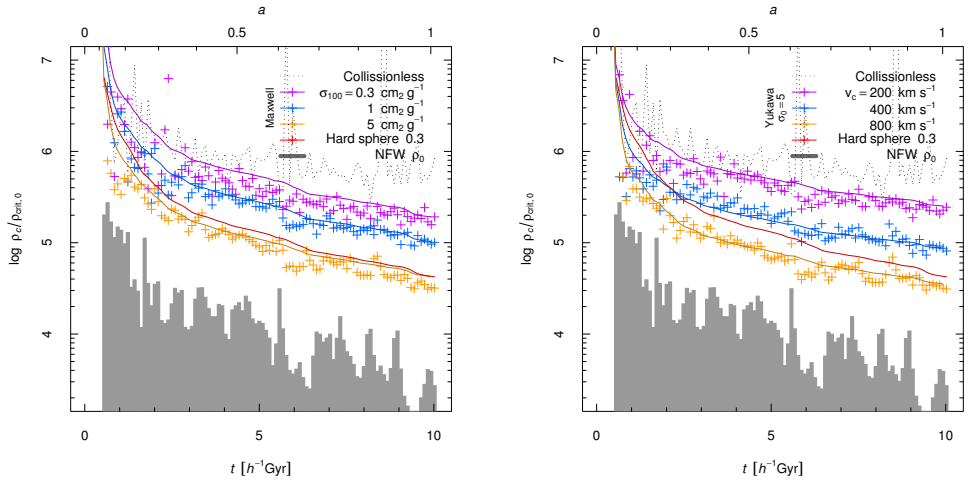

Figure 5.3: Same as Fig. 5.1 but with Maxwell cross sections (*left*) and Yukawa-like cross sections (*right*) for the cluster mass halo (C1). The Semi-analytic model works well for those velocity dependent cross sections as well.

5.4 Analytical Properties

5.4.1 Self-Similar Solution

We present the self-similar solution of the semi-analytic relaxation model; the solution assumes that the halo density parameter evolves as,

$$\rho_0 \propto a^{-3} \tag{5.8}$$

as a function of the cosmic scale factor a, and the universe is matter dominated (Einstein-de Sitter). This is a natural situation at high redshift, ($z \gtrsim 2$ for galaxy scale); when a halo forms, its density reflect the mean density of the universe at the time of formation; e.g., in a spherical top-hat collapse model during matter domination, halo has a mean density $18\pi^2 \approx 178$ times the critical density [72]. The inner part of a halo ($\{\rho_0, r_s\}$) decouples from the expanding universe, at low redshifts, when the mass accretion rate get smaller. Self-similar solution is a natural model for a halo in between rapid growth era at high redshift and isolated era.

Let $\Delta_c(t) \equiv \rho_c(t)/\rho_0(t)$ be the central density relative to the halo inner density $\rho_0(t)$, which represents the amount of relaxation; $\Delta_c = \mathcal{C} = 2.0$ for a maximally relaxed SIDM halo. Under the assumption (5.8) for ρ_0, the equation of the semi-analytic model (5.5) reads,

$$\dot{\Delta} - 3H\Delta_c = -\frac{1}{t_r}\mathcal{F}(\Delta_c), \tag{5.9}$$

where the dot is the time derivative, and $H = \dot{a}/a$ is the Hubble parameter. Self-similar solution is a solution of this equation with constant Δ_c with time, which is a solution of an algebraic equation,

$$3t_r H\Delta_c = \mathcal{F}(\Delta_c). \tag{5.10}$$

Such constant Δ_c exists if and only if the relaxation time $t_r \propto (\rho_0^{3/2}\sigma r_s)^{-1}$ is a constant faction of the Hubble time $H^{-1} \propto t$ at all times. With the Friedmann equation in matter domination, $H \propto a^{-3/2}$, the condition is also equivalent to a constant Knudsen number $(\rho_0\sigma r_s)^{-1} = const.$[2] For a variable hard sphere cross section $\sigma \propto v^{-\eta}$, the scale radius needs to grow as,

$$r_s \propto a^{3(1-\eta/2)/(1-\eta)}. \tag{5.11}$$

which means a mass growth,

$$M \propto \rho_0 r_s^3 \propto a^{3(2-\eta/2)/(1-\eta)}. \tag{5.12}$$

Mass growth rate, with a initial random Gaussian perturbation, depends on its power spectrum; for a hard sphere cross section ($\eta = 0$), a power-law power spectrum $P(k) \propto k^n$ with $n = -2.5$, gives the self-similar solution; the index is a reasonable approximation for galactic halos [4].

The solution Δ_c is the point of intersection of a curve $y = \mathcal{F}(\Delta_C)$ and a line $y = 3(t_r/H^{-1})\Delta_c$, which are plotted in Fig. 5.4) on the left panel. The figure also shows that the self-similar solution is the unique attractor solution of the ODE (5.9) for self-similar halo ($t_r H = const$). Even if $t_r H$ were not constant, the algebraic equation would be an approximate solution if the self-similar Δ_C is nearly constant during the Hubble time, which requires that the combination $t_r H$ is nearly constant during the Hubble time. Note, also, that the solution may not be attracted to the self-similar solution enough if the relaxation time is much longer than the age of

[2]This is also proportional to the Q parameter ($Q = \rho_{\rm crit}\sigma r_{\rm vir}$) in Ahn & Shapiro [4]

universe. On the right panel of Fig. 5.4), the solution Δ_c is plotted as a function of $t_r H$, the ratio of the relaxation time to the Hubble time. Although we do not write down explicitly, the value of $t_r H$ necessary to have a central density Δ_c is an elementary function of Δ_c, by a simple calculation. In the large Δ_c limit, the function $\mathcal{F}$ has a simple power law form,

$$\mathcal{F}(\Delta) \approx \frac{\Delta^3}{2A^2} \quad (\text{for} \quad \Delta \gg 1). \tag{5.13}$$

This gives a simple power law form for the central density,

$$\Delta_c = \sqrt{6} A (t_r / H^{-1})^{1/2} \propto \sigma^{-1/2}, \tag{5.14}$$

in the small σ limit.

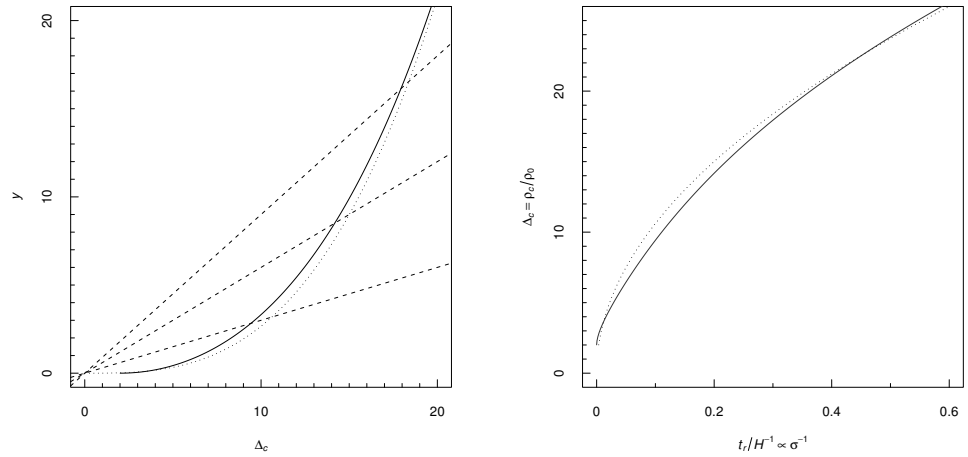

Figure 5.4: Self-similar solution of the semi-analytic relaxation model. (*Left:*) The plot of function $y = \mathcal{F}(\Delta_c)$ (solid curve), and dashed lines $y = 3(t_r/H^{-1})\Delta_c$ for $t_r/H^{-1} = 0.1, 0.2, 0.3$, respectively, in the order of increasing slopes. The intersection gives the central density $\Delta_c = \rho_c/\rho_0$ of the self-similar solution. Dotted line is an asymptotic form of the function $\mathcal{F}(\Delta_c) \approx \Delta_c^3/(2A^2)$ (*Right:*) The central density Δ_c as a function of relaxation time in the unit of Hubble time (solid line). Dotted line is the asymptotic solution $\Delta_c \approx \sqrt{6}A\sqrt{t_r/H^{-1}}$ for $\Delta \gg 1$.

Chapter 6

Statistical Properties of SIDM Halos in ΛCDM

Our semi-analytic relaxation model needs a history of NFW profile $\{\rho_0(t), r_s(t)\}$ as input; we extract an ensemble of halo histories from cosmological collisionless N-body simulations. We obtain the statistical distribution of SIDM halos, and compare the results with observed dwarf and Low Surface Brightness (LSB) galaxies and density profiles of cluster of galaxies.

6.0.2 Cosmological Collisionless N-body Simulations

The cosmological simulations has periodic boundary conditions, and cosmological parameters $\Omega_m = 0.25$, $\Omega_\Lambda = 0.75$, and Hubble constant, $h = 0.7$. Initial condition is a random Gaussian field parametrized by the power-law index $n_s = 0.95$ and amplitude $\sigma_8 = 0.8$. The power spectrum is calculated by a publicly available code `CAMB` [116], and the N-body particles on regular grid is perturbed by the second order Lagrangian perturbation theory with the publicly available `2LPT initial conditions code` [45], at redshift $z = 99$. We use three boxsizes, $L = 10.5, 21$ and $420h^{-1}$Mpc on a side, to cover dwarf galaxy scale $\sim 10^{10} M_\odot$ and cluster of galaxy scales $\sim 10^{14} - 10^{15} M_\odot$. Number of particles are $N = 256^3$, and additionally $N = 512^3$ for the $L = 420h^{-1}$Mpc box simulation. Because the collapse fraction decrease with mass, we need to use a large box to have enough

name	boxsize L $[h^{-1}\mathrm{Mpc}]$	N	m $[h^{-1}M_\odot]$	N_{halo}
L10	10.5	256^3	4.79×10^6	459
L21	21	256^3	3.83×10^7	653
L420a	420	256^3	3.06×10^{11}	223
L420b	420	512^3	3.83×10^{10}	6,329

Table 6.1: Numbers for the uniform resolution cosmological simulations to obtain an ensemble of halo histories. Boxsize L is the length of the periodic simulation box on a side, N is the number of particles, m is the mass of N-body particles, and N_{halo} is the number of halos with more than 1000 particles.

sample of cluster-sized halos. The simulations are summarized in Table 6.1; we label the simulations with the box size, L10, L21, L420a and L420b, where L420a is the $N = 256^3$ simulation and L420b is the $N = 512^3$ simulation. The gravitational softening length of the N-body particles are set to 0.5% of the mean separation, which is small enough to have a correct gravitational forces on lengths of scale radius r_s, [122].

We output 200 snapshots uniformly separated in $\ln a$ between the initial redshift and the present $z = 0$, where a is the scale factor. For each snapshot, halos are found by the friends-of-friends algorithm [47], using a publicly available code using a kd-tree.[1] We calculated NFW parameters of halos and solve the semi-analytic relaxation model in the way we described in § 5.2. We use halos with more than 1000 particles at present.

[1] `http://www-hpcc.astro.washington.edu/tools/fof.html`

6.0.3 Comparison with Observed Galaxy Rotation Curves

We apply the semi-analytic relaxation model applied to halos in the small-box simulations, run L10 and L21, and compare them with observed rotation curves of dwarf and LBS galaxies. Those rotation curve are thought to represent the underlying dark matter distribution, because those galaxies are dark matter dominated down to the core radius.

Observers often use the pseudo-isothermal profile,

$$\rho(r) = \rho_c / (r^2 + r_{\rm iso}^2) \tag{6.1}$$

to fit the dark matter contribution in observed rotation curves, which has two free parameters ρ_c and r_c; the maximum circular velocity, $V_{\rm max}$, is related to those parameters via,

$$V_{\rm max} = r_{\rm iso} \sqrt{4\pi G \rho_c} \tag{6.2}$$

We showed in § 4.5.2 that circular velocity curves of SIDM halos can be fitted by the pseudo-isothermal profile, as well, using the results of Monte Carlo scattering simulations. We also showed that the maximum circular velocity $V_{\rm max}$ is related to the NFW profile independent of the relaxation, and the core radius $r_{\rm iso}$ can be calculated as a function of the other two parameters ρ_c and $V_{\rm max}$. Our relaxation model gives the central density ρ_c for given cross section, thus it provides the complete information for the rotation curve $\{\rho_c, r_{\rm iso}, V_{\rm max}\}$ for all halos in the collisionless N-body sample.

Fig. 6.1 shows the distribution of central density ρ_c, core radius $r_{\rm iso}$ for halos in our simulation that have various maximum circular velocity $V_{\rm max}$. The

self interaction are hard sphere cross sections with $\sigma = 0.03, 0.1, 0.3, 0.5, 1.0$ and $5.0\,\mathrm{cm^2 g^{-1}}$. The mean and the standard deviation values of ρ_c as a function of $V_{\max}$ are plotted on the upper-left panel. Similarly the values for ρ_c versus $V_{\max}$, and ρ_c versus r_c are plotted on lower-left and upper right, respectively. Those relations of the mean are almost linear in logarithmic coordinates. We fit the logarithmic quantities with lines,

$$\log_{10}(\rho_c/\rho_{\mathrm{crit},0}) = \log_{10}\tilde{\rho}_c^{(100)} + \alpha_{\rho V}\log_{10}(V/100\ \mathrm{km\ s^{-1}}) \tag{6.3}$$

$$\log_{10}(r_{\mathrm{iso}}/1h^{-1}\ \mathrm{kpc}) = \log_{10}\tilde{r}_c^{(100)} + \alpha_{rV}\log_{10}(V/100\ \mathrm{km\ s^{-1}}) \tag{6.4}$$

$$\log_{10}(\rho_c/\rho_{\mathrm{crit},0}) = \log_{10}\tilde{\rho}_c^{(1\mathrm{kpc})} + \alpha_{\rho r}\log_{10}(r_{\mathrm{iso}}/1h^{-1}\ \mathrm{kpc}) \tag{6.5}$$

with the least square method for the simulated halo samples. The best-fit lines are almost parallel to other lines with different values of cross section. We also plotted the values in the literatures on dwarf or LBS galaxy observation by de Blok et al. [49], Gentile et al. [64], Kuzio de Naray et al. [111] by data points with error bars.

In Fig. 6.2 we plot the distributions around the lines. On the left panel, we plot the distribution of the quantity,

$$\log_{10}(\rho_c/\rho_{\mathrm{crit}}) + 0.6\log_{10}(V_{\max}/100\ \mathrm{km\ s^{-1}}), \tag{6.6}$$

which is the distance to the line (6.3) with $\alpha_{\rho V} = -0.6$ and zero intercept. The gray histograms are the distribution of our semi-analytic results for different cross sections; each color curve is the Gaussian distribution that have the mean and the standard deviation of the data, which shows that the distribution is Gaussian. The histogram with larger bin width shows the distribution of the observed quantities.

	$\rho_c - V_{\rm max}$		$r_{\rm iso} - V_{\rm max}$		$\rho_c - r_{\rm iso}$	
$\sigma[{\rm cm}^2\,{\rm g}^{-1}]$	$\alpha_{\rho V}$	ρ_c^{100}	α_{rV}	$r_{\rm iso}^{100}$	$\alpha_{\rho r}$	$\rho_c^{\rm 1kpc}$
0.03	-0.614	84.0	1.31	0.89	-0.588	73.74
0.1	-0.627	45.2	1.31	1.22	-0.588	47.8
0.3	-0.634	25.2	1.32	1.62	-0.583	31.7
1.0	-0.612	13.3	1.31	2.23	-0.572	20.0
5.0	-0.548	6.3	1.27	3.25	-0.576	11.5

Table 6.2: Best fit Parameters for the results of semianalytic relaxation model in dwarf/LSB scales. See Eqs. (6.3)-(6.5) for the definitions.

Similar plot with r_c instead of ρ_c is plotted on the right panel. The mean values of the observation for both panels are similar to those for SIDM halos with $\sigma = 0.3$, but the standard deviation of the observations are about a factor 3 larger than that of our SIDM halos. The observation data points here are only about 20, and also not a complete samples, however; we need more investigations to see whether the observed rotation curves are consistent with SIDM halos, statistically.

6.0.4 Comparison with Observed Galaxy Cluster Density Profiles

We compute the distribution of the central density ρ_c and the core radius in our cored NFW profile r_c (§ 4.5). We compare the results with a observation of a cluster of galaxy. For clusters, their density profiles are consistent with the NFW profile, therefore, the cored NFW profile of SIDM halos may contradict with observations. In other words, the cluster observations put an upper limit on the value of cross sections.

We plot the mean and the standard variance of ρ_c and r_c, respectively, as function of mass M_{500} in Fig. 6.4. Those averages are a power law function of the

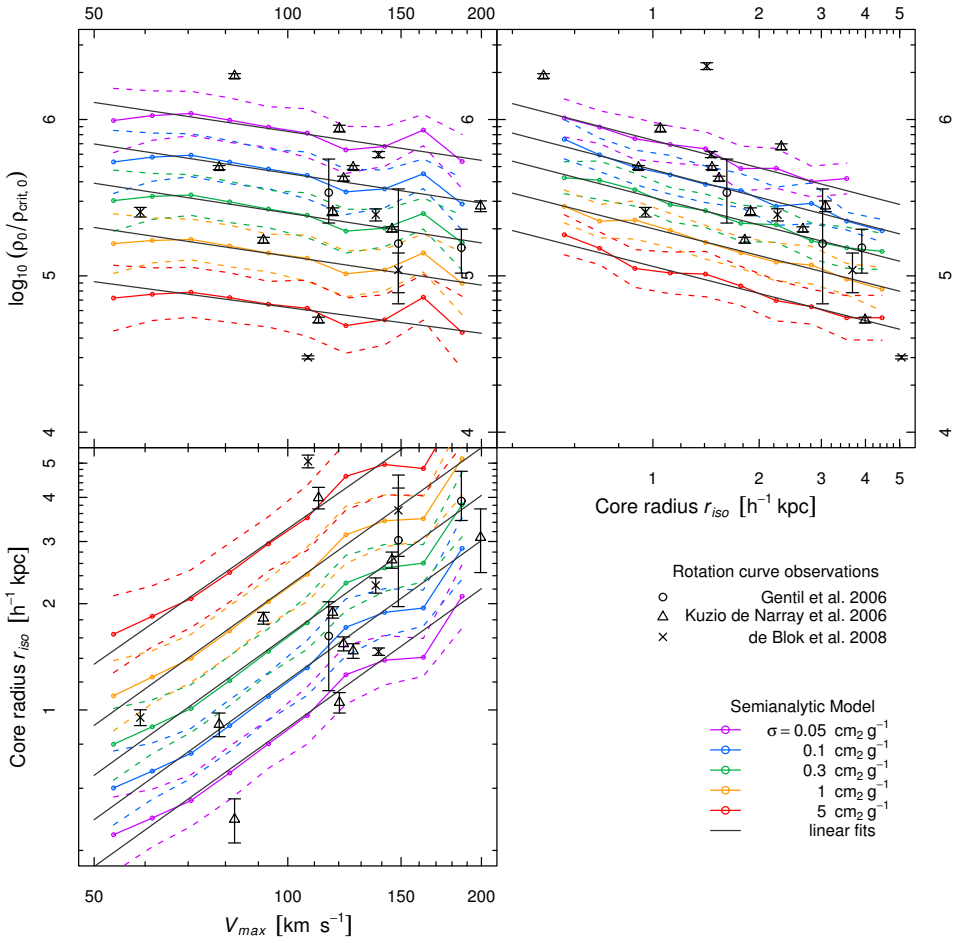

Figure 6.1: SIDM halo statistics on dwarf and LSB galaxy scales at $z = 0$. Vertical axes on the upper two panels are the central density ρ_c in unit of current critical density $\rho_{\rm crit,0}$; horizontal axis of the left columns are maximum circular velocity $V_{\rm max}$; the horizontal axis of the top-right panel, and the vertical axis of the left-bottom panel is the core radius $r_{\rm iso}$ in the pseudo-isothermal profile. Solid lines are the mean logarithmic values in our semi-analytic model with different values of hard sphere cross sections, $\sigma = 0.03, 0.1, 0.3, 1.0.5.0\,{\rm cm}^2{\rm g}^{-1}$; dashed lines are values one standard deviations above and below the mean values. Points with error bars are taken from literatures on observing rotation curves of dwarf and LBS galaxies [49, 64, 111].

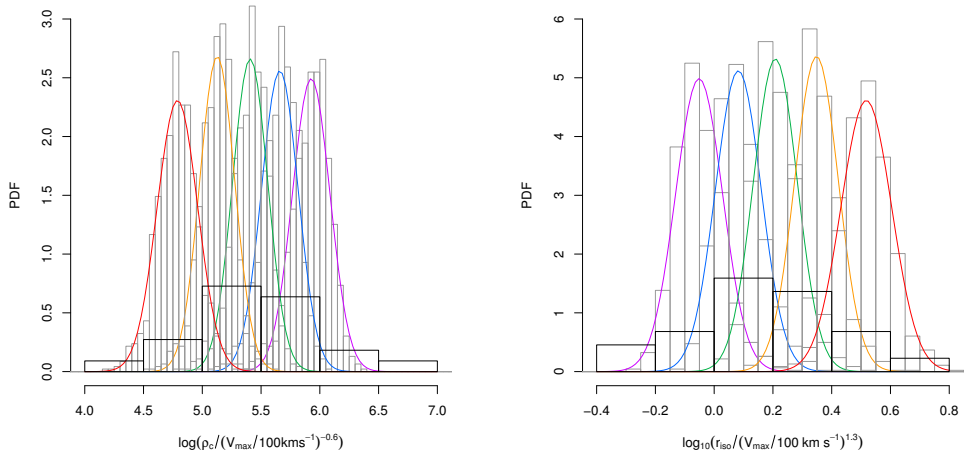

Figure 6.2: Distribution of SIDM halo properties in dwarf and LSB galaxy scales. (*Left:*) The distribution of scaled central densities $\log_{10}\left[(\rho_c/\rho_{\rm crit,0})/(V_{\rm max}/100\ {\rm km\ s^{-1}})^{-1.3}\right]$, which is the value of central densities around a line $\log_{10}(\rho_c/\rho_{\rm crit,0}) = -0.6\log_{10}(V_{\rm max}/100\ {\rm km\ s^{-1}})$. Each gray histogram is shows the distribution of that quantity in our semi-analytic calculations with different cross sections, plotted with a Gaussian distribution with the mean and standard deviation of the sample. (*Right:*) Same as the left panel but shows the pseudo-isothermal core radius $r_{\rm iso}$ in h^{-1}kpc, scaled as $\log_{10}(r_c/(V_{\rm max}/100{\rm km\ s^{-1}}$. Both quantities are log-normal distributions. The distribution of SIDM halos agree with the observed rotation curves in terms of the means with $\sigma = 0.3$, but the standard deviation is about a factor 3 larger for the observation than our SIDM model; note, however, that the observation data we plotted here are not a complete set of dwarf/LSB galaxies.

mass, and the distribution around the average is a log-normal distribution. Distribution of core radii around a power law is shown in Fig 6.5.

We compare the distribution with a cluster A2029. We first find the upper limit on the core radius r_c in our cored NFW formula. The mass of A2029 profile is accurately known by an observation by the *Chandra* X-ray observatory [117]. The cluster is nearby, at redshift $z = 0.0767$ and has X-ray temperature 7.54 ± 0.15 keV. The mass profile is well described by an NFW profile with parameters, $r_s = 540 \pm 90$kpc and $4\pi\rho_0 r_s = 1.90 \times 10^{15} M_\odot$. This best-fit gives $c_{500c} \equiv r_{500c}/r_s = 3.0$, $M_{500c} = 8.48 \times 10^{14} M_\odot$ or $c_{200c} \equiv r_{200c}/r_s = 4.5$kpc, $M_{200c} = 1.19 \times 10^{15}$ (Values assumed Hubble constant $h = 0.7$). The virial mass is consistent with the known mass-temperature relation. There is a cD galaxy at the center of the cluster, which may be baryon (star) dominated. The cD galaxy has a effective radius $r_e = 76$kpc, which includes the half of surface luminosity in the de Vaucouleurs profile. In Fig. 6.3, we plot the observed mass profile of this cluster by [117], and plotted our cored NFW formula for various core radius r_c, but with fixed best-fit ρ_0 and r_s values, because the core is not large enough to change outer mass profile at radius $\sim r_s$. Cored NFW profile with $r \lesssim 50$kpc are consistent with the observed profile if the highly uncertain mass-to-light ratio (M/L) is adjusted as a free parameter; stellar mass may dominate the mass in the SIDM core, and make the total mass consistent with the observation. For $r_c \gtrsim 50$ the SIDM cored NFW profile have too small mass around $r \sim 100$kpc which is difficult to be explained by stellar mass; therefore, we set an upper limit on core radius $r_c < 50 = 35h^{-1}$kpc from this cluster. The upper limit gives a upper limit on the logarithmic scaled core

radius, which we temporarily call x,

$$x \equiv \log_{10}\left[(r_c/1h^1\mathrm{kpc})/(M_{500}/10^{14}h^{-1}M_\odot)^{0.53}\right] < 1.1, \qquad (6.7)$$

which is $\log_{10}$ of the core radius scaled to $M_{500} = 10^{14}h^{-1}M_\odot$ along the linear fit line with slope 0.53 in Fig. 6.4.

The distribution of x is plotted in Fig 6.5. SIDM halos with $\sigma = 0.03\,\mathrm{cm}^2\mathrm{g}^{-1}$, in our semi-analytic calculations, has a Gaussian distribution with mean 1.1 and standard deviation 0.16 for x. For larger cross sections in the figure, SIDM halos with $x < 1.1$ are in minority. For $\sigma = 0.3\,\mathrm{cm}^2\mathrm{g}^{-1}$, mean is 1.35 and standard deviation is 0.16, the upper limit $x = 1.1$ is only 1.6σ away from the mean;[2] $\sigma = 0.3\,\mathrm{cm}^2\mathrm{g}^{-1}$ cannot be excluded from one cluster.

Although, there are not many clusters that have known density profile as accurate as A2029, many cluster have density profiles consistent with NFW. With future observations, fitted with the cored NFW formula, the velocity independent cross section (hard sphere cross section) may be constrained to $\sigma < 0.03$, if A2029 with $x < 1$ is a typical cluster. Constraints from mass profiles of relaxed clusters is a potential to be much better than those from the merging "bullet cluster," $\sigma < 0.7\,\mathrm{cm}^2\mathrm{g}^{-1}$.

Constraints on cross section on galaxy cluster scale does not necessarily constrain the cross section at dwarf galaxy scale if there is a velocity dependence. We show how the results of a velocity dependent cross section change the core

[2]This σ is the standard deviation, not cross section.

radius distribution in Figs. 6.6 and 6.7; we plot figures similar to 6.4 and 6.5, but for Yukawa-like velocity dependent cross sections, instead of velocity independent hard sphere cross sections. The cross section in the low velocity scale is set to $\sigma_0 = 0.3\,\mathrm{cm}^2\mathrm{g}^{-1}$, which gives the average dwarf and LBS galaxy properties as described in the previous section. The velocity cutoff parameters are set to $v_c = 100, 200, 500$ and 1000 km s^{-1} in the figures. For $v_c = 500$ and 1000 km s^{-1}, the upper limit on the scaled radius ($35h^{-1}$kpc) corresponds to $x = 1.2$ and 1.3, respectively, in which the best fit slope in Fig. 6.6 are used. The distribution of x for $v_c = 500$ km s^{-1} has a mean 0.65 and standard deviation 0.16, while the upper limit from the cluster A2029, $x = 1.3$ is 3.9σ larger than the SIDM values. Thus the observed cluster A2029 is consistent with a cross section $\sigma_0 = 0.3\,\mathrm{cm}^2\mathrm{g}^{-1}$ if there is a Yukawa-like velocity dependence with a cutoff scale $v_c \lesssim 500,$ km s^{-1}.

6.1 Conclusion

We applied our semi-analytic SIDM relaxation model to a sample of halo histories extracted from collisionless N-body simulations. With this model, we are able to calculate the consequences of SIDM collisions without running a computationally expensive Monte Carlo N-body simulations with many values of cross sections. We obtained a statistical distribution of SIDM halo properties for the first time.

We showed that average central density and core radius of dwarf or LSB galaxies are consistent with SIDM halos with hard sphere cross sections $\sigma = 0.3\,\mathrm{cm}^2\mathrm{g}^{-1}$. The scatter around the average seems to be larger in the observed galaxies than in SIDM halos, but we need more samples and may need consider

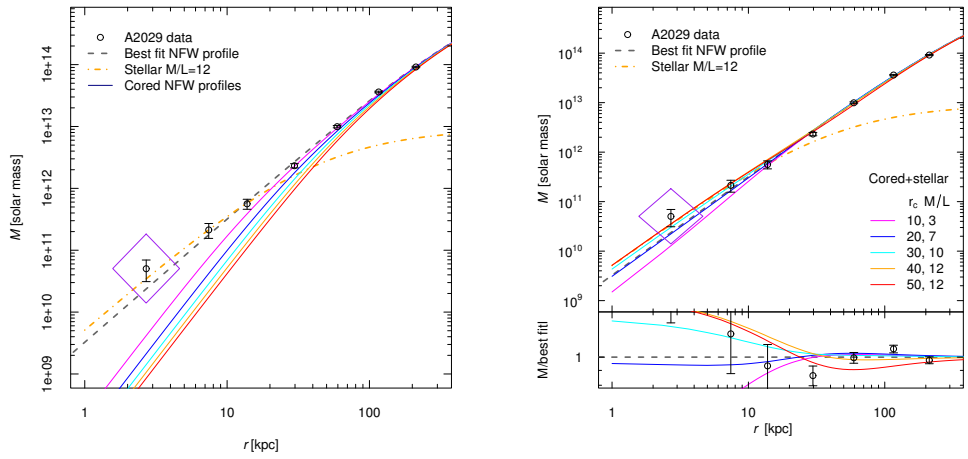

Figure 6.3: Observed mass profile of a nearby galaxy cluster A2029 (at $z = 0.0767$) taken from Lewis et al. [117], plotted with cored NFW profiles (*left*), and the sums of cored NFW profiles and stellar mass profiles (*right*), with various core radius r_c and stellar mass to light ratio (M/L). Gray dashed line is the best-fit NFW profile; the yellow dash-dotted line is the stellar mass assuming a M/L ratio 12, but M/L is highly uncertain. A diamond at innermost point shows the additional systematic uncertainty in the observation. Two parameters, $\rho_0, r_s = 540$kpc, in the cored NFW formula, are fixed to those values for the best-fit NFW profile, which are accurately constrained at larger radius. Although small cores $r_c \lesssim 40$kpc cannot be excluded due to uncertain stellar mass contributions, core radii larger than 50kpc are difficult to satisfy the mass profile at $r \sim 100$kpc.

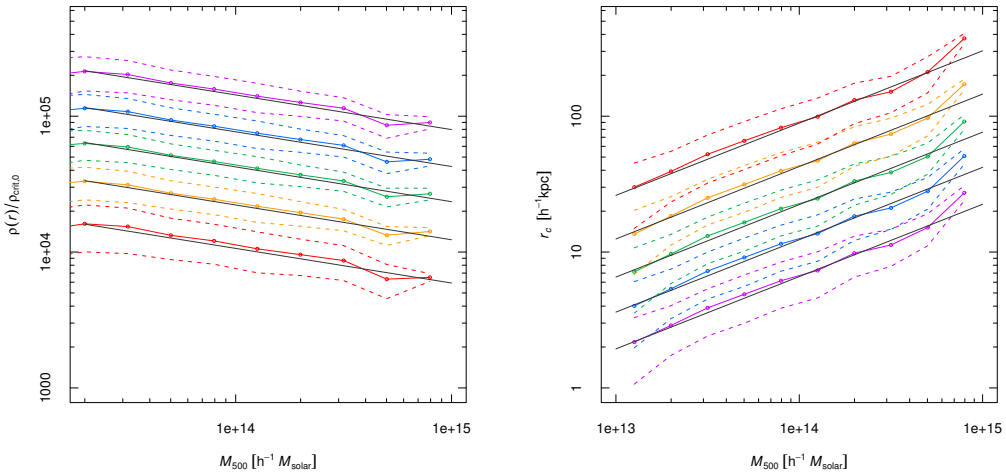

Figure 6.4: SIDM halo statistics on cluster scale. (*Left:*) Average and standard deviation of central densities ρ_c as a function of Mass M_{500}. (*Right:*) Same plot for core radius $r_c \equiv r_s\rho_0/\rho_c$ in our cored NFW profile. The SIDM model is the hard sphere cross section with $\sigma = 0.03, 0.1, 0.3, 1.0, 5.0\,\mathrm{cm^2 g^{-1}}$; ρ_c decrease with σ and r_c increase with σ, respectively.

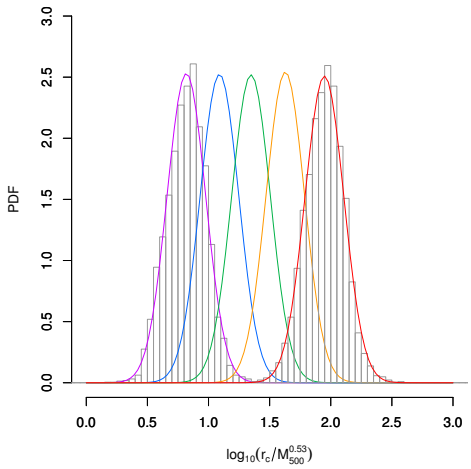

Figure 6.5: Distribution of scaled SIDM core radii in galaxy cluster scales. Horizontal axis is core radius r_c is in unit of h^{-1}kpc divided by $M_{500}/10^{14}h^{-1}M_\odot$ in logarithmic scale. The histogram shows the actual distribution of halos in our semi-analytic calculations (only for two cross sections are plotted), and the Gaussian curve shows their mean and standard deviation with the hard sphere cross section with $\sigma = 0.03, 0.1, 0.3, 1.0.$, and $5.0\,\mathrm{cm}^2\mathrm{g}^{-1}$ from left to right.

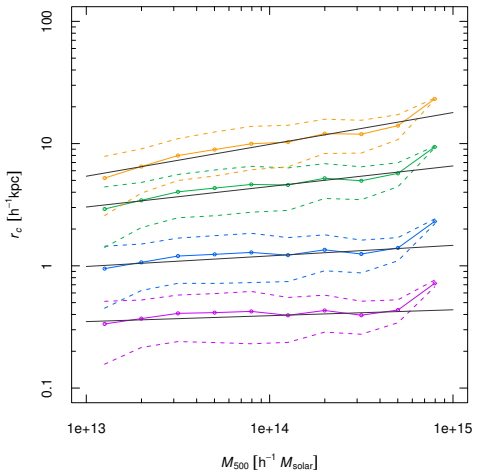

Figure 6.6: Same as Fig. 6.4 but for Yukawa-like velocity dependent cross sections. The cutoff velocities are $v_c = 100, 200, 500, 1000$; smaller v_c gives smaller cross section, therefore a smaller core radius.

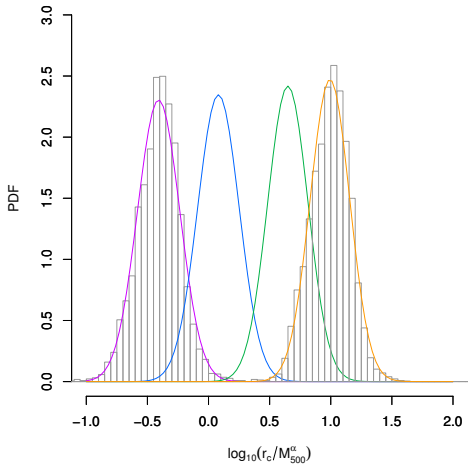

Figure 6.7: Same as Fig. 6.5 but for Yukawa-like velocity dependent cross section. The best-fit slope $\alpha = 0.048, 0.086, 0.168, 0.260$ are used for $v_c = 100, 200, 500, 1000$ km s^{-1} respectively. Larger v_c gives smaller cross sections and smaller core radii. The distribution shows that the core radius constraint by A2029 is satisfied for $v_c = 500$ and smaller v_cs.

$\sigma[\mathrm{cm}^2\,\mathrm{g}^{-1}]$	slope α	intercept β	residual R
0.03	0.532	0.829	0.157
0.1	0.533	1.09	0.158
0.3	0.533	1.35	0.158
1.0	0.533	1.63	0.157
5.0	0.532	1.95	0.159

Table 6.3: Best fit Parameters for the r_c-M_{500} relations in the semianalytic relaxation model with hard sphere cross section. The best-fit slopes and intercepts of a linear fit $\log_{10}(r_c/1h^{-1}\,\mathrm{kpc}) = \alpha\log_{10}(M_{500}/10^{14}h^{-1}M_\odot) + \beta$, and the standard deviations of the residuals is listed.

possible addition observational effect or baryonic effect on observed halos. Also intrinsic scatter of theory in N-body may be larger than that in the relaxation model, because mergers and substructures may cause additional fluctuation in the amount of relaxation.

We presented the distribution of the scaled core radius for halos in the scale cluster of galaxies. By comparing with a mass profile of one cluster, A2029, we showed that the hard sphere cross section $\sigma \geq 1.0$ are excluded by about 3σ. We provide a "cored NFW" fitting formula, and the distribution of its core radius for various cross sections, so that future observations can put further constraints on SIDM cross sections.

We also show that a velocity dependence in the scattering cross section (e.g. $\sigma_0 = 0.3\,\mathrm{cm}^2\mathrm{g}^{-1}$ and $v_c = 500\mathrm{kmg}^{-1}$ or smaller v_c), SIDM can have cored profiles consistent with average dwarf and LSB galaxies in low mass scale, and simultaneously satisfy the constraint on the cluster of galaxy scales.

v_c[km s^{-1}]	slope α	intercept β	residual R
100	0.048	-0.408	0.173
200	0.086	0.081	0.169
500	0.168	0.649	0.164
1000	0.260	0.993	0.161

Table 6.4: Same as Fig. 6.3, but for Yukawa-like cross section with $\sigma_0 = 0.3\,\mathrm{cm}^2\mathrm{g}^{-1}$ for several cut-off velocity v_c.

Part II

A Collision of Clusters of Galaxies

Chapter 7

The Cluster-Merger Shock in 1E 0657-56

The merging galaxy cluster 1E 0657-56, known as the "bullet cluster," is one of the hottest clusters known. The X-ray emitting plasma exhibits bow-shock-like temperature and density jumps. The segregation of this plasma from the peaks of the mass distribution determined by gravitational lensing has been interpreted as a direct proof of collisionless dark matter. If the high shock speed inferred from the shock jump conditions equals the relative speed of the merging CDM halos, however, this merger is predicted to be such a rare event in a ΛCDM universe that observing it presents a possible conflict with the ΛCDM model.

We examined this question using high resolution, 2D simulations of gas dynamics in cluster collisions to analyze the relative motion of the clusters, the bow shock, and the contact discontinuity, and relate these to the X-ray data for the bullet cluster. We find that the velocity of the fluid shock need not equal the relative velocity of the CDM components. An illustrative simulation finds that the present relative velocity of the CDM halos is 16% lower than that of the shock. While this conclusion is sensitive to the detailed initial mass and gas density profiles of the colliding clusters, such a decrease of the inferred halo relative velocity would

significantly increase the likelihood of finding 1E 0657-56 in a ΛCDM universe.[1]

7.1 Introduction

We use gas dynamical simulations of the nearly head-on collision of two unequal-mass clusters to model the "bullet cluster" 1E 0657-56, to show that the high shock velocity of 4700 km s^{-1} inferred from X-ray observations [126, 128] may exceed the relative velocity of the merging halos. Previous estimates of the extremely small probability of finding such a high-velocity cluster-cluster collision in a ΛCDM universe assumed that the shock and the halo-collision velocities were the same [58, 76]. Our results, first described in Milosavljević et al. [137], significantly increase the likelihood of observing such a merger event in ΛCDM.

7.2 Simulation

We used the adaptive mesh-refinement (AMR) ASC FLASH code [61] in 2D cylindrical coordinates to simulate a region 20 Mpc across, with 1 kpc spatial resolution. Gravity is contributed by two rigid, spherical DM halo profiles, whose centers free-fall toward each other from rest at separation 4.6 Mpc. The density associated with the gravitational force is an NFW profile $\rho = \rho_0(r/r_s)^{-1}(1+r/r_s)^{-2}$ for the sub-cluster, and a cored profile $\rho = \rho_0(1+r/r_s)^{-3}$ for the main cluster, to imitate a non-head-on merger. The masses ($M_{500}/10^{15}M_\odot$) and radii r_{500} and r_s (Mpc)

[1] This chapter is based on Milosavljević, Koda, Nagai, Nakar, & Shapiro [137] and Koda et al. [104]

are $(1.25, 1.5, 0.5)$ and $(0.25, 0.5, 0.16)$ for the main cluster and subcluster, respectively.

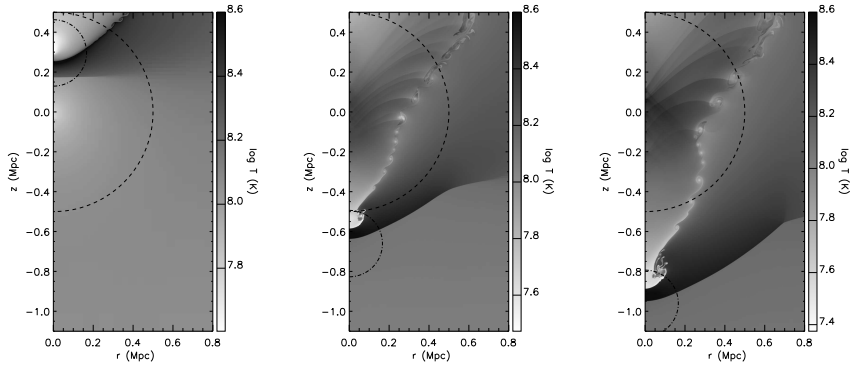

Figure 7.1: Time evolution of temperature. Larger CDM halo is centered at cylindrical $(r, z) = (0, 0)$; smaller halo is at $z = 0.29, -0.66$ and -0.96 Mpc, respectively. Circles indicate the scale radii r_s of the halos.

7.3 Results

After subhalo "bullet" passes through the center of primary halo, the subhalo gas trails the subhalo DM, led by a bow shock and contact discontinuity (cold front), as seen in Figure 7.1. The opening angle and radius of curvature of the bow shock are sensitive to simulation details, but both are larger than expected for steady-state bow shocks of hard spheres with constant velocity in a uniform medium. The wings of the contact discontinuity are Kelvin-Helmholtz unstable.

During pericenter passage, the shock and contact discontinuities are slower than the relative velocity of the two CDM halos, due to ram pressure force acting on the gas. Later, the halos climb out of the gravitational potential well and decelerate, but the shock and contact discontinuity do not decelerate (Fig. 7.2[a]). At

observed separation $D = 720$ kpc, the velocity of the shock is 4800 km s^{-1}, consistent with the 4740 km s^{-1} inferred from 1E 0657-56 data. The relative velocity of the simulated halos then is much less, 4050 km s^{-1} (16% smaller). The X-ray surface brightness and temperature profiles of the simulation viewed transverse to collision axis (Fig. 7.3) agree with those of 1E 0657-56.

Figure 7.4 shows the thermal X-ray spectrum of the simulated merging cluster. The observed spectrum of 1E 0657-56 has stronger emission above 30 keV, suggesting some additional non-thermal emission [146].

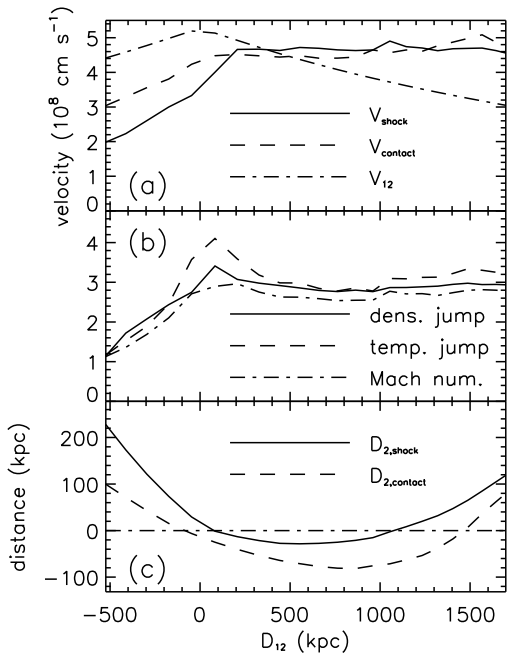

Figure 7.2: (a) Velocity of the shock, $V_{\rm shock}$, and of the contact discontinuity, $V_{\rm contact}$ relative to the preshock gas upstream, and the relative velocity of the CDM halos, V_{12}, all as functions of the time. The distance between two CDM halos, D_{12}, is used as the coordinate of time. (b) Density and temperature jump at the shock, and the shock Mach number. (c) Position of the shock (solid line) and the contact discontinuity (dashed line) relative to subhalo center.

7.4 Discussion and Conclusions

Our simulations of merging galaxy clusters show that the halo collision velocity need not be the same as the intergalactic gas shock velocity. Applying our correction to the speed of the subhalo, the probability that such a massive cluster in our CDM universe has such a high-speed subhalo increases by 3 orders of magnitude relative to previous estimates, but is still small ($\sim 10^{-4}$). Springel & Farrar [163] independently reached a similar conclusion, although their relative halo velocity is much smaller, 2600 km s^{-1}. They assumed perfectly head-on collision between a cuspy main halo and a more concentrated subhalo than ours, which would make the subhalo decelerate more before reaching the observed separation. More recent simulations by Mastropietro & Burkert [130] show that the difference between the shock velocity and the halo relative velocity is smaller if the initial halo collision velocity is larger and if the collision is not perfectly head-on. Their favored configuration to match the X-ray observations and their results are similar to ours in terms of mass ratio, the degree of off-center collision, and difference between the relative halo velocity and shock velocity.

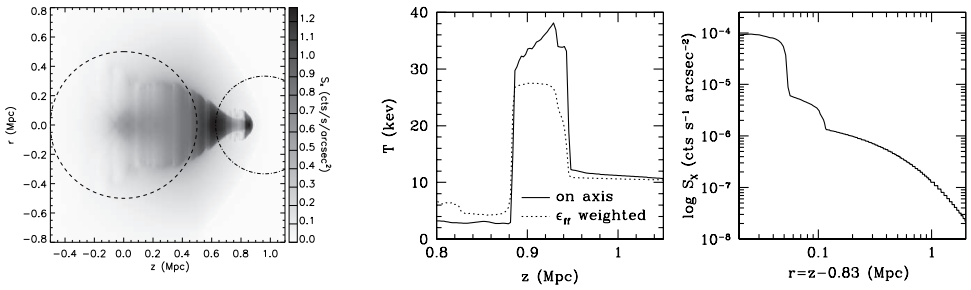

Figure 7.3: (Left:) Surface brightness map of the simulated cluster in the $0.8 - 4$ keV band. The circles indicate the scale radii r_s of the CDM halos. (Middle:) Temperature profile along collision axis (solid) and emissivity-weighted temperature, averaged over the (transverse) line of sight (dotted). (Right:) Surface brightness profile along collision axis.

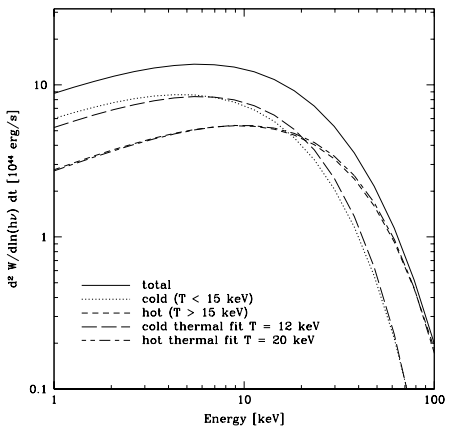

Figure 7.4: Thermal bremsstrahlung emission spectrum from simulated merging cluster: the contribution from cold gas below 15 keV (dotted) and hot gas above 15 keV (short-dash), total spectrum (solid), which is the sum of cold and hot components, and single-temperature fit to cold (long-dashed) and hot (mixed dash) components. The emission from the hot shock-heated gas ($T > 15$ keV) dominates the spectrum above 20 keV and is fitted well by a single temperature profile with $T = 20$ keV.

Part III

Abundance of Disc-Dominated Galaxies in ΛCDM

Chapter 8

On the Survival and Abundance of Disk-dominated Galaxies

We study the formation of disk-dominated galaxies in a ΛCDM universe. Their existence is considered to be a challenge for the ΛCDM cosmology, because galaxy mergers isotropize stellar disks and trigger angular momentum transport in gas disks, thus fostering the formation of central stellar spheroids. Here, we postulate that the formation of stellar spheroids from gas-rich disks is controlled by two parameters that characterize galaxy mergers, the mass ratio of merging dark matter halos, and the virial velocity of the larger merging halo. We utilize merger histories generated from realizations of the cosmological density field to calculate the fraction of dark matter halos that have avoided spheroid formation, and compare the derived statistics with the spheroid occupation fractions in surveys of nearby galaxies. We find, for example, that the survival rate of disk-dominated galaxies in ΛCDM is just high enough to explain the observed fractional representation of disk-dominated galaxies in the universe if the only mergers which lead to central spheroid formation are those with mass ratios $M_2/M_1 > 0.3$ and virial velocities $V_{\rm vir,1} > 55$ km s^{-1}. We discuss the physical origin of this criterion.[1]

[1]This work has been published as Koda, Milosavljević, & Shapiro [103].

8.1 Introduction

The existence of disk-dominated galaxies, with little or no bulge, is frequently cited as a challenge to the ΛCDM cosmology [e.g., 97, 105]. Apart from the question of whether or not the theory of galaxy formation in ΛCDM can succeed in making these observed rotationally-supported disk galaxies in the first place [2, 52], the survival of such disks, once formed, is our focus here. The mergers that every galaxy-hosting dark matter halo experiences can trigger angular momentum transport in the interstellar medium of the merger remnant. If a substantial amount of gas is transported into the central kiloparsec of the remnant, the gas can fuel a starburst forming a central stellar system—a "classical" bulge (i.e., self-gravitating, baryon-dominated stellar system supported by random motions rather than rotation). By contrast, "pseudobulges" can also arise in some disk galaxies if they have *not* experienced recent major mergers, by the secular transport of angular momentum [e.g., by galactic bars, 92]. These pseudobulges (sometimes called "disky bulges") are supported more by rotation than random motion, however [e.g., 106, and references therein].[2] About one third of all disk galaxies in the local universe do not contain bulges or pseudobulges [97][3] and another third contain only pseudobulges. Allen et al. [7] carried out a Sérsic spheroid and exponential disk decomposition on a

[2]Pseudobulges are to a larger degree supported by rotation than classical bulges and can have rotational velocity-to-1D velocity dispersion ratios $V_{\rm max}/\sigma > 1$. Their velocity dispersions are smaller than expected from the Faber-Jackson relation. Pseudobulges tend to have flattened isophotes and surface brightness profiles close to exponential. The classical bulges and pseudobulges can be distinguished from a third class, the boxy or peanut-shaped bulges, which are bars seen edge-on [11, 35].

[3]The classification of galaxies by their bulge content is usually done using simple bulge-disk or concentration models, which may not be accurate in extreme disk-dominated galaxies [e.g., 27].

large sample of galaxies and find that 30% of exponential disks have small bulge-to-total ratio $B/T < 0.2$. Barazza et al. [14] report that 20% of disk galaxies can be visually classified as bulgeless.[4]

For our purposes here, we shall assume that disk-dominance means that no classical bulge is present in a galaxy. Although the precise characteristics of mergers that form classical bulges remain unknown, disk-dominated galaxies must have avoided major mergers during and after formation. Just how large the mass ratio of the merging galactic halos must be in order to induce bulge formation is somewhat uncertain, however. Mergers of similar-mass galaxies have been shown to trigger starbursts and result in elliptical galaxies, by gas dynamical and N-body simulations for galaxy halo masses $M \gtrsim 10^{11} M_{\odot}$, merging at relative velocities of the order of the virial velocity [44, 135]. In that case, a bulge forms from the momentum-exchange and compression of gas in merger shocks and the outward angular momentum transport induced by merger torques. Pure N-body simulations of such mergers find that the pre-existing stellar disks are mixed and destroyed [e.g., 139], leaving an elliptical galaxy. For minor mergers, N-body and gas dynamical simulations with halo masses $M \gtrsim 10^{11} M_{\odot}$ indicate that disks survive but bulges can also grow [44, 56, 134, see also D'Onghia et al. 53]. However pure N-body simulations of this process find that these bulges are pseudobulge-like (i.e., partially supported by rotation), rather than classical, for mass ratios $0.1 \lesssim M_2/M_1 \lesssim 0.25$ [29], where M_1 and M_2 are the masses of the larger and smaller merging galaxy-

[4]Pure disk galaxies also contain nuclear star clusters [e.g., 26, 180] which could be products of secular gas transport [136], but these star clusters are tiny by comparison with the bulges described above.

hosting dark matter halos, respectively; hereafter, the subscripts 1 and 2 denote quantities pertaining to the larger and smaller halos, respectively. Bulge formation by the merging of lower mass ($V_{\rm max} \lesssim 70\,{\rm km\,s^{-1}}$) and gas-rich galaxies has not yet been simulated.

Semianalytic models of galaxy formation [e.g., 16, 96] assume they can track the morphological type of galaxies by converting a disk component into a spheroidal component in mergers with mass ratios $\mu \equiv M_2/M_1$ greater than some threshold. These models successfully reproduce the distribution of earlier morphological types by tuning the critical mass ratio for disk destruction, and adopting a critical bulge-to-total mass ratio that discriminates broadly between disk and elliptical galaxies. Recent semianalytic models employing merger trees extracted from hydrodynamic N-body simulations yield a similar result [125]. However, the studies that focus on the survival of disks generally do not address the abundance of *disk-dominated* galaxies. Existing ab initio cosmological simulations have yielded disks with bulges [e.g., 2], but currently lack the dynamic range to explore a large enough volume to sample the statistics of galaxy morphology while simultaneously resolving the formation and mergers of individual galaxies.

The purpose of this work is to compare the predicted disk survival probabilities during hierarchical merging in a ΛCDM universe with the observed statistics of galaxies at the end of the Hubble sequence. This comparison is then used to place constraints on the physics of bulge-forming mergers. In § 8.2.1 we discuss the role of mergers in bulge formation. In § 8.2.2 we describe the effect of cosmic reionization and Jeans-mass filtering on bulge formation. In § 8.2.3 we present a

calculation of bulge formation and disk survival probabilities derived from galactic halo merger trees generated from realizations of cosmological density fields. In § 8.2.4 we compare observed disk galaxy statistics with these merger tree results and place constraints on the properties of bulge-forming mergers. In § 8.3 we summarize our main conclusions. Standard cosmological parameters consistent with the *Wilkinson Microwave Anisotropy Probe* [162] are assumed throughout.

8.2 Disk Survival in ΛCDM Cosmology

8.2.1 Mechanisms for Bulge Formation in Mergers

The merging of gas-rich galaxies fosters bulge formation directly and indirectly. Directly, the time-dependent gravitational potential of the two merging components deflects some of the gas into the center of the merger remnant, where it gets compressed in shocks and fuels a starburst. Indirectly, the gravitational tidal field of the merging components excites nonaxisymmetric perturbations inside the merging galaxies (bars, spirals, etc.) which then torque disk gas into the center of the galaxy [e.g., 43, and references therein]. In the center, again, shocks are ubiquitous and play a role in angular momentum transport. The indirect channel should be important in minor mergers, especially where the smaller galaxy loses its gas to ram pressure stripping in the early stages of the merger.

The strength of direct merger torques is a function of the mass ratio of the host dark matter halos of the merging galaxies, $\mu \equiv M_2/M_1$. The strength of nonaxisymmetric distortions in minor mergers with $\mu \ll 1$ depends nontrivially on the resonance structure of the merging halos and the orbit of the merger [e.g., 67].

These cannot be modeled in a general case; therefore, we here consider only the gross properties of the mergers, averaged over the merger orbital parameters and over the properties of merging halos with given masses at a specific redshift.

Efficient transport of angular momentum in perturbed gas disks requires an excitation of nonlinear waves by nonaxisymmetric potential distortions that can give rise to momentum-transporting shocks.[5] The strength of merger shocks is characterized by the Mach number $\mathcal{M}$, which is the ratio of the shock velocity to the sound speed of the warm neutral gas $c_s \sim 10\,\mathrm{km\,s^{-1}}$. Merger-driven strong shocks can be radiative, because the post-shock cooling time can be much shorter than the dynamical and sound crossing times of the HI disk. In this limit the shocks are isothermal and the shock compression is $\sim \mathcal{M}^2$. This shock compression may in turn affect the rate of gravitational instability in the shocked gas and, hence, the efficiency of star formation.

In view of these considerations, we postulate that, besides the mass ratio μ, the efficiency of bulge formation in mergers is also controlled by a second parameter, the merger Mach number $\mathcal{M} \equiv V_{\mathrm{vir},1}/c_s$, where $V_{\mathrm{vir},1}$ is the virial velocity of the larger merging halo.[6] In general, the condition that determines whether a merger triggers bulge formation or not can be any function of μ and $\mathcal{M}$. Here, we do not study the gas flow in merging galaxies, and hence we cannot specify the

[5] For angular momentum transport by spiral shocks, see, e.g., Rozyczka & Spruit [151], Savonije et al. [153], and Goodman & Rafikov [69].

[6] Here and throughout the letter, $V_{\mathrm{vir}} \equiv (GM_{200}/r_{200})^{1/2}$, where M_{200} is the mass inside a sphere with radius r_{200} centered on the halo within which the mean density equals 200 times the critical density of the universe.

requirements for bulge formation in detail. Instead, we postulate a simple model of bulge formation that is characterized by two parameters, $\mu_{\rm crit}$ and $\mathcal{M}_{\rm vir,crit}$; bulges form if mergers with $\mu > \mu_{\rm crit}$ and $\mathcal{M} > \mathcal{M}_{\rm vir,crit}$ occur, but otherwise do not. By our definition of Mach number, the condition on a Mach number $\mathcal{M} > \mathcal{M}_{\rm crit}$ is equivalent to a condition on the virial velocity $V_{\rm vir,1} > V_{\rm vir,crit} = c_s \mathcal{M}_{\rm crit}$, where $c_s \sim 10$ km s^{-1} is the sound speed of gas.

An important distinct possibility is that in which bulge formation is driven *cumulatively*, rather than induced in a single merger [30]. The central density of gas in the disk of a late-type disk galaxy could increase gradually due to slow, continuous radial gas inflow. Evidence for such inflow can be found in the "central light excess" (above the exponential law) in pure disk galaxies [e.g., 27]. The inflow could be excited by perturbations associated with minor mergers. Through their differential gravitational perturbations, many consecutive minor mergers can induce a slow, secular drift in the angular momentum distribution of the disk fluid, which could lead to central accumulation without leaving any characteristic signatures of merger-driven evolution (dynamically hot stellar components, etc.). The inflow could also be driven by nongravitational processes, such as the magnetorotational instability in the gas disk [136, see also, e.g., Piontek & Ostriker 147]. The resulting increase of the central surface density brings the galaxy closer to the threshold for gravitational instability. The bulge or pseudobulge formation-triggering merger then must only nudge the galaxy over the threshold for, e.g., nuclear bar formation, where the galaxy is already marginally unstable.

For systems which are gas-poor, collisionless mergers of stars can result in

an elliptical galaxy or a classical bulge, if and only if the μ is sufficiently large [e.g., 29, 139]. This bulge formation can be characterized by merger ratio μ, but it is independent of $V_{\rm vir,1}$ because the gravitational dynamics without gas is scale free. However, there will still be a dependence on $V_{\rm vir,1}$ through the requirement that the galaxies *prior* to their merger were able to form long-lived (i.e., low-mass) stars (see below).

8.2.2 The Critical Virial Velocity for Bulge Formation after Reionization and Jeans-Mass Filtering

In order for the merger of two halos to have produced a bulge, the halos must have contained a substantial amount of gas, or else stars will have already formed from the collapsed gas. During cosmic reionization, in the process known as the Jeans-mass filtering [156], the gas content of small-mass halos, however, was affected by the reheating of the intergalactic medium (IGM) out of which the gas inside those halos collapsed. The gas pressure of the reheated intergalactic medium competes with gravitational instability, in that case, to suppress structure formation in those baryons which would otherwise have formed galaxies with virial velocity below some threshold. The Jeans length in the IGM for a gas photoheated to $\sim 10^4$ K corresponds to a halo mass after collapse and virialization for which the circular velocity is

$$V_{\rm c} = 55\,(T_{\rm IGM}/10^4\ {\rm K})^{1/2}\ {\rm km\ s^{-1}} \tag{8.1}$$

[88]. The actual threshold virial velocity is uncertain, because one must account for the time-dependent growth of fluctuations in an evolving background and because the formation of dark matter halos affects the baryons in a nonlinear way.

Estimates of the value of the velocity threshold which results range from about 30 to 80 km s^{-1} [e.g., 55, 101, 143, 172]. Whatever the precise value should be, this would impose a lower limit to the critical virial velocity of merging halos capable of producing a bulge, as described above, i.e., $V_{\rm crit,min} \sim 30 - 80$ km s^{-1} .

Since the virial velocity threshold which results from Jeans-mass filtering depends primarily on the temperature, other sources of IGM heating could have a similar effect. The supernova explosions associated with massive star formation, for example, could also heat the intergalactic gas. Such feedback could also have unbound the interstellar gas from the galaxies which formed these stars, if the galaxy virial velocities were small enough.

8.2.3 Merger Histories of Low-Mass Galaxies

To explore the sensitivity of the fractional abundance of disk-dominated galaxies produced during structure formation to the critical values of μ and $V_{\rm vir,1}$, and thus to place constraints on the values of these two parameters that are compatible with the observed statistics, we generate merger histories of low-mass, disk-galaxy hosting halos and study disk survival in this population of halos. We utilize those merger histories to calculate the abundance of disk-dominated galaxies as a function of $\mu_{\rm crit}$ and $V_{\rm vir,crit}$. We compare the resulting abundances with the incidence of late-type galaxies in the *Tully Galaxy Catalog* (§ 8.2.4).

The merger histories are generated from the nonlinear evolution of the initial, linearly perturbed cosmological density field using the publicly-available Lagrangian perturbation code PINOCCHIO [138]. The code generates a Gaussian-

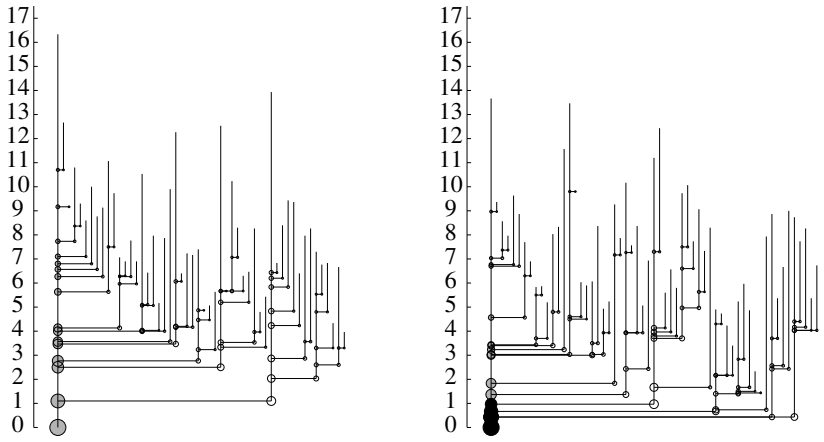

Figure 8.1: Examples of merger trees. Gray circles represent disk-dominated galaxies and black circles represent galaxies with classical bulges, respectively, under a bulge-forming criterion $\mu_{\rm crit} = 0.3$, $V_{\rm vir,crit} = 55$ km s^{-1}. Radii of circles are proportional to $M^{1/3}$. Mergers with $\mu < 0.05$ are not plotted in the figure. Vertical axis label is redshift.

random field on a cubic mesh, distributes particles on the mesh, and determines the collapse time of each particle using an ellipsoidal collapse criterion. The "collapsed" particles are moved by Lagrangian perturbation theory and related to virialized objects, which are the dark matter halos, by a linking criterion. We employed 512^3 particles with cosmological parameters $\Omega_{\rm m} = 0.24$, $\Omega_\Lambda = 0.76$, $\sigma_8 = 0.74$, and $h = 0.73$, in a cubical box with 50 comoving Mpc on a side. The mass of an individual particle was $m_{\rm part} = 3.3 \times 10^7 M_\odot$, and halos with more than 10 particles were selected for inclusion in the merger tree. For a given redshift, PINOCCHIO provides a list of all of the halos with mass $M > 10\ m_{\rm part}$ which formed inside the comoving box at this or any *earlier* redshift, and a complete list of their merger events. Each merger event is characterized by the merger redshift and the masses of the halos participating in the merger.

We compute the fraction of halos containing disk-dominated galaxies as a function of the threshold for spheroid formation that is parametrized by the critical mass ratio μ and critical virial velocity $V_{\rm vir,1}$ of the larger halo at the time of each merger. Specifically, we assume that a merger with $\mu > \mu_{\rm crit}$ will create a central stellar spheroid if the halo has a virial velocity $V_{\rm vir,1} > V_{\rm vir,crit}$. We follow the most massive progenitor branch of the merger history of each halo and identify the resulting $z = 0$ halo as containing a disk-dominated galaxy if no spheroid has yet formed in the halo based on the defined criterion.

In Fig. 8.1, we plot examples of merger trees. Gray circles represent disk-dominated galaxies and black circles represent galaxies with classical bulges, respectively, with a bulge-forming criterion $\mu_{\rm crit} = 0.3$, $V_{\rm vir,crit} = 55\,{\rm km\,s^{-1}}$. Left panel is an example that the halo host disk-dominated galaxy at present, and right panel is and example that a classical bulge was formed by present.

There are rare cases in which a progenitor mass is so small at high redshift that bulge-forming mergers are not resolved by our numerical results. We have estimated the number of such cases and confirmed that it is negligible. For $1/10 < \mu_{\rm crit} < 1/3$, the fraction of current halos in the mass range we will describe below, in which bulge-forming mergers occur with a halo containing less than 50 particles is less than 3%. For $\mu_{\rm crit} = 1/2$, the fraction increases to 8%, but the total mass of the merger remnant is small for those mergers with $\mu > 1/2$. If the smaller halo contains 50 particles, the merger remnant with $\mu > 1/2$ has at most 150 particles, which is ten times smaller than $M_{\rm min}$, the minimum mass of interest for our comparisons with present-day galaxies.

We consider halos with present masses in the range $M_{\rm min} < M < M_{\rm max}$, where $M_{\rm min} = 5 \times 10^{10} M_\odot$ (corresponding to $V_{\rm vir,min} \approx 60$ km s^{-1}) and $M_{\rm max} = 10^{12} M_\odot$ (corresponding to $V_{\rm vir,max} \approx 160$ km s^{-1}); the resulting galaxy statistics are compared with the observed galaxy statistics in the same approximate mass range. Since the halo mass and the maximum circular velocity of the galaxy disk are not known for most of the galaxies in each observed sample, we use the Tully-Fisher relation to estimate halo masses for the observed galaxies. We used the Tully-Fisher relation measured by Kannappan et al. [94]. The present total number density of halos in the above range is 0.021 Mpc^{-3}. Disk-dominated galaxy abundances thus calculated will not dependent strongly on the specific choice of $M_{\rm max}$ because halos with masses $M < M_{\rm max}$ dominate the number density of halos in the universe today. However, the abundances will be sensitive to $M_{\rm min}$. In §8.2.4 we explore the sensitivity to the choice of $M_{\rm min}$. An approach more accurate than the one employed here would dispense with $M_{\rm min}$ and would consider halos of all masses and then match the fractional disk and irregular galaxy abundances as a function of halo mass.

We ignore the finite duration of the merger, which is the time elapsed between the halo contact and the final bulge formation. This approximation is generally good as long as the dynamical friction time for a galaxy to complete its merger with a central galaxy is shorter than the age of the universe when the halo merger took place. The dynamical friction time scale was recently calibrated in N-body simulations [91],

$$t_{\rm dyn} = \frac{0.94\epsilon^{0.60} + 0.60}{0.86} \frac{1}{\mu \ln(1+\mu^{-1})} \frac{r_{\rm vir}}{V_{\rm circ}}, \tag{8.2}$$

where ϵ is the circularity parameter. Setting $\epsilon = 0.5$ and $V_{\rm circ} = V_{200}$, this simplifies to

$$t_{\rm dyn} \sim \frac{0.14}{\mu} \frac{1}{\ln(1+\mu^{-1})} H(z)^{-1}, \tag{8.3}$$

where $H(z)^{-1}$ is the Hubble time at halo merger. The dynamical friction time scale is smaller than the Hubble time for $\mu > 0.05$, and therefore the galaxy merger time due to dynamical friction is negligible in most cases. Boylan-Kolchin et al. [32] also gives a fitting formula for $t_{\rm dyn}$, which is different in detail (especially in its dependence on ϵ), but also indicates that the dynamical friction time is smaller than the Hubble time for $\mu > 0.05$ for any ϵ. For late mergers, close to the present, we should perhaps compare this dynamical friction time with the look-back time to that merger event, rather than with the age of the universe then. The late mergers are only a minority however. In the halo mass range corresponding to disk-dominated galaxy hosts, the present fraction of mergers in progress is only $\lesssim 5\%$ for mass ratios $\mu > 0.2$ and $\lesssim 10\%$ for $\mu > 0.1$.

8.2.4 Results

Figure 8.2 shows the fraction of galaxies without classical bulge as a function of the bulge formation criterion $(\mu_{\rm crit}, V_{\rm vir,crit})$, which is the result of the model described in § 8.2.3. In order to compare these theoretical contours with the observed abundance of disk-dominated galaxies, we select 2281 galaxies in the nearby universe from the *Tully Galaxy Catalog*[7] that have blue magnitudes in the range $-20 < M_B < -17$ and are located at distances $D < 20\ h^{-1}$ Mpc at which the

[7] http://haydenplanetarium.org/universe/duguide/exgg_tully.php

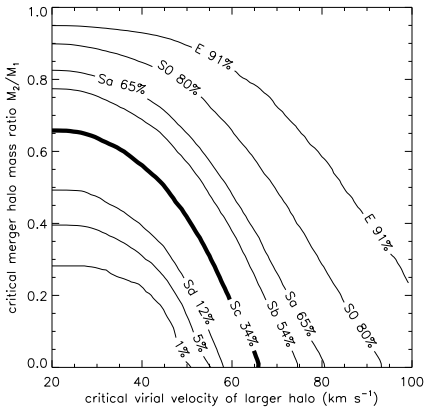

Figure 8.2: The fraction of disk-dominated galaxies (galaxies without classical bulges) that results from bulge formation criteria $(\mu_{\rm crit}, V_{\rm vir,crit})$ characterized by the critical merger mass ratio, $\mu_{\rm crit}$, and the critical virial velocity of the larger halo at merger, $V_{\rm vir,crit}$. Some of the contours are also labeled by the morphological type of galaxy in the Tully subsample such that the observed fraction of galaxies of that morphological type or later equals the theoretical fraction of disk-dominated galaxies which results from the bulge-formation criterion $(\mu_{\rm crit}, V_{\rm vir,crit})$ on that contour. As discussed in the text, we have adopted the view that galaxies of type Sc and later are the disk-dominated population (i.e., with no classical bulge), so the bold contour constitutes our theoretical expectation for the bulge-forming threshold criteria that is compatible with the observations.

catalog is reasonably complete. This luminosity range is chosen to render the number density of galaxies equal to the density 0.021 Mpc^{-3} of halos that we synthesize (see § 8.2.3). The corresponding circular velocity range calculated from the Tully-Fisher relation [e.g., 94] is $60\ \mathrm{km\ s}^{-1} < V_{\mathrm{c}} < 160\ \mathrm{km\ s}^{-1}$. This range is consistent with the range of virial velocities in our theoretical halo sample, which is a self-consistency check of our association of galaxies with dark matter halos in our numerical halo catalog for ΛCDM.

Some of the contours in Figure 8.2 are labelled with with a galaxy morphological type, as well. Each pair of morphological type and fraction printed on the contour indicates that that morphological type and later types occupy the corresponding fraction in the subsample of the *Tully* catalog. If we choose to assume that a particular morphological type (e.g., Sd, Sc, or Sb) and all later morphological types are disk-dominated galaxies, while the earlier morphological types are galaxies with classical bulges, then the fraction of disk-dominated galaxies in the subsample is explained by the parameters $(\mu_{\mathrm{crit}}, V_{\mathrm{vir,crit}})$ along the contour labeled by the chosen transitional morphological type. The classification by morphological type does not precisely separate galaxies that have classical bulges from those do not; nevertheless we assume that Sc and later type galaxies are either bulgeless or have pseudobulges, while Sbc and earlier types contain classical bulges. Assuming this correspondence, the contour "Sc" in the figure shows the parameter space locus yielding the abundance of galaxies without classical bulges.

While the criterion for the survival in mergers of a given morphological type must lie on the appropriate contour, from the statistics alone it cannot be de-

termined which specific value of $(\mu_{\rm crit}, V_{\rm vir,crit})$ along the contour is the true physical criterion for bulge formation. The critical virial velocity cannot be much less than the minimum value imposed by Jeans-mass filtering discussed in §8.2.2. If $V_{\rm vir,crit} = V_{\rm crit,min} = 55\,{\rm km\,s^{-1}}$ (see, eq. [8.1]), then $\mu_{\rm crit}$ is 0.3 on the Sc contour. That is, the observed abundance of disk-dominated galaxies is consistent with the hypothesis that mergers with $\mu > 0.3$ in halos with $V_{\rm vir,1} > 55\,{\rm km\,s^{-1}}$ create classical bulges, while mergers that do not satisfy these criteria do not. This $\mu_{\rm crit}$ is consistent with the threshold value such that mergers with larger mass ratio result in a random-motion-dominated ellipsoid in dissipationless N-body simulations [29]. However, since the precise value of $V_{\rm vir}$, below which gas collapse is suppressed is not known, a somewhat larger $\mu_{\rm crit}$ and somewhat smaller $V_{\rm vir,crit}$ and vice versa would be equally plausible, e.g., $(\mu_{\rm cirt}, V_{\rm vir,cirt}) = (0.3^{+0.3}_{-0.2}, 55^{-10}_{+5}\,{\rm km\,s^{-1}})$.

Were the critical velocity for bulge formation above $\sim$ 65 km s^{-1}, however, then the relative abundance of disk-dominated galaxies would be greater than observed for all mass ratios μ. In that case, there would be too few galaxies with bulges relative to their observed abundance. A similar upper limit to $V_{\rm vir,crit}$ results from the fact that classical bulges are unlikely to form from mergers that are too minor. If $V_{\rm vir,crit} \sim 65\,{\rm km\,s^{-1}}$, then mergers will over-produce disk-dominated galaxies unless $\mu_{\rm crit} \ll 1$, which may be implausibly small (i.e., not major mergers). To identify the true, unique criterion for bulge formation, one must resort to physical insight to exclude such implausible, extreme criteria that are still allowed by the statistics.

The Kautsch et al. [97] sample of edge-on disk galaxies gives a similar disk-

dominated galaxy fraction. If we assume the same additional fraction of early-type galaxies as in the Tully subsample, the fraction of Sd is 11% and the fraction of Sc or later is 45%.

The assumption that the Tully-Fisher relation can be used to relate the luminosities of galaxies in the Tully catalog to their halo virial velocities (and, hence, to their masses, M_{200}) works best for the spiral galaxies but is less certain for the elliptical and S0 galaxies. The Tully-Fisher relation for S0 galaxies is shifted to lower luminosity by about $M_B \sim +1.5$ for each $V_{\rm max}$, and the scatter is larger compared to spirals [18]. This estimate is uncertain because the Tully-Fisher relation or virial mass-to-light ratio is unknown for S0s at small masses near $M_{\rm min}$. The virial mass-to-light ratio for elliptical galaxies could be a factor of 10 larger relative to spirals in the B-band [73, 83]. If we shift the luminosity range of the subsample that corresponds to $M_{\rm min} < M < M_{\rm max}$ by $+5$ mag for ellipticals and $+1.5$ mag for S0s, respectively, then all the ellipticals will be removed (i.e., $M > M_{\rm max}$) and the number of S0s will increase by 30%, but the sum of E and S0 will only decrease from 25% to 20%, and the Sc contour move from 34% to 36%. Hence, uncertainties regarding the virial velocities of the ellipticals and S0s in the sample do not significantly affect our determination of the disk-dominated portion.

To test the dependence on mass cutoff $M_{\rm min}$, we vary this parameter from the fiducial cutoff at $5 \times 10^{10} M_\odot$ to a lower cutoff at $3.2 \times 10^{10} M_\odot$. The number density of halos increases by 50% to $0.034\,{\rm Mpc}^{-3}$. To compensate for the change in the number density of galaxies, we move the lower luminosity cutoff for selection from the *Tully* sample to $M_B < -15.5$. The observed fraction of disk-

dominated galaxies (Sc or later morphological type) remains unchanged at $\approx 33\%$, but the contours representing the bulge formation criterion move by about 10% toward lower critical virial velocities. This is because mergers with a fixed mass ratio μ tend to occur at smaller $V_{\rm vir,1}$ in smaller halos. The criterion, e.g., with $(\mu_{\rm crit}, V_{\rm vir,crit}) = (\frac{1}{4}, 57\ {\rm km\ s^{-1}})$ on the Sc contour in Figure 8.2 shifts only by a small amount, to $(\frac{1}{4}, 50\ {\rm km\ s^{-1}})$, as the mass cutoff is lowered to $3.2 \times 10^{10} M_\odot$. Any lower cutoffs than this are not appropriate, because at luminosities $M_B \lesssim -15$, disk galaxies give way to irregulars as the most common galaxy type [e.g., 22].

In Figure 8.2, we showed that the integrated fraction of disk-dominated galaxies in the mass range $M_{\rm min} < M < M_{\rm max}$ can be explained by a two-parameter model with $(\mu_{\rm crit}, V_{\rm vir,crit})$ along the Sc contour in that figure. However, we can also compare the disk-dominated fraction in our model with observations *as a function of halo mass*. The left panel of Figure 8.3 shows the disk-dominated fraction as a function of mass for the *Tully* subsample (Sc or later) and our model with $(\mu_{\rm crit}, V_{\rm vir,crit}) = (0.3, 55)$, $(0.4, 50)$, $(0.5, 45)$, and $(0.6, 35)$, respectively, which are points along the Sc contour in Figure 8.2. Our model predicts that disk-dominated fractions decrease too quickly with mass, compared to observation. The quick decline is understandable, because halos rarely accrete mass from $V_{\rm vir} = V_{\rm vir,crit}$ to $M \sim 10^{11.5} - 10^{12} M_\odot$ without major merger, i.e., $\mu > \mu_{\rm crit}$. However, these classical bulges formed when $V_{\rm vir} \sim V_{\rm vir,crit}$ may be too small to be observed for such large halos $M \sim 10^{11.5} - 10^{12} M_\odot$. To show this effect, we add a third criterion with a free parameter μ_2, which determines that the classical

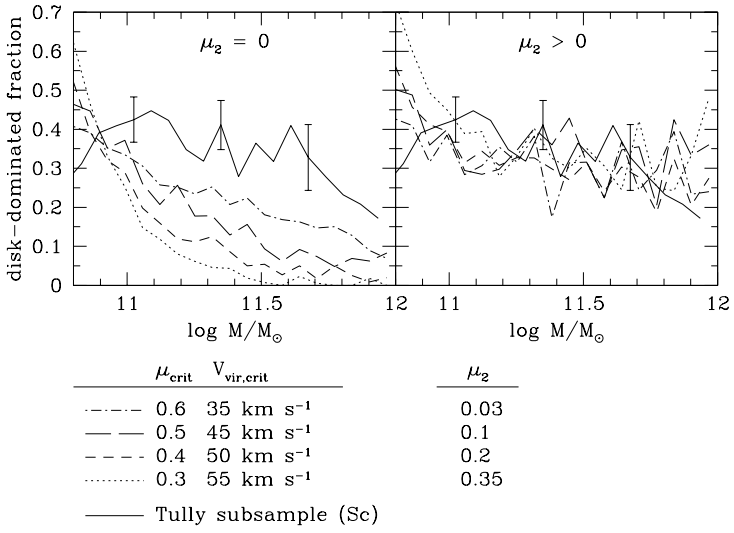

Figure 8.3: Disk-dominated fraction as a function of galaxy-hosting halo Mass for the two-parameter model ($\mu_{\rm crit}$, $V_{\rm vir,crit}$) (*left panel*) and the three-parameter model with additional parameter μ_2 (*right panel*), in which we assume that a merger remnant would not be observed as a classical bulge if its mass were smaller than μ_2 times present halo mass. Solid line is the observed fraction of Sc and later in the Tully subsample with Poisson error bars. Our model with two parameters does not agree with the observed mass dependence, but the agreement become reasonably good by introducing the third parameter μ_2

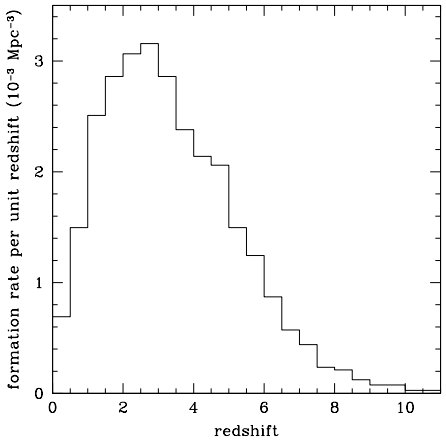

Figure 8.4: The redshift distribution of first mergers that create classical bulges. We assumed $\mu_{\rm crit} = 0.3$ and $V_{\rm vir,crit} = 55\,{\rm km\,s^{-1}}$ as the critical parameters for parameters of bulge formation, which is consistent with the abundance of disk-dominated galaxies in the local universe (see Fig. 8.2).

bulge is large enough to be observed only if,

$$(M_1 + M_2)(z_{\rm mer}) > \mu_2 M_0, \tag{8.4}$$

where $z_{\rm mer}$ is a redshift of a merger, and M_0 is the halo mass at present. With this additional condition, the disk-dominated fraction is consistent with the Tully sub-sample for, e.g., $(\mu_{\rm crit}, V_{\rm vir,crit}, \mu_2) = (0.3, 55, 0.35)$, $(0.4, 50, 0.2)$, $(0.5, 45, 0.1)$, or $(0.6, 35, 0.03)$. To make a better prediction, one must track the disk and bulge mass separately along the merger tree, and predict the bulge-to-total ratio, as often done in semianalytic galaxy formation models, which is beyond the scope of this paper.

In Figure 8.4, we plot the redshift distribution of the earliest bulge-forming

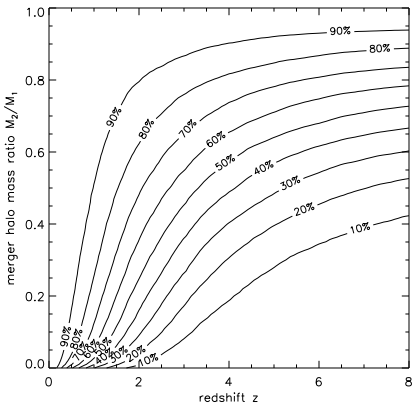

Figure 8.5: Fraction of halos that have not experienced a merger with mass ratio M_2/M_1 or larger since redshift z.

mergers of $z = 0$ halos for $\mu_{\rm crit} = 0.3$ and $V_{\rm vir,crit} = 55$ km s^{-1}.[8] The distribution is insensitive to the choices of $\mu_{\rm crit}$ and $V_{\rm vir,crit}$, as long as the two parameters remain on the same contour in Figure 8.2. This shows that bulge-forming mergers generally took place long after reionization was completed (i.e., $z_{\rm rei} \gtrsim 6$). Moreover, the typical collapse epoch for these merging halos was at $z < 6$ [157], so their star formation was also post-reionization. Hence the lower limit to $V_{\rm vir,crit}$ imposed by Jeans-mass filtering is applicable.

Minor mergers may not destroy galactic disks, but they can heat and thicken disks. Toth & Ostriker [175] placed an upper limit on the amount of merging that could have taken place during the lifetime of a galactic disk by quantifying the role

[8] If, as commonly assumed, bulge-forming mergers are responsible for quasar activity, it would be temping to point out the resemblance between the redshift distribution of first bulge-forming mergers and the observed evolution of the quasar luminosity [150]. However, the mass range of the halos in Figure 8.4 is significantly lower than that of the halos thought to host bright quasars.

of mergers in the heating and thickening of the Milky Way's disk. They found that in order for the Milky-Way disk to have remained thin, the Galaxy could not have accreted more than 5% of its present mass during the past 5 Gyr. Subsequent work refined the estimates of disk heating, resulting in less stringent constraints on the merger history [e.g., 19, 178]. An N-body simulation of mergers shows that a thin disk survives if $\mu < 0.02$ [98].

Kauffmann & White [95] used the Press-Schechter excursion set theory to generate merger histories of Milky-Way sized halos in a matter-dominated CDM universe (i.e., $\Lambda = 0$) and addressed the Toth-Ostriker constraint by calculating the fraction of halos that experienced a merger with mass ratio larger than μ after redshift z. Their results suggested that, while the Toth and Ostriker constraint might be difficult to satisfy in an Einstein-de Sitter universe, an open universe had no such difficulty. We have used our merger history calculation to recompute this statistic for the currently favored ΛCDM universe as shown in Figure 8.5. We find that, since $z = 1$, 70% of the halos throughout the mass range from $5 \times 10^{10} M_{\odot}$ to $10^{12} M_{\odot}$ had no merger with $\mu > 0.05$. This fraction is larger than that reported by Kauffmann & White [95] for their open universe case. This suggests that thin-disks survive the destructive effects of merger identified by [175].

Although the Toth & Ostriker constraint is probably satisfied in ΛCDM, the time period 5 Gyr is only a lower bound for the age of the disk. It is not certain weather thin disks survive during the whole history of galaxies. Stewart et al. [167] assume the age of thin disks to be $\sim$ 10 Gyr instead, consistent with estimates for the Milky Way. They conclude that whenever subhalos as large as $\sim 2 \times 10^{11}$

merge with Milky-Way sized galaxies anytime during the last 10 Gyr, their thin disks must survive, or else the 70% fraction of disk galaxies cannot be explained, but such survival seems unlikely. However, the typical present-day Milky Way-mass galaxies assembled most of their mass more recently then $\sim$ 10 Gyr ago, so it may not be necessary to require that typical thin-disks survived that long. Recently, Hopkins et al. [86] have claimed that mergers along nearly radial orbits (common in ΛCDM) heat the disk less than Toth-Ostriker's estimate because the infalling galaxy is rapidly tidally stripped. They said that even several 1:10 mergers could be consistent with the survival of Milky-Way thin disk.

8.3 Conclusions

In order to explain the observed space density and fraction of disk-dominated galaxies within the ΛCDM cosmology, we propose a bulge-forming criterion such that only those halo mergers with mass ratio greater than $\mu_{\rm crit} \sim 0.3$ and halo virial velocity (of the larger halo) above $V_{\rm vir,crit} \sim 55$ km s^{-1} formed classical bulges, while other mergers did not. This criterion has some degeneracy between $\mu_{\rm crit}$ and $V_{\rm vir,crit}$, but $V_{\rm vir,crit}$ cannot be larger than about 65 km s^{-1} without underproducing the galaxy fraction with bulges, or much smaller than $\sim$ 60 km s^{-1} since Jeans-mass filtering after reionization inhibits such small-mass halos from acquiring and retaining baryons or forming stars. The validity of this bulge formation criterion needs to be confirmed by further analytic calculation or hydrodynamical simulations of major and minor mergers in the halo mass range $V_{\rm vir,1} \lesssim 60$ km s^{-1}.

After we submitted this paper, Hopkins et al. [85] analyzed galaxy-merger

simulations for a wide range of merger parameters and presented an analytic model that predicts the post-merger disk fraction as a function of galaxy and merger properties. They found that the bulge dominated fraction among the merger remnants depends strongly on the gas fraction of the galaxies; with a larger gas fraction, bulge formation is less efficient. This is qualitatively consistent with our suggestion that bulge do not form for $V_{\rm vir} < V_{\rm vir,crit}$, because galaxies near the Jeans-mass filtering scale should be gas rich. Their simulations adopted a range of assumed gas fractions for the merging galaxies, but they did not attempt to determine the values of this gas fraction self-consistently for the ΛCDM universe. So we cannot directly compare the simulation results with our statistical analysis. Their results can, in principle, be incorporated into semi-analytic galaxy formation models, which estimate the gas fractions of merging galaxies, to improve the prediction of the disk-dominated fraction and other morphological properties in ΛCDM.

We find that bulge-forming criteria in our model that can explain the observed total disk-dominated galaxy fraction tend to predict that mass-dependent disk-dominated fraction decreases more rapidly with increasing halo mass than is observed. However the discrepancy disappears if the bulges formed by mergers that involved halos with masses much smaller than the final halo mass are difficult to detect. Future surveys of bulgeless/pseudobulged galaxy fraction as a function of mass should be a useful discriminant of models like ours and improve our knowledge of galaxy and bulge formation.

Acknowledgements

We would like to thank Shardha Jogee for detailed comments, and John Kormendy

for inspiring and illuminating discussions. We thank the anonymous referee for helpful comments. This work was supported in part by NSF grant AST-0708795 to M. M., and NASA ATP grants NNG04G177G, NNX07AH09G, SAO TM8-9009X, and NSF grant AST-0708176 to P. R. S.

Appendices

Appendix A

Scattering Cross Sections

In this appendix, we summarize various scattering cross sections appear in physics and in the nature.

A.1 The Definition

When a uniform flux of particles, J (number of particles passing a unit area per unit time), is scattered by a target particle, the differential cross section $d\sigma/d\Omega$ characterises the flux of scattered particles J_s to a solid angle $d\Omega$, by the proportionality relation

$$J_s d\Omega = J\frac{d\sigma}{d\Omega}d\Omega. \tag{A.1}$$

Total cross section σ is the angle integrated differential cross section

$$\sigma \equiv \int \frac{d\sigma}{d\Omega}d\Omega. \tag{A.2}$$

We consider two body scattering, but it is well known that a two body problem reduces to a one body problem by a change of variables. Let the mass, position and velocity of each particle be m_i, $\boldsymbol{x}_i$ and $\boldsymbol{v}_i$, respectively, for $i = 1, 2$. Assume that the interaction potential be translational invariant $V = V(\boldsymbol{r}_2 - \boldsymbol{r}_1)$. The Lagrangian

is

$$L = \frac{1}{2}m_1 v_1^2 + \frac{1}{2}m_2 v_2^2 - V(\boldsymbol{x}_1 - \boldsymbol{x}_2). \tag{A.3}$$

It is natural to introduce center-of-mass and relative coordinates

$$\boldsymbol{x}_{\rm cm} \equiv \frac{m_1 x_1 + m_2 x_2}{m_1 + m_2}, \quad \boldsymbol{v}_{\rm cm} \equiv \frac{d}{dt}\boldsymbol{x}_{\rm cm}, \tag{A.4}$$

$$\boldsymbol{r} \equiv \boldsymbol{x}_2 - \boldsymbol{x}_1, \quad \boldsymbol{v} \equiv \frac{d}{dt}\boldsymbol{r}. \tag{A.5}$$

The coordinate transformation gives a Lagrangian

$$L = \frac{1}{2}M v_{\rm cm}^2 + \frac{1}{2}m v^2 - V(\boldsymbol{r}), \tag{A.6}$$

where $M \equiv m_1 + m_2$ is the total mass, and $m_r \equiv (m_1^{-1} + m_2^{-1})^{-1}$ is the reduced mass. The system decouples to a trivial constant velocity motion in a straight line for the center of mass, and an one body system with $\boldsymbol{r}$ and $\boldsymbol{v}$.

Thus, in sections A.2 and A.3 we consider one body problems, with position $\boldsymbol{r}$ and velocity $\boldsymbol{v}$, scattered by some potentials $V(\boldsymbol{r})$. We only consider spherical symmetric potentials $V(\boldsymbol{r}) = V(r)$, for simplicity, in those sections.

A.2 Classical Mechanics

The cross section of classical-mechanical particles can be calculated by finding the relation between the scattering angle θ and the *impact parameter* b, which is the distance between the incident particle and the line parallel to the initial velocity and passes the origin $\boldsymbol{r} = 0$. [Fig. (A.1)]. Under a spherically symmetric potential, the angular momentum is conserved; therefore the orbit in confined on a plane passing the origin.

When the incoming particles with impact parameters between b and $b + db$ are scattered to angles between θ and $\theta + d\theta$ by a spherically symmetric potential, the definition (Eq. A.1) gives

$$\frac{d\sigma}{d\Omega} = \frac{b}{\sin\theta}\left|\frac{db}{d\theta}\right|. \tag{A.7}$$

We show three cross sections below.

A.2.1 Hard Sphere

Hard sphere is defined to have an infinite potential inside some radius R and zero outside. Geometrically, one can find a relation between the impact parameter b and the scattering angle θ (Fig. A.1)

$$b = R\cos\frac{\theta}{2}. \tag{A.8}$$

We thus have the isotropic and velocity-independent differential cross section, from (A.7)

$$\left(\frac{d\sigma}{d\Omega}\right)_{\text{hardsphere}} = \frac{1}{4}R^2 \tag{A.9}$$

The total cross section is the geometrical cross section; $\sigma = \pi R^2$. Therefore we call a velocity independent and isotropic scattering a *hard sphere cross section* (e.g., [113]).

Remark: Although one can in principal calculate the cross section of hard sphere potential with quantum mechanics, the result does not have a simple analytical form.

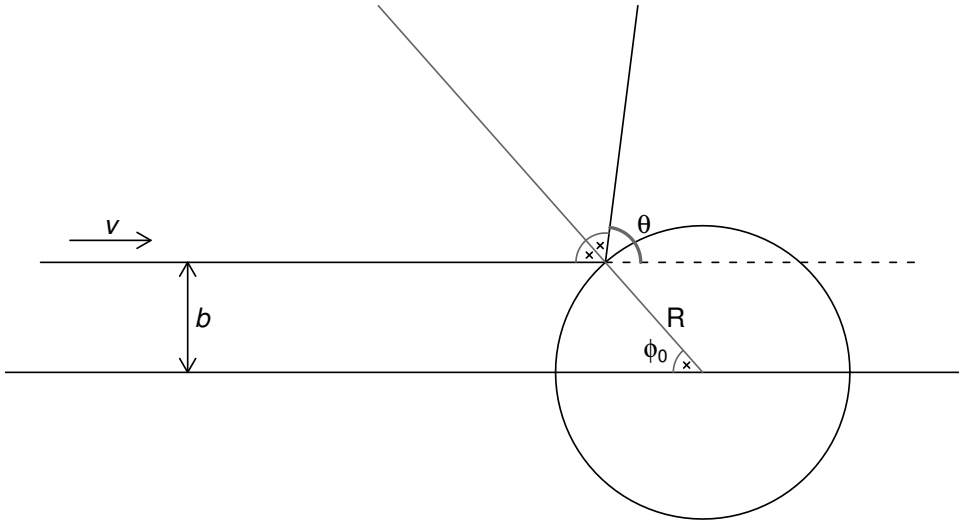

Figure A.1: The diagram of scattering by a hard sphere with radius R. The scattering angle θ is related to the angle ϕ_0; $\theta = \pi - 2\phi_0$. The impact parameter b is also related to the angle ϕ_0; $R\sin\phi_0$. Those two equations gives Equation (A.8). Because the force is normal to the surface of the sphere, the velocity component parallel to the surface remains constant; the velocity component normal to the surface only change is sign due to energy conservation.

Historical remarks: James Clerk Maxwell calculated the scattering properties of two hard spheres in his paper in 1860, in which he first introduced what is currently known as the Maxwellian distribution [131, 133]. He showed that when every position is equally probable, the probability of the direction of rebound is isotropic; this is exactly what we now mean by the hard sphere cross section.

A.2.2 The Maxwell Molecule or the Inverse Power Law Model

In 1867 paper, James Clerk Maxwell calculated the scattering problem of inverse power low $V(r) = \alpha/r^{(n-1)}$, and show the velocity dependence of the differential cross section is $d\sigma/d\Omega \propto v^{-4/(n-1)}$), as shown below [132, 133].

The energy conservation

$$\frac{1}{2}mv^2 = \frac{1}{2}m\dot{r}^2 + \frac{1}{2}mr^2\dot{\phi}^2 + V(r), \tag{A.10}$$

together with angular momentum conservation

$$mbv = mr^2\dot{\phi}, \tag{A.11}$$

gives an integral form of the relation between the scattering angle θ and the impact parameter b:

$$\theta = \pi - 2b\int_{r_{\min}}^{\infty} \frac{bdr/r^2}{\sqrt{1 - \frac{b^2}{r^2} - \frac{2}{mv^2}V(r)}}, \tag{A.12}$$

where $r_{\min}$ is the radius of closest approach (perihelion); it is the largest positive solution when $\dot{r} = 0$ in Equations (A.10, A.11). With change of variables,

$$u \equiv b/r, \quad u_{\max} \equiv b/r_{\min}, \tag{A.13}$$

$$\eta \equiv b\left(mv^2/\alpha\right)^{\frac{1}{n-1}}, \tag{A.14}$$

equation become

$$\theta = \pi - 2\int_0^{u_{\max}} du/\sqrt{1 - u^2 - 2(u/\eta)^{n-1}}. \tag{A.15}$$

Because $u_{\max}$ depends only on η for a given constant n ($u_{\max}$ is the smallest positive solution of $1 - u^2 - 2(u/\eta)^n = 0$), $\theta = \theta(\eta)$ is a pure mathematical function

of η, independent of the physical parameters b or v. From equations (A.7) and (A.14), the differential cross section is

$$\frac{d\sigma}{d\Omega} = (mv^2/\alpha)^{-\frac{2}{n-1}} \frac{\eta}{\sin\theta} \frac{d\eta}{d\theta}. \tag{A.16}$$

The first factor gives the velocity dependence $v^{-4/(n-1)}$; the latter factors are functions of θ only.

The cross section is inversely proportional to the velocity if $n = 5$. Maxwell thought $n = 5$ is realistic enough model for molecules, and even calculated the differential cross section numerically. For this reason, any cross section inversely proportional to velocity is called the *Maxwell model*, or the *Maxwell molecules*; because the angular dependence of the inverse power law scattering is complicated, cross sections with other angular function are often called the Maxwell model as well.

Today, the Maxwell model is widely used in theoretical studies of Boltzmann systems, although, it is not realistic enough for molecular gas dynamics; an exact analytical solution of spatially-homogeneous Boltzmann equation for the the Maxwell model (for arbitrary function of angular dependence), is a milestone of the theoretical understanding of the Boltzmann equation [25, 107, 108, 109].

A.2.3 The Rutherford Scattering

In 1911 Rutherford explained his and his students' data of α and β particles scattered by Nucleus with his formula of differential cross section associated with the Coulomb potential, $V(r) = \alpha/r$, [152].

Figure A.2: The diagram of Rutherford scattering with impact parameter b and scattering angle θ. When the asymptotic speed is v, the momentum transfer due to the scattering is $q \equiv |\boldsymbol{p}_f - \boldsymbol{p}_i| = 2mv\sin\theta/2$. One the other hand, we can calculated the momentum transfer by integrating the y component of the force; $q = 2\int_{-\infty}^{\infty} F_y dt = -2\int \frac{\alpha}{r^2} dt = -\frac{2\alpha}{vb}\int_{\theta/2}^{\pi/2} \sin\phi d\phi$. These two equations give Equation A.17.[2] The motion has a reflection symmetry about the y-axis because of the spherical and time-reversal symmetry; consider a motion starting at a point on y-axis with a velocity perpendicular to the axis and its time reversal.

By integrating the hyperbolic Kepler orbit (e.g., [93, 113]), or the momentum transfer (Fig. A.2), one can obtain

$$b = \frac{\alpha}{mv^2}\frac{1}{\tan\frac{\theta}{2}}. \tag{A.17}$$

The differential cross section is the *Rutherford scattering cross section*

$$\left(\frac{d\sigma}{d\Omega}\right)_{\text{Rutherford}} = \frac{\alpha^2}{4m^2v^4}\frac{1}{\sin^4\frac{\theta}{2}} \tag{A.18}$$

A.3 Quantum Mechanics

We show some cross sections appear in (non-relativistic) quantum mechanics, represented by the Schrödinger equation

$$\left(-\frac{\hbar^2}{2m}\nabla^2 + V(r)\right)\psi = E\psi. \tag{A.19}$$

A.3.1 Yukawa Cross Section

We derive the scattering cross section of Yukawa potential

$$V(r) = \alpha e^{-\beta r}/r \tag{A.20}$$

using the first order Born approximation (Eq. A.29).

Let the potential be a perturbation of order ϵ — the order parameter. Expand the wave function and the energy with respect to ϵ

$$\psi = \psi_0 + \epsilon\psi_1 + \mathcal{O}(\epsilon^2) \tag{A.21}$$

$$E = E_0 + \epsilon E_1 + \mathcal{O}(\epsilon^2) \tag{A.22}$$

The zeroth order of ϵ gives

$$-\frac{\hbar^2}{2m}\nabla^2\psi = E_0\psi. \tag{A.23}$$

Because this is the solution without the potential, the solution for the scattering problem should be the incident plan wave

$$\psi_0(\boldsymbol{r}) = e^{-i\boldsymbol{k}\cdot\boldsymbol{r}}, \quad E_0 = \frac{\hbar^2 k^2}{2m}. \tag{A.24}$$

The first order is the Helmholtz equation

$$(\nabla^2 + k^2)\psi_1(\boldsymbol{r}) = \frac{\hbar^2}{2m}V(r)\psi_0, \tag{A.25}$$

where we set $E_1 = 0$; because $E_1 > 0$ would simply give additional homogeneous solution unperturbed by the potential; we assume, as the setup, that the ψ_0 is the only such mode. The Green's function G of the Helmholtz operator $(\nabla^2 + k^2)$, i.e.,

$$(\nabla^2 + k^2)G(\boldsymbol{r}) = \delta^3(\boldsymbol{r}), \tag{A.26}$$

is

$$G(\boldsymbol{r}) = \frac{e^{\pm ikr}}{r}, \tag{A.27}$$

which can be derived, e.g., by Fourier transform followed by a complex contour integral. In the scattering problem, the scattered spherical wave ψ_1 is outgoing, e^{-ikr}/r; hence the scattered wave has the integral form, with an asymptotic analytical expression

$$\psi_1(\boldsymbol{r}) = -\frac{\hbar^2}{2m}\int d^3r' G(\boldsymbol{r}-\boldsymbol{r'})V(r') \rightarrow -\frac{2\alpha m}{\hbar^2}\frac{1}{\beta^2+k^2}\frac{e^{-ikr}}{r}, \tag{A.28}$$

where the asymptotic form assumes large $\boldsymbol{r}$ (i.e., $1/|\boldsymbol{r}+\boldsymbol{r'}| \rightarrow 1/r$). By comparing with the definition of $f(\theta)$, one obtains the *Yukawa scattering cross section*

$$\frac{d\sigma}{d\Omega} = \left(\frac{2m\alpha}{\hbar^2}\right)^2 \frac{1}{(\beta^2+k^2)^2}. \tag{A.29}$$

Remark: Noting that the momentum is $mv = \hbar k$, Yukawa cross section reduces to the Rutherford cross section for $\beta \rightarrow 0$, and to the hard sphere cross section for $\alpha \gg k$, respectively.

Bibliography

[1] Aarseth, S. J., Henon, M., & Wielen, R. 1974, A&A, 37, 183

[2] Abadi, M. G., Navarro, J. F., Steinmetz, M., & Eke, V. R. 2003, ApJ, 591, 499

[3] Ackerman, L., Buckley, M. R., Carroll, S. M., & Kamionkowski, M. 2009, Phys. Rev. D, 79, 023519

[4] Ahn, K., & Shapiro, P. R. 2005, MNRAS, 363, 1092, (A&S)

[5] —. 2007, MNRAS, 375, 881

[6] Alam, S. M. K., Bullock, J. S., & Weinberg, D. H. 2002, ApJ, 572, 34

[7] Allen, P. D., Driver, S. P., Graham, A. W., Cameron, E., Liske, J., & de Propris, R. 2006, MNRAS, 371, 2

[8] Alvarez, M. A., Ahn, K., & Shapiro, P. R. 2003, in Revista Mexicana de Astronomia y Astrofisica Conference Series, Vol. 18, Revista Mexicana de Astronomia y Astrofisica Conference Series, ed. M. Reyes-Ruiz & E. Vázquez-Semadeni, 4–7

[9] Arabadjis, J. S., Bautz, M. W., & Garmire, G. P. 2002, ApJ, 572, 66

[10] Ascasibar, Y., Yepes, G., Gottlöber, S., & Müller, V. 2004, MNRAS, 352, 1109

[11] Athanassoula, E. 2005, MNRAS, 358, 1477

[12] Babovsky, H., & Illner, R. 1989, SIAM J. Numer. Anal., 26, 45

[13] Balberg, S., Shapiro, S. L., & Inagaki, S. 2002, ApJ, 568, 475, (BSI)

[14] Barazza, F. D., Jogee, S., & Marinova, I. 2008, ApJ, 675, 1194

[15] Bardeen, J. M., Bond, J. R., Kaiser, N., & Szalay, A. S. 1986, ApJ, 304, 15

[16] Baugh, C. M., Cole, S., & Frenk, C. S. 1996, MNRAS, 283, 1361

[17] Baumgardt, H., Heggie, D. C., Hut, P., & Makino, J. 2003, MNRAS, 341, 247

[18] Bedregal, A. G., Aragón-Salamanca, A., & Merrifield, M. R. 2006, MNRAS, 373, 1125

[19] Benson, A. J., Lacey, C. G., Frenk, C. S., Baugh, C. M., & Cole, S. 2004, MNRAS, 351, 1215

[20] Bertschinger, E. 2001, ApJS, 137, 1

[21] Bettwieser, E. 1983, MNRAS, 203, 811

[22] Binggeli, B., Sandage, A., & Tammann, G. A. 1988, ARA&A, 26, 509

[23] Binney, J., & Tremaine, S. 1987, Galactic dynamics (Princeton, NJ, Princeton University Press)

[24] Bird, G. A. 1994, Molecular Gas Dynamics and the Direct Simulation of Gas Flows (Clarendon, Oxford, 1994)

[25] Bobylev, A. V. 1975, Doklady Akad. Nauk SSSR., 225, 1296

[26] Böker, T., Laine, S., van der Marel, R. P., Sarzi, M., Rix, H.-W., Ho, L. C., & Shields, J. C. 2002, AJ, 123, 1389

[27] Böker, T., Stanek, R., & van der Marel, R. P. 2003, AJ, 125, 1073

[28] Bondi, H. 1947, MNRAS, 107, 410

[29] Bournaud, F., Jog, C. J., & Combes, F. 2005, A&A, 437, 69

[30] —. 2007, A&A, 476, 1179

[31] Bowers, R. L., & Wilson, J. R. 1991, Numerical modeling in applied physics and astrophysics (abc)

[32] Boylan-Kolchin, M., Ma, C.-P., & Quataert, E. 2008, MNRAS, 383, 93

[33] Bryan, G. L., & Norman, M. L. 1998, ApJ, 495, 80

[34] Bullock, J. S., Kolatt, T. S., Sigad, Y., Somerville, R. S., Kravtsov, A. V., Klypin, A. A., Primack, J. R., & Dekel, A. 2001, MNRAS, 321, 559

[35] Bureau, M., Freeman, K. C., Pfitzner, D. W., & Meurer, G. R. 1999, AJ, 118, 2158

[36] Burkert, A. 1995, ApJ, 447, L25+

[37] —. 2000, ApJ, 534, L143

[38] Casertano, S., & Hut, P. 1985, ApJ, 298, 80

[39] Chapman, S., & Cowling, T. G. 1970, The mathematical theory of non-uniform gases (Cambridge: University Press, 1970, 3rd ed.)

[40] Clowe, D., Bradač, M., Gonzalez, A. H., Markevitch, M., Randall, S. W., Jones, C., & Zaritsky, D. 2006, ApJ, 648, L109

[41] Cohn, H. 1980, ApJ, 242, 765

[42] Colín, P., Avila-Reese, V., Valenzuela, O., & Firmani, C. 2002, ApJ, 581, 777

[43] Combes, F. 1998, in Starbursts: Triggers, Nature, and Evolution, Les Houches School, ed. B. Guiderdoni & A. Kembhavi, 175–+

[44] Cox, T. J., Jonsson, P., Somerville, R. S., Primack, J. R., & Dekel, A. 2008, MNRAS, 384, 386

[45] Crocce, M., Pueblas, S., & Scoccimarro, R. 2006, MNRAS, 373, 369

[46] Davé, R., Spergel, D. N., Steinhardt, P. J., & Wandelt, B. D. 2001, ApJ, 547, 574

[47] Davis, M., Efstathiou, G., Frenk, C. S., & White, S. D. M. 1985, ApJ, 292, 371

[48] de Blok, W. J. G., Bosma, A., & McGaugh, S. 2003, MNRAS, 340, 657

[49] de Blok, W. J. G., Walter, F., Brinks, E., Trachternach, C., Oh, S.-H., & Kennicutt, R. C. 2008, AJ, 136, 2648

[50] Diemand, J., Zemp, M., Moore, B., Stadel, J., & Carollo, C. M. 2005, MNRAS, 364, 665

[51] D'Onghia, E., & Burkert, A. 2003, ApJ, 586, 12

[52] —. 2004, ApJ, 612, L13

[53] D'Onghia, E., Burkert, A., Murante, G., & Khochfar, S. 2006, MNRAS, 372, 1525

[54] D'Onghia, E., Firmani, C., & Chincarini, G. 2003, MNRAS, 338, 156

[55] Efstathiou, G. 1992, MNRAS, 256, 43P

[56] Eliche-Moral, M. C., Balcells, M., Aguerri, J. A. L., & González-García, A. C. 2006, A&A, 457, 91

[57] Endoh, H., Fukushige, T., & Makino, J. 1997, PASJ, 49, 345

[58] Farrar, G. R., & Rosen, R. A. 2007, Physical Review Letters, 98, 171302

[59] Feng, J. L., Kaplinghat, M., Tu, H., & Yu, H.-B. 2009, Journal of Cosmology and Astro-Particle Physics, 7, 4

[60] Firmani, C., et al. 2000, ArXiv Astrophysics e-prints

[61] Fryxell, B., et al. 2000, ApJS, 131, 273

[62] Gallis, M. A., Torczynski, J. R., & Rader, D. J. 2004, Phys. Rev. E, 69, 042201

[63] Gao, L., Navarro, J. F., Cole, S., Frenk, C. S., White, S. D. M., Springel, V., Jenkins, A., & Neto, A. F. 2008, MNRAS, 387, 536

[64] Gentile, G., Salucci, P., Klein, U., Vergani, D., & Kalberla, P. 2004, MNRAS, 351, 903

[65] Gentile, G., Tonini, C., & Salucci, P. 2007, ArXiv Astrophysics e-prints

[66] Gnedin, O. Y., & Ostriker, J. P. 2001, ApJ, 561, 61

[67] Goldreich, P., & Tremaine, S. 1980, ApJ, 241, 425

[68] Goodman, J. 1987, ApJ, 313, 576

[69] Goodman, J., & Rafikov, R. R. 2001, ApJ, 552, 793

[70] Gough, B. 2009, GNU Scientific Library Reference Manual - Third Edition (Network Theory Ltd.)

[71] Greengard, C., & Reyna, L. 1991, Phys. Fluids A, 4, 4

[72] Gunn, J. E., & Gott, J. R. I. 1972, ApJ, 176, 1

[73] Guzik, J., & Seljak, U. 2002, MNRAS, 335, 311

[74] Hachisu, I., & Sugimoto, D. 1978, Progress of Theoretical Physics, 60, 123

[75] Hayashi, E., & Navarro, J. F. 2006, MNRAS, 373, 1117

[76] Hayashi, E., & White, S. D. M. 2006, MNRAS, 370, L38

[77] Hayashi, E., et al. 2004, MNRAS, 355, 794

[78] Heggie, D. C. 1984, MNRAS, 206, 179

[79] Heggie, D. C., & Ramamani, N. 1989, MNRAS, 237, 757

[80] Heggie, D. C., & Stevenson, D. 1988, MNRAS, 230, 223

[81] Hennawi, J. F., & Ostriker, J. P. 2002, ApJ, 572, 41

[82] Hernquist, L. 1990, ApJ, 356, 359

[83] Hoekstra, H., Hsieh, B. C., Yee, H. K. C., Lin, H., & Gladders, M. D. 2005, ApJ, 635, 73

[84] Hoffman, Y., Romano-Díaz, E., Shlosman, I., & Heller, C. 2007, ApJ, 671, 1108

[85] Hopkins, P. F., Cox, T. J., Younger, J. D., & Hernquist, L. 2009, ApJ, 691, 1168

[86] Hopkins, P. F., Hernquist, L., Cox, T. J., Younger, J. D., & Besla, G. 2008, ApJ, 688, 757

[87] Hut, P., & Makino, J. 1987, The Art of Computational Science Vol. 11 (http://www.artcompsci.org/kali/vol/plummer/title.html)

[88] Iliev, I. T., Mellema, G., Shapiro, P. R., & Pen, U.-L. 2007, MNRAS, 376, 534

[89] Iliev, I. T., & Shapiro, P. R. 2001, ApJ, 546, L5

[90] —. 2001, MNRAS, 325, 468

[91] Jiang, C. Y., Jing, Y. P., Faltenbacher, A., Lin, W. P., & Li, C. 2008, ApJ, 675, 1095

[92] Jogee, S., Scoville, N., & Kenney, J. D. P. 2005, ApJ, 630, 837

[93] Jose, J. V., & Saletan, E. J. 1998, Classical dynamics : a contemporary approach (New York : Cambridge University Press, 1998.)

[94] Kannappan, S. J., Fabricant, D. G., & Franx, M. 2002, AJ, 123, 2358

[95] Kauffmann, G., & White, S. D. M. 1993, MNRAS, 261, 921

[96] Kauffmann, G., White, S. D. M., & Guiderdoni, B. 1993, MNRAS, 264, 201

[97] Kautsch, S. J., Grebel, E. K., Barazza, F. D., & Gallagher, III, J. S. 2006, A&A, 445, 765

[98] Kazantzidis, S., Bullock, J. S., Zentner, A. R., Kravtsov, A. V., & Moustakas, L. A. 2008, ApJ, 688, 254

[99] Kazantzidis, S., Magorrian, J., & Moore, B. 2004, ApJ, 601, 37

[100] Khalisi, E., Amaro-Seoane, P., & Spurzem, R. 2007, MNRAS, 374, 703

[101] Kitayama, T., & Ikeuchi, S. 2000, ApJ, 529, 615

[102] Kochanek, C. S., & White, M. 2000, ApJ, 543, 514

[103] Koda, J., Milosavljević, M., & Shapiro, P. R. 2009, ApJ, 696, 254

[104] Koda, J., Milosavljevic, M., Shapiro, P. R., Nagai, D., & Nakar, E. 2008, ArXiv e-prints

[105] Kormendy, J. 2008, in IAU Symposium, Vol. 245, IAU Symposium, ed. M. Bureau, E. Athanassoula, & B. Barbuy, 107–112

[106] Kormendy, J., & Kennicutt, Jr., R. C. 2004, ARA&A, 42, 603

[107] Krook, M., & Wu, T. T. 1976, Phys. Rev. Lett., 36, 1107

[108] —. 1977, Physics of Fluids, 20, 1589

[109] Krupp, R. S. 1967, M.S. thesis, MIT

[110] Kuzio de Naray, R., McGaugh, S. S., & de Blok, W. J. G. 2008, ApJ, 676, 920

[111] Kuzio de Naray, R., McGaugh, S. S., de Blok, W. J. G., & Bosma, A. 2006, ApJS, 165, 461

[112] Kuzio de Naray, R., McGaugh, S. S., & Mihos, J. C. 2009, ApJ, 692, 1321

[113] Landau, L. D., & Lifshitz, E. M. 1976, Mechanics (Oxford: Pergamon Press, 1976, 3rd ed.)

[114] Larson, R. B. 1970, MNRAS, 147, 323

[115] Levermore, C. D. 1996, Journal of Statistical Physics, 83, 1021

[116] Lewis, A., Challinor, A., & Lasenby, A. 2000, Astrophys. J., 538, 473

[117] Lewis, A. D., Buote, D. A., & Stocke, J. T. 2003, ApJ, 586, 135

[118] Lifshitz, E. M., & Pitaevskii, L. P. 1981, Physical Kinetics (Oxford ; Butterworth-Heinemann)

[119] Louis, P. D. 1990, MNRAS, 244, 478

[120] Lynden-Bell, D., & Eggleton, P. P. 1980, MNRAS, 191, 483, (LBE)

[121] Lynden-Bell, D., & Wood, R. 1968, MNRAS, 138, 495

[122] Macciò, A. V., Dutton, A. A., & van den Bosch, F. C. 2008, MNRAS, 391, 1940

[123] Mahdavi, A., Hoekstra, H., Babul, A., Balam, D., & Capak, P. 2007, ArXiv e-prints, 706

[124] Makino, J. 1996, ApJ, 471, 796

[125] Maller, A. H., Katz, N., Kereš, D., Davé, R., & Weinberg, D. H. 2006, ApJ, 647, 763

[126] Markevitch, M. 2006, in ESA Special Publication, Vol. 604, The X-ray Universe 2005, ed. A. Wilson, 723–+

[127] Markevitch, M., Gonzalez, A. H., Clowe, D., Vikhlinin, A., Forman, W., Jones, C., Murray, S., & Tucker, W. 2004, ApJ, 606, 819

[128] Markevitch, M., & Vikhlinin, A. 2007, Phys. Rep., 443, 1

[129] Mastropietro, C., & Burkert, A. 2007, ArXiv e-prints, 711

[130] —. 2008, MNRAS, 389, 967

[131] Maxwell, J. C. 1860, Philosophical Magazine, 19, 20, 19,21

[132] —. 1867, Philosophical Transactions of the Royal Society of London, 157, 49

[133] —. 1890, Scientific Papers, Vol. 1 (Cambridge University Press. (Reprinted by Dover Publications, New York))

[134] Mihos, J. C., & Hernquist, L. 1994, ApJ, 425, L13

[135] —. 1996, ApJ, 464, 641

[136] Milosavljević, M. 2004, ApJ, 605, L13

[137] Milosavljević, M., Koda, J., Nagai, D., Nakar, E., & Shapiro, P. R. 2007, ApJ, 661, L131

[138] Monaco, P., Theuns, T., & Taffoni, G. 2002, MNRAS, 331, 587

[139] Naab, T., & Burkert, A. 2003, ApJ, 597, 893

[140] Nanbu, K. 1980, Journal of the Physical Society of Japan, 49, 2042

[141] —. 1984, Physics of Fluids, 27, 2632

[142] Navarro, J. F., Frenk, C. S., & White, S. D. M. 1997, ApJ, 490, 493

[143] Navarro, J. F., & Steinmetz, M. 1997, ApJ, 478, 13

[144] Navarro, J. F., et al. 2008, ArXiv e-prints

[145] Oh, S.-H., de Blok, W. J. G., Walter, F., Brinks, E., & Kennicutt, R. C. 2008, AJ, 136, 2761

[146] Petrosian, V., Madejski, G., & Luli, K. 2006, ApJ, 652, 948

[147] Piontek, R. A., & Ostriker, E. C. 2004, ApJ, 601, 905

[148] Randall, S. W., Markevitch, M., Clowe, D., Gonzalez, A. H., & Bradac, M. 2007, ArXiv e-prints, 704

[149] Reed, D., Governato, F., Verde, L., Gardner, J., Quinn, T., Stadel, J., Merritt, D., & Lake, G. 2005, MNRAS, 357, 82

[150] Richards, G. T., et al. 2006, AJ, 131, 2766

[151] Rozyczka, M., & Spruit, H. C. 1993, ApJ, 417, 677

[152] Rutherford, E. 1911, Philosophical Magazine, 21, 669

[153] Savonije, G. J., Papaloizou, J. C. B., & Lin, D. N. C. 1994, MNRAS, 268, 13

[154] Sellwood, J. A. 2003, ApJ, 587, 638

[155] —. 2006, ApJ, 637, 567

[156] Shapiro, P. R., Giroux, M. L., & Babul, A. 1994, ApJ, 427, 25

[157] Shapiro, P. R., & Iliev, I. T. 2002, ApJ, 565, L1

[158] Shapiro, P. R., Iliev, I. T., & Raga, A. C. 1999, MNRAS, 307, 203

[159] Simon, J. D., Bolatto, A. D., Leroy, A., Blitz, L., & Gates, E. L. 2005, ApJ, 621, 757

[160] Spano, M., Marcelin, M., Amram, P., Carignan, C., Epinat, B., & Hernandez, O. 2008, MNRAS, 383, 297

[161] Spergel, D. N., & Steinhardt, P. J. 2000, Physical Review Letters, 84, 3760

[162] Spergel, D. N., et al. 2007, ApJS, 170, 377

[163] Springel, V., & Farrar, G. R. 2007, MNRAS, 380, 911

[164] Springel, V., Yoshida, N., & White, S. D. M. 2001, New Astronomy, 6, 79

[165] Spurzem, R., & Aarseth, S. J. 1996, MNRAS, 282, 19

[166] Stadel, J., Potter, D., Moore, B., Diemand, J., Madau, P., Zemp, M., Kuhlen, M., & Quilis, V. 2009, MNRAS, 398, L21

[167] Stewart, K. R., Bullock, J. S., Wechsler, R. H., Maller, A. H., & Zentner, A. R. 2008, ApJ, 683, 597

[168] Szell, A., Merritt, D., & Kevrekidis, I. G. 2005, Physical Review Letters, 95, 081102

[169] Takahashi, K. 1995, PASJ, 47, 561

[170] Tasitsiomi, A., Kravtsov, A. V., Gottlöber, S., & Klypin, A. A. 2004, ApJ, 607, 125

[171] Thoul, A. A., & Weinberg, D. H. 1995, ApJ, 442, 480

[172] —. 1996, ApJ, 465, 608

[173] Tolman, R. C. 1934, Proceedings of the National Academy of Science, 20, 169

[174] Tormen, G., Bouchet, F. R., & White, S. D. M. 1997, MNRAS, 286, 865

[175] Toth, G., & Ostriker, J. P. 1992, ApJ, 389, 5

[176] Trachternach, C., de Blok, W. J. G., Walter, F., Brinks, E., & Kennicutt, R. C. 2008, AJ, 136, 2720

[177] Valenzuela, O., Rhee, G., Klypin, A., Governato, F., Stinson, G., Quinn, T., & Wadsley, J. 2007, ApJ, 657, 773

[178] Velazquez, H., & White, S. D. M. 1999, MNRAS, 304, 254

[179] Vesely, F. J. 2001, Computational Physics: An Introduction (New York, Plenum Press)

[180] Walcher, C. J., et al. 2005, ApJ, 618, 237

[181] Wechsler, R. H., Bullock, J. S., Primack, J. R., Kravtsov, A. V., & Dekel, A. 2002, ApJ, 568, 52

[182] Weinberg, M. D., & Katz, N. 2002, ApJ, 580, 627

[183] Yoshida, N., Springel, V., White, S. D. M., & Tormen, G. 2000, ApJ, 544, L87

[184] Zackrisson, E., Bergvall, N., Marquart, T., & Östlin, G. 2006, A&A, 452, 857

Vita

Jun Koda was born in Minneapolis, Minnesota in 1979 between Japanese parents. He grew up in Saitama, Japan and graduated from Urawa High School in 1998. He received the Bachelor of Science degree in Physics from Kyoto University in March 2002. He was accepted and started graduate studies at the University of Texas at Austin in the fall of 2002.

Permanent address: 1320-27 Kamihideya, Okegawa-shi, Saitama
363-0026, Japan

This dissertation was typeset with LaTeX[†] by the author.

[†]LaTeX is a document preparation system developed by Leslie Lamport as a special version of Donald Knuth's TeX Program.